Universiteit
Leiden
The Netherlands

Optical coherence tomography for coronary artery disease : analysis and applications

Liu, S.

Citation
Liu, S. (2018, September 4). *Optical coherence tomography for coronary artery disease : analysis and applications*. Retrieved from https://hdl.handle.net/1887/64938

Version:	Not Applicable (or Unknown)
License:	Licence agreement concerning inclusion of doctoral thesis in the Institutional Repository of the University of Leiden
Downloaded from:	https://hdl.handle.net/1887/64938

Note: To cite this publication please use the final published version (if applicable).

Cover Page

Universiteit Leiden

The handle http://hdl.handle.net/1887/64938 holds various files of this Leiden University dissertation.

Author: Liu, S.
Title: Optical coherence tomography for coronary artery disease : analysis and applications
Issue Date: 2018-09-04

Optical Coherence Tomography for Coronary Artery Disease: Analysis and Applications

Optical coherence Tomography for Coronary Artery Disease:
Analysis and Applications
Shengnan Liu

ISBN: 978-94-93019-16-4
Printed by: Proefschriftmaken || www.proefschriftmaken.nl

This book was typeset by the author using LaTeX. The main body of the text was set using a 10-points New Century Schoolbook font. References were organized to follow standard American Medical Association (AMA) style.

About the cover: An OCT image is shown in a wall plate in Deft Blue color scheme. It was mached using exact histogram specification technque in Matlab2017 (The MathWork, Inc). The Dutch elements would remind me of all the good moments during my PhD period.

© 2018, Shengnan Liu, Leiden, The Netherlands. All rights reserved. No part of this publication may be reproduced or transmitted in any form or by any means, electronic or mechanical, including photocopy, recording, or any information storage and retrieval system, without permission in writing from the copyright owner.

Optical coherence Tomography for Coronary Artery Disease: Analysis and Applications

Proefschrift

ter verkrijging van de graad van doctor aan de
Universiteit Leiden
op gezag van
rector magnificus

prof. mr. C.J.J.M. Stolker

volgens besluit van het College voor Promoties.

te verdedigen op
donderdag 4 september 2018 om 16:15 uur

door

Shengnan Liu

geboren te Dunhua, China

Promotor:	**Prof.dr.ir. B.P.F. Lelieveldt**
Copromotor:	**Dr.ir. J. Dijkstra**
Leden promotiecommissie:	**Prof.dr. A.G.J.M. van Leeuwen** *University of Amsterdam*
	Dr. J.J. Wentzel *Erasmus Medical Center*
	Prof.dr. P.H.A. Quax

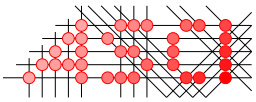

The research in this thesis was conducted at Division of Medical Image Procession (LKEB), Department of Radiology of the Leiden University Medical Center, Leiden, The Netherlands. This work was carried out in the ASCI graduate school. ASCI dissertation series number 393.

Financial support by the Dutch Heart Foundation for the publication of this thesis is gratefully acknowledged.

Financial support for the publication of this thesis was kindly provided by:
the Dutch Heart Foundation
ASCI research school
Library of the University of Leiden

To remember my beloved Grandma G. Yao and Grandpa D. Hao...

— LEIDEN, NOVEMBER 2017

Contents

Colophon **ii**

Preface **v**

1 Introduction **1**
1.1 Coronary artery disease 1
1.2 Intravascular optical coherence tomography 3
1.3 Intravascular optical coherence tomography in clinical studies . . . 4
1.4 Tissue Characterization 7
1.4.1 Optical properties 8
1.5 Outline of the thesis 9

2 Analysis and Compensation for the Effect of the Catheter Position on Image Intensities in Intravascular Optical Coherence Tomography **11**
2.1 Introduction 12
2.2 Materials and Methodology 14
2.2.1 Distance and Incident Angle Extended Light Transmission Model 14
2.2.2 Parameter estimation of the linear model with Hierarchical linear regression 16
2.2.3 Compensation 17
2.3 Results 18
2.3.1 Hierarchical linear regression 18
2.3.2 Compensation 19
2.4 Application of the compensated images 20
2.4.1 Pathological images with foam cells 20
2.4.2 BVS strut detection 20
2.5 Discussions 21
2.5.1 Hierarchical linear regression 22
2.5.2 Compensation 23
2.5.3 Limitations 24
2.5.4 Future work 25
2.6 Conclusions 25

3 Tissue characterization with depth-resolved attenuation coefficient and backscatter term in intravascular optical coherence tomography images 27
3.1 Introduction . . . 28
3.2 Depth-resolved model analysis . . . 29
3.2.1 Depth-resolved attenuation . . . 30
3.2.2 Backscatter term estimation . . . 30
3.2.3 DR-CF cut-off algorithm . . . 31
3.3 Experiment and Implementation . . . 32
3.3.1 Data description . . . 32
3.3.2 Implementation . . . 34
3.3.3 Statistical analysis . . . 35
3.4 Results . . . 35
3.5 Discussion . . . 39
3.5.1 Attenuation coefficient . . . 45
3.5.2 Backscatter term . . . 48
3.5.3 IVOCT intensity . . . 49
3.5.4 Limitations . . . 50
3.5.5 Future directions . . . 51
3.6 Conclusion . . . 51

4 Histogram-Based Standardization of Intravascular Optical Coherence Tomography Images Acquired from Different Imaging Systems 53
4.1 Introduction . . . 54
4.2 Theory and terminology . . . 56
4.3 Materials and methodology . . . 58
4.3.1 Global and Local matching schemes . . . 58
4.3.2 Data description and alignment . . . 59
4.3.3 Dissimilarity between histograms . . . 61
4.3.4 Validation . . . 61
4.4 Results . . . 63
4.5 Comparing attenuation coefficient values . . . 67
4.6 Discussion . . . 68
4.6.1 Limitation . . . 69
4.6.2 Future work . . . 69
4.7 Conclusion . . . 70

5 Neointimal quality assessment of BVS and CoCr–EES 71
5.1 Introduction . . . 72
5.2 Methods . . . 73
5.2.1 Study design and population . . . 73
5.2.2 PCI procedure . . . 73
5.2.3 Optical frequency domain imaging analysis . . . 73
5.2.4 Statistical analysis . . . 76
5.3 Result . . . 76

5.3.1 Study subjects 76
5.4 Discussion 80
5.4.1 Head-to-head comparison of neointimal quality in previous publication 81
5.4.2 Light property analysis 82
5.4.3 Clinical implication 83
5.4.4 Strength and limitations 83
5.5 Conclusion 84
5.5.1 Impact on daily practice 84

6 Comparison of Visual Assessment and Computer Image Analysis of Intracoronary Thrombus Type by Optical Coherence Tomography in Clinical Patients 85
6.1 Introduction 86
6.2 Materials and Methods 86
6.2.1 Patients 86
6.2.2 OCT Imaging 87
6.2.3 Optical coherence tomography image analysis 88
6.2.4 Visual assessment of thrombus type 88
6.2.5 Computer image analysis of thrombus 88
6.2.6 Statistical analysis 89
6.3 Results 90
6.3.1 Qualitative thrombus classification by two observers 91
6.3.2 Reproducibility of quantitative measurements using QCU-CMS software 92
6.3.3 Comparison of visual TAS and measurements by QCU-CMS software 93
6.3.4 ROC analysis 100
6.4 Discussion 100
6.4.1 Limitations 103
6.5 Conclusions 104

7 Summary and Discussion 105
7.1 Summary 105
7.2 Discussion 107
7.3 Future work 109

Samenvatting 111
7.4 Discussie 113
7.5 Toekomstig werk 115

Bibliography 117

Publications 131

Acknowledgment 135

Curriculum Vitae **137**

CHAPTER ONE

INTRODUCTION

1.1 Coronary artery disease

Coronary arteries form a system of blood vessels that supply the heart muscle with oxygen and nutrients. Coronary Artery Disease (CAD) may cause a limitation and interruption in the blood supply, and may eventually cause myocardial tissue to die from oxigen and nutrient deprivation, a process also known as ischemic heart disease (IHD) [1]. Clinical symptoms include stable angina, unstable angina and ultimately myocardial infarction. The latter two are considered to be acute coronary syndromes (ACSs), which can result in sudden cardiac death. CAD is the leading cause of death worldwide, with an annual increasing rate of 0.38% [2]. According to a latest report from the World Health Organization (WHO), CAD was responsible for 7.4 million deaths in 2015, representing 13% of the overall global deaths [3].

In IHD, blood flow is restricted by two factors, vessel narrowing and thrombus. Both factors can be induced by atherosclerosis, which is a type of chronic inflammatory disease of the artery wall. [4, 5, 6] Although symptoms of CAD are presented mostly in people over forty, the development of asymptomatic plaques may start much earlier [7].

The healthy arterial wall is composed of three layers, the tunica intima (intima), the tunica media (media) and the tunica externa, also called tunica adventitia (adventitia), see Fig. 1.1. The media is mainly composed of smooth muscle cells. It is separated from intima by the internal elastic membrane (IEM), and from adventitia by the external elastic membrane (EEM). The intima is isolated from blood flow by the endothelium, which protects the vessel wall such that blood cells cannot clot on its surface.

Atherosclerosis is initialized by the endothelial dysfunction triggered by cardiac risk factors such as smoking, aging, hypercholesterolemia, hypertension, hyperglycemia and family disease history [9]. When patients are exposed to these factors, low density lipoprotein cholesterol(LDL-c) particles in the blood permeate into the intima. After a cascade of chemical reactions, they are oxidized to become toxic intruders, and trigger an inflammatory response. Macrophages assemble to engulf the oxidized LDL particles, but are immobilized due to the toxicity resulting in cell death. The increasingly collected fatty LDL-c and macrophages interact and gradually form a foamy, lipid-rich pool. Meanwhile, smooth muscle cells in media are permeated into the

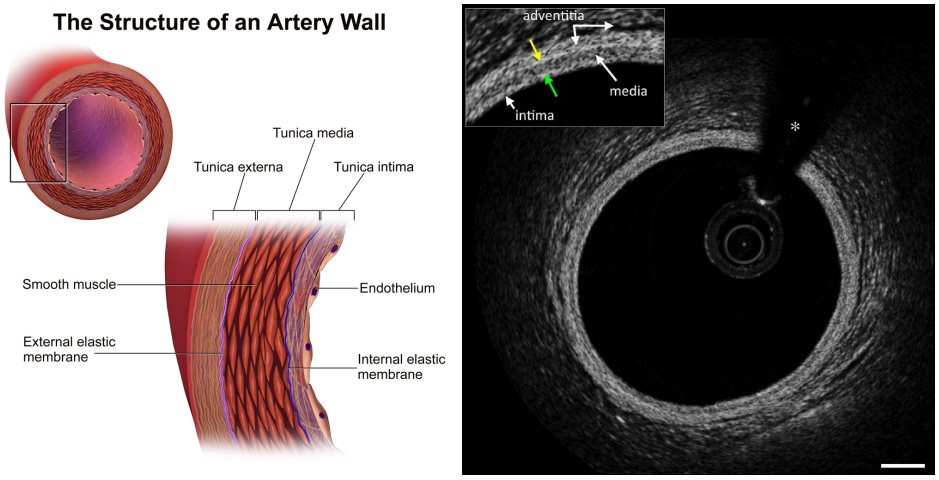

Figure 1.1: Left: Structure of an artery wall. *Blausen.com staff (2014). "Medical gallery of Blausen Medical 2014". WikiJournal of Medicine 1 (2). DOI:10.15347/wjm/2014.010. ISSN 2002-4436.* The tri-layer structure can be clearly observed in IVOCT as demonstrated in the right panel. The intima layer appears to be bright, attached with a dark media band and surrounded by the adventitia which is a bright layer and a dark heterogeneous layer. In the inset (x2), The IEM and the EEM are indicated with green and yellow arrows respectively. The scale bar at right corner marks 500 μm. Star * marks the Guide-wire shadow. Adopted from the consensus paper [8].

intima and form a fibrous cap on top of this lipid pool. Rather than narrowing the lumen, early and mid stages of plaque development tend to expand the vessel wall outwards (Glagov effect), and results in less flexible arteries.

In advanced plaque formation, dead macrophages form a large necrotic core and promote the inflammatory response further. The plaque starts to grow into the lumen and restrict the blood flow, the protective fibrous cap may become thinner and the plaque becomes vulnerable (i.e. susceptible to rupture). This vulnerable plaque is defined as thin-cap fibroatheroma (TCFA), featured as a large lipid pool covered with a thin fibrous cap less than 65μm thick and macrophage infiltration [8]. Upon a rupture or erosion of a TCFA, blood cells start to clot massively resulting in thrombus formation in the coronary artery. The clot can also drift along the blood flow and block other sites of arteries. Any of above scenarios can have catastrophic outcomes [10, 6, 11].

Stent placement is one of the routine therapies [12] during percutaneous coronary intervention (PCI). The culprit lesion is first diagnosed using angiography, then a stent is guided to the narrowing and expanded to reopen the coronary lumen, and locally maintaining a consistent radial support to keep the vessel open. The development of stents has greatly enhanced treatment options for coronary artery disease, and is one of the hallmarks of biomedical

engineering that has improved quality of life in patients with ischemic heart disease. Stents can be divided into three categories by their design: coiled, modular tube mesh and tubular slotted. According to the working mechanisms, stents are categorized to be the bare metal stents (BMSs), drug-eluting stents (DESs) and bioabsorbable vascular scaffold (BVS).

1.2 Intravascular optical coherence tomography

Undoubtedly, a better understanding of pre- and post-procedural development of plaques contributes to the prevention of CAD and improves diagnostic and therapeutic interventions. Intravascular optical coherence tomography (IVOCT) is at the moment the *in vivo* imaging modalities with the highest resolution to inspect the vessel wall composition, monitor stent deployment and treatment response [5, 14, 8, 15]. The center wavelength is around 1300 nm, which balances the acquired images with a high axial resolution and a reasonable penetration. The axial resolution is as high as $5-10$ μm. Meanwhile, the penetration depth is enough for the visualization of most ACS relevant structures including; plaque features such as lipid content, cap thickness, macrophages and microcalication, and stent features such as strut apposition, edge dissection, tissue protrusion, strut coverage and thrombus [16].

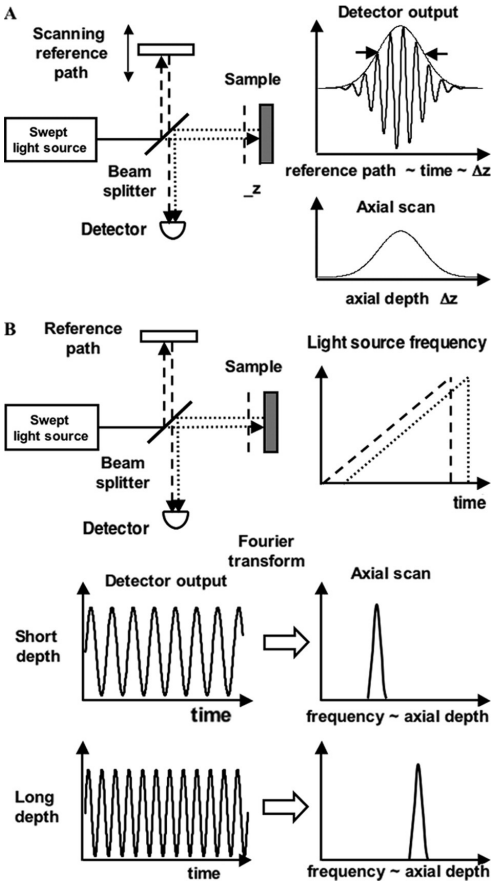

Figure 1.2: Schematic of time domain OCT and frequency domain OCT. Reprinted from [13]

The OCT images are acquired by sending light pulses towards the sample and then measuring the travel time of back-propagated light. The magnitude of received light is used to construct the image intensity at corresponding location. Because light travels at speed as high as 3×10^8 m/s, the measurement needs to be done with an interferometer (schematic can be seen in Fig. 1.2. The light source is split into reference beam and sample beam. The reference beam is sent to a mirror and reflected. The sample beam is sent to sample and part of it

will be backscattered at different depth (for interactions between light and tissue). The backscattered sample beam interferes with the reflected reference beam, then the locations and magnitude can be measured.

In early commercialized intravascular OCT systems, measurements are acquired using a time domain detection. The schematic is shown in Fig 1.2A. A broadband light source is used and location information was measured by moving the reference mirror to achieve interference. Nowadays, measurements are performed in frequency domain. The mirror is fixed and the wavelength of light source is swept quickly from 1250 nm to 1350 nm, and then frequency differences can be measured simultaneously. Knowing the swept time and the distance of the reference mirror, the travel distance of sample beam can be calculated with the measured frequency differences. The development of frequency domain OCT (FD-OCT) dramatically improves the imaging speed by ten fold.

Due to a high attenuation of light, blood needs to be removed during imaging procedural. In TD-OCT, this has been done either with consistent flush medium injection or distal medium injection in combination with a proximal balloon occlusion. With FD-OCT, the high imaging speed requires only transient blood removal by a bolus injection of flush medium at rates of 2–4 ml/s. An injection during 3 seconds allows the acquisition of OCT images in 60 millimeters artery.

The light is transmitted through the catheter tip onto the artery wall and the backscattered light is collected with a detector. One collected radial signal is called an A-line. A miniature rotary conjunction driven by a motor enables a sequence of A-lines to be acquired circumferentially. These A-lines can be stored either as a polar image or transformed into Cartesian coordinates. The former can be useful for signal analysis and the latter is usually used for visualization and quantitative measurements. By automated pullback of the catheter with a typical speed between 20 to 40 mm per second and a frame rate of 100 to 160 frames per second, a stack of images (pullback) is acquired.

1.3 Intravascular optical coherence tomography in clinical studies

The first pilot *in vivo* IVOCT study in patients was published in 2001 [17]. The tissue components in the coronary wall were visualized at an unprecedented resolution. The periprocedural arterial reaction was observed nearly real-time and measuring of the fibrous cap of TCFA was demonstrated. Together with studies of human cadavers and other patient studies [18, 19], fundamental reading guidelines of IVOCT image were formulated to identify common coronary structures including the three tunica layers, fibrous, calcific, lipid rich (atheroma) plaques with the fibrous cap accurately measured, macrophage infiltration, intraluminal thrombus. They are later organized in a consensus paper [8].

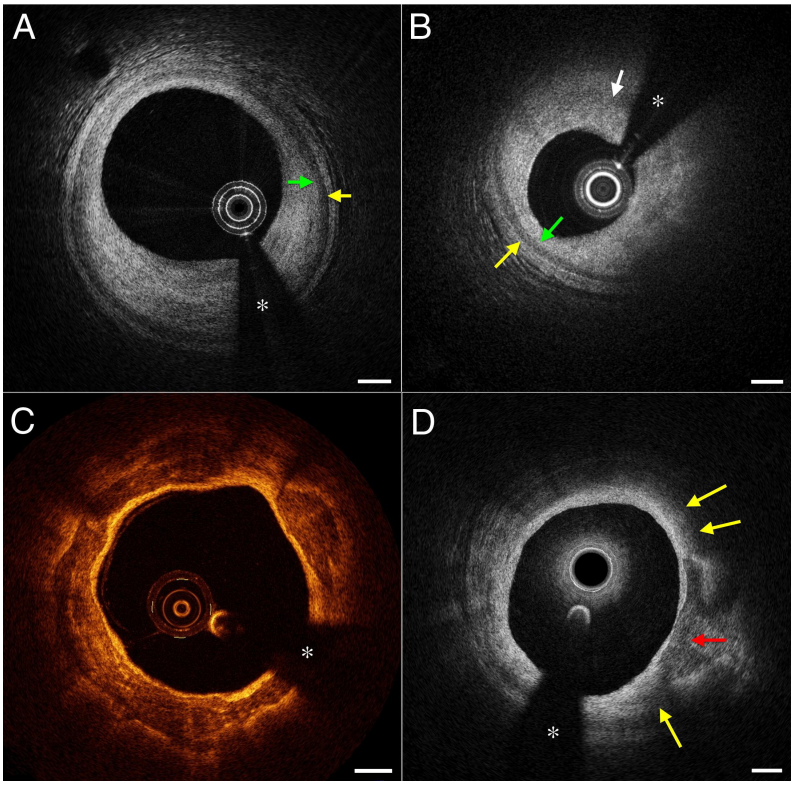

Figure 1.3: Plaque appearance in IVOCT images. (A) Moderate fibrous plaque where IEM (green arrow) and EEM (yellow arrow) can be observed. (B) Advanced thickened fibrous plaque without IEM or EEM can be observed (white arrow). The EEM (yellow arrow) and IEM (green arrow) can be clearly observed opposite to the advanced thickening region. (C) Calcified plaque appears as a circumferential low-signal region with sharp front borders. (D) Mixed plaque with focal calcific deposit (red arrow) adjacent to lipid plaques (yellow arrows). Scale bars mark 500 μm. Stars * mark the Guide-wire shadows. Adopted from the consensus paper [8].

As it is shown in the right panel in Fig. 1.1, the tri-layer structure for health artery wall can be clearly observed in IVOCT. The intima layer appears to be a signal-rich inner layer, attached with media which appears as a dark band, and is followed with the adventitia shown as a bright layer and/or a dark heterogeneous layer. The IEM and the EEM are considered to be at the boundaries of media. Fibrous plaques appear in IVOCT images as a a thickened homogeneous intima. The IEM and EEM can be observed in moderate plaque (Fig. 1.3A), but disappear in advanced thickening (Fig. 1.3B). A calcified plaque is characterized as a region with low intensity and delineated with sharp borders to fibrous tissue (Fig. 1.3C).

When the border of a low-signal region appears diffused, it is usually linked to a lipid plaque. Fig. 1.3D shows a mixed plaque with both a focal calcific deposition and a lipid plaque for concretely explanation. A fibroatheroma is a type of plaque with a large necrotic core under a fibrous cap. It appears as a signal poor region with diffused front border to a signal-rich cap (Fig. 1.4). Macrophage infiltration appears as concentrated bright dots.

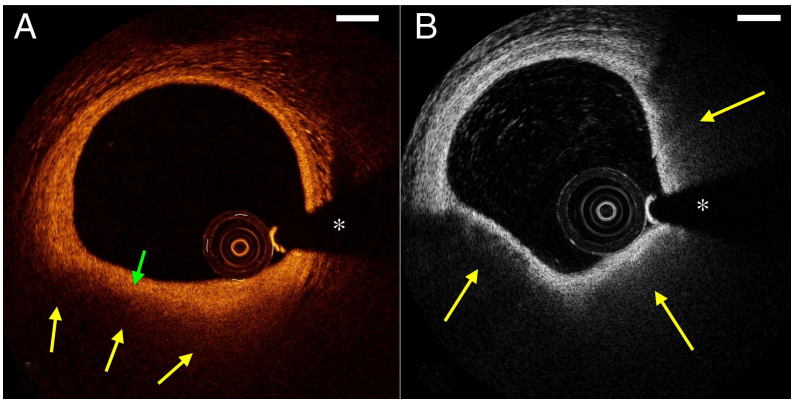

Figure 1.4: Fibroatheroma. (A) Fibroatheroma with signal-poor region (yellow arrows) covers about one quadrant artery wall with diffused front borders (green arrow). (B) Fibroatheroma covers more than 3 circumferential quadrants appears with region of low image intensities (yellow arrows). Scale bars mark 500 μm. Stars * mark the Guide-wire shadows. Adopted from the consensus paper [8].

These earlier studies suggested a convincing and promising clinical significance of IVOCT. An overview of plaque distribution of target artery can provide clinicians with an evaluation of stiffness and degree of atherosclerosis for planing the appropriate treatment. Since lipid content, fibrous cap and macrophage infiltration can be well observed, IVOCT can be an auxiliary tool for TCFA detection. For stent deployment, IVOCT is versed not only in tissue assessment for landing zone determination, but also in showing both short- and long-term post-stenting structures including tissue prolapse, stent thrombus, stent apposition and stent edge dissection. Periprocedure feedback of intraluminal event allows timely follow-up treatment, thus can prevent the recurrence of ASC and stenting failure in short period.

Long term follow-up OCT is usually not common, unless in case of ASCs are reclaimed or for a specific study purpose such as testing new medicinal therapeutic, treatment scheme or modified stent design. The healing process on the arterial wall is rather complex and slow, especially when interventions are involved. Stenting is 'a double-edged sword'. [20]: It may cause earlier recurrence of ACSs. Studies [21, 22, 23] shown that the following thrombotic incidents within short period (peri-procedual, a few hours and days) are significantly dependent on the type of overlaid plaques and the geometrical

properties of the chosen stent (length, thickness of struts, etc.) Late stent failure may occur resulting ISR and ST.

The fundamental reason for this is that stenting usually induces denudation of the endothelium, thus resulting in the exposure of intima to the blood flow, or worse: fissure in the cap of a TCFA, or tissue prolapse. The target artery may lose the natural curvature and become less flexible. Artery wall healing usually involves the progress of coverage of neointima over struts, but malapposed struts and stent fracture can cause an inflammatory response that delays the recovery. All these aforementioned factors may cause in-stent thrombus and stenting stenonsis, result in ACSs recurrence. Clinical studies have shown that late and very late stent failure may occur 5 years after implantation even for well recovered artery [24]. One important predictor is the redevelopment of atherosclerosis, also called neoatherosclerosis. [25] i.e., the atherosclerosis in the neointima. Though not a routine following clinical examination, IVOCT does offer an opportunity for long term monitoring and surveillance of post-PCI recovery of the artery. These information is useful for improving the design of stents and other therapeutic strategies.

Seeing the advantages in recognizing tissue components raises the question about IVOCT potential for PCI guidance. Clinical trials are still ongoing to compare IVOCT to other modalities for PCI guidance. One of the major issues for using IVOCT for PCI guidance is that vessel size at the lesion location can not be estimated due to its limited light penetration. In recent reported random trials [26], the reference size of the vessel was determined with healthy vessel sections at distal or proximal sites of the pullback, where at least 180° of external elastic membrane is supposed to be visible. In this study report, IVOCT was compared to two most common guiding tools for PCI, angiography and intravascular ultrasound (IVUS). Outcomes shown that IVOCT performs similar as IVUS and angiography when considering the minimum stent area, but results in less untreated major dissection and malapposition.

1.4 Tissue Characterization

The clinical prospects of IVOCT are promising. However, one OCT pullback usually contains several hundreds of images. Browsing through the whole pullback is thus time consuming and cumbersome. Therefore, an automated tissue analysis tool can both speedup clinical studies and benefit further clinical applications. Although tissue structures were reported to be recognized well in IVOCT images, developing a computer-based recognition framework remains challenging. Visual assessment of different types of tissue in the artery wall is based on the high sensitivity of human eyes to image intensities changes, such as from high to low sharply for calcified plaque or gradually for lipid-rich plaque, or isolated bright spots for macrophages. These changing patterns are because of the differences in refraction indices. However, the relative scale of variation in this index is usually small. For example, refractive indices of fibrous tissue, lipid pool and calcification were reported to be around 1.35, 1.43

and 1.50 for a light source with a center wavelength of 1320 nm. [27] This yields a high overlap for the quantification of different type of arterial tissue using image intensities. Not to mention that plaques in most cases are composed of mixed tissue types, and images are featured to a high noise level. Meanwhile, an image can be darkened due to the residual blood in the catheter, thrombus or optical translucent struts. In short, image intensity alone does not suffice for tissue quantification and quantification.

In the past decade, several optical parameters have been investigated, such as birefringence with polarization-sensitive (PS) OCT, attenuation and backscatter coefficient. Early works have show enhanced determination of plaques with attenuation and backscatter coefficient [27, 28] and more structure including collagen and smooth muscle cells, acute (red) thrombus and chronic (white thrombus) can be differentiated in PS OCT [29, 30]. Since PS OCT is still not generally available, the work in this thesis focuses on optical parameters which can be derived from regular OCT intensities.

1.4.1 Optical properties

When light travels through biological tissue, it is absorbed and scattered. Light absorption is a process in which the incident optical power (electromagnetic energy) is converted into some inner energy of tissue particles, such as thermal energy. Another tissue-light interaction is scattering. When traveling through a medium, light can be scattered in all directions due to the interaction of photons and particles (scatterers) in the tissue. If kinetic energy is conserved, the scatter is elastic, otherwise nonelastic scatter takes place. For NIR light in biological tissue, the elastic scatter is dominant. Since forward propagating light is attenuated due to both absorption and scattering, the attenuation coefficient is defined as the sum of the absorption and scattering coefficients, $\mu_t = \mu_a + \mu_s$. The center wavelength of the currently used IVOCT is 1300 nm, at which the scatter coefficient in arterial tissue is much larger than the absorption coefficient.

In practice, biological tissue can be composed of various types of particles such as cells of different forms, extracellular matrix and multiple types of molecules. Optical attenuation for these particles can also differ with minor changes in temperature, respiration, activity and nutritional intake. It is impractical to determine the attenuation for each type of particles, thus μ_t in tissue optics usually represents a bulk attenuation coefficient for a certain type of tissue.

For homogeneous tissue the Lambert-Beer law is often used to calculate the attenuation coefficient.

$$I(d) = I_0 \cdot e^{-\mu_t d} \tag{1.1}$$

For heterogeneous tissue, the attenuation can be modeled as a depth-dependent function, then Eq. 1.1 becomes:

$$I(d) = I_0 \cdot e^{-\int_0^d \mu_t(x)\mathrm{d}x} \tag{1.2}$$

The exponential decrease is valid with a single scatter assumption. Namely, light is considered to be scattered once. In practice, light can be scattered multiple times, which contributes to its forward and backward propagation. The multi-scatter is inhibited at the focal point and becomes stronger as it is further away from the focal point location. In IVOCT the focal point is designed to be around the lumen wall. Therefore, an IVOCT A-line is usually modeled with a single scatter model in combination with a system-related terms. The model can be then used for the estimation of attenuation. When Eq. 1.1 is used, the attenuation coefficient is assumed to be the same within one type of tissue and then can be estimated with curve fitting procedure. When Eq. 1.2 is used as a decrease term, the model is called depth-resolved (DR) model.

The appearance of each type of tissue can be explained with its attenuation and backscatter properties [27]. The fibrous plaque appears to be bright homogeneous region because it has hight backscatter but low attenuation. The calcified plaque is characterized as a signal poor region with well delineated borders, because both its attenuation and backscatter are low. Low attenuation allows a deeper penetration of light which explains that the backside border and structures being visible for moderate fibrous plaques and small calcified plaques. A lipid-rich region has both high attenuation and backscatter. When light travels though the boundary of fibrous cap and lipid, detected signal stays high due to the high backscatter of lipid, which explains the diffused border. Meanwhile, the light power is dramatically decreased within a short distance due to high attenuation, resulting in low-signal region and invisible backside border. The attenuation and backscatter properties can be used for the differentiation of the arterial tissue types.

Until now, region-based curve-fitting approach for the estimation of attenuation coefficient is dominantly used for tissue analysis. Fitting ranges are determined either manually or automatically. Manual determination results in a low reproducibility, while automated determination yields a high reproducibility yet suboptimal segmentation and resolution. On the other hand, DR estimation overcomes these drawbacks by estimating attenuation coefficients for each pixel. Because of the preserved structure and resolution, pixel-wise estimation is very promising for further analysis and algorithm development. However, due to its being recently proposed, limit work has been done.

1.5 Outline of the thesis

The aim of this thesis is to develop a pipeline for IVOCT tissue analysis using estimation based on the depth-resolved model. In particular, we address the following specific aims: 1) to investigate catheter position effects on the IVOCT image intensities. 2) to validate the DR algorithm for characterizing intravascular tissue structures. 3) to develop a framework to standardize the IVOCT image intensity from different systems to compare outcomes. 4) to apply the DR algorithm for estimating attenuation and backscattering effects in

IVOCT images. The thesis is structured as follows:

Chapter 2 aims to analyze the effect of the catheter position on IVOCT image intensities and proposes a compensation method to minimize this effect in order to improve the visualization and the automatic analysis of IVOCT images. The effect of catheter position is modeled with respect to the distance between the catheter and the arterial wall (distance-dependent factor) and the incident angle onto the arterial wall (angle-dependent factor). A light transmission model incorporating both factors is introduced. On the basis of this model, the interaction effect of both factors is estimated with a hierarchical multi-variant linear regression model.

Chapter 3 explores the estimation of the attenuation coefficient and a backscatter term, and in combination with image intensities to distinguish different atherosclerotic tissue types with a robust implementation of depth-resolved (DR) approach. In order to exclude noisy regions with weak signal, an automated algorithm is implemented to determine the cut-off border in IVOCT images. Referring to the histopathological images, the attenuation coefficient, backscatter term and the image intensity are further analyzed in regions of interest. Local statistics were reported and their distributions were further compared with 2-sample t-test to evaluate the potential for distinguishing six types of tissues.

Chapter 4 focuses on developing an intensity mapping framework to match intensities based on an exact histogram matching technique to overcome the difference in the intensity range and distribution between different IVOCT systems. The matching accuracy is analyzed using leave-one-out validation and quantified at both histogram and intensity levels.

Chapter 5 aimed to quantitatively assess the neointimal quality after BVS implantation in comparison with CoCr-EES by optical frequency domain imaging (OFDI). This study is a post-hoc analysis of TROFI II randomized controlled trial focusing on the quantitative neointimal quality assessment 6-month after the implantation of BVS and CoCr-EES in ST elevation myocardial infarction (STEMI) patients. The fully automatic light property analysis of the attenuation, backscatter and light intensity was performed for superficial and deep neointima separately.

Chapter 6 aims to compare the newly developed optical property analysis method to the subjective visual classification of intracoronary thrombus type using optical coherence tomography (OCT) imaging. Thirty patients with myocardial infarction and OCT imaging of the thrombotic culprit lesion were included. The thrombus type was evaluated by two independent readers. For comparison, the same OCT images were analyzed using DR algorithm. Two observer consensus was considered the golden standard for the receiver operating curve (ROC) analyses

Chapter 7 In Chapter 7, the overall achievements of this thesis are summarized and discussed.

CHAPTER TWO

ANALYSIS AND COMPENSATION FOR THE EFFECT OF THE CATHETER POSITION ON IMAGE INTENSITIES IN INTRAVASCULAR OPTICAL COHERENCE TOMOGRAPHY

Abstract — Intravascular optical coherence tomography (IVOCT) is a novel technique, which is used to analyze the underlying cause of cardiovascular disease. Because a catheter is used during imaging, the intensities can be affected by the catheter position. This work aims to analyze the effect of the catheter position on IVOCT image intensities and propose a compensation method to minimize this effect in order to improve the visualization and the automatic analysis of IVOCT images. In this paper, the effect of catheter position is modeled with respect to the distance between the catheter and the arterial wall (distance-dependent factor) and the incident angle onto the arterial wall (angle-dependent factor). A light transmission model incorporating both factors is introduced. On basis of this model, the interaction effect of both factors is estimated with a hierarchical multi-variant linear regression model. Statistical analysis shows that IVOCT intensities are significantly affected by both factors with $p < 0.001$, as either aspect increases the intensity tends to decrease. This effect differs for different pullbacks. The regression results were used to compensate for this effect. Experiments show that the proposed method can improve the performance of the detection of the bioresobable vascular scaffold struts.

This chapter was published as: S. Liu, J. Eggermont, R. Wolterbeek, A. Broersen, C.A.G.R. Busk, H. Precht, B.P.F. Lelieveldt and J. Dijkstra. **Analysis and Compensation for the Effect of the Catheter Position on Image Intensities in Intravascular Optical Coherence Tomography**, *J. Biomed. Opt.*, Volume 21, Issue 12, Pages 126005, 2016.

2.1 Introduction

Cardiovascular disease (CVD) is a major cause of death worldwide [31]. One of the underlying processes that cause CVD is atherosclerosis, which is the long-term accumulation of plaque in the vessel wall. The extent and composition of atherosclerosis can be visualized in-vivo with intravascular optical coherence tomography (IVOCT) at a higher resolution of 10 to 20 μm [8, 32, 33] compared to other in-vivo imaging modalities, such as Intravascular Ultrasound (IVUS), Computed Tomography Angiography (CTA) or Magnetic Resonance Imaging (MRI).

IVOCT is an optical imaging modality using near-infrared (NIR) light as the imaging source. The images are acquired using a catheter which is inserted into the coronary artery. Images of arterial cross-sections are reconstructed from the echo time delay and the intensity of back-scattered light. Due to the high scattering of NIR light in blood caused by red blood cells, the artery is flushed with saline or a contrast medium to clear the blood inside the artery. The image intensity is assumed to be only tissue dependent, thus different types of tissue appear different [8].

In practice, however the signal magnitude may not only be dependent on the tissue type, but also on the position of the catheter with respect to the vessel wall, which causes non-tissue-related effects on the IVOCT image intensities [34, 35]. An example is given in Fig. 2.1. The average intensities are calculated within the thin superficial uniform layer of the IVOCT image of a non-pathological artery segment. Nevertheless, there is a clear variation in the profile of the average intensities (Fig. 2.1 b).

The importance of analyzing the effect on intensities caused by the position of the catheter has been well depicted in the field of IVUS. Courtney et al. showed that the IVUS image intensities are strongly related to the catheter position [36]. Their study concluded that when the distance or the angle towards the luminal wall increases, the intensity will decrease for both intima-media tissue and adventitia tissue. Earlier work [37, 38, 39] shows that the reflected ultrasound signal is critically dependent on the angle of incidence and varies for different types of arterial plaques.

In the literature of IVOCT image analysis, statistical values of the intensities are commonly used as key features for both automated detection algorithms and the quantitative studies. For example, mean intensity has been applied as one of the textural features for automated tissue characterization [40]. A recent stent strut detection algorithm has been proposed to train a supervised artificial neural network classifier with statistical features including the maximum, mean, median intensities, etc [41]. Furthermore, the percentiles values of the distribution are often used as thresholds. For example, the 5th percentile has been used as the threshold for noise removal [42, 43, 44, 45]. More percentiles were used as cutoff values to determine the trailing shadow [46, 44] for metal strut detection, and the black core regions [47] for the detection of the bioresorbable vascular scaffold (BVS) strut. With the assistance of the BVS strut detection, median values and peak values within the black core

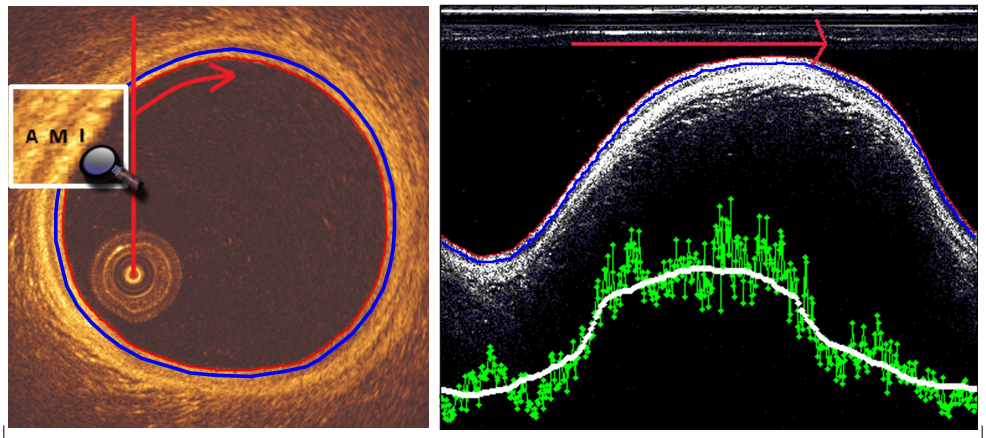

Figure 2.1: (a): An IVOCT image of a non-pathological artery wall: the artery has a regular and almost circular shape; three arterial layers, intima (I), media (M) and adventitia (A), are clearly visible (as shown in zoomed-in top-left corner). (b): Polar representation of the image in (a) sampled clockwise along radial A-lines from the catheter center shown as a bright line on the top of the image. For each A-scan, the average intensity within a superficial thin layer ($\approx 50\mu m$) is calculated and shown as the green profile. The white curve is the smoothed green profile.

region were quantitatively analyzed to track the variation of the BVS struts in post stenting and follow up IVOCT images at 6, 12, 24 and 36 month respectively.

However, effected by the catheter position, the distributions of the intensities can appear different, which may increase the variation of those statistical numbers. The amount of the variation cause by the catheter position depends on the extent of its eccentricity. Further quantitative analysis of this effect can be helpful to develop a algorithm to compensated for it. To the best of our knowledge, only one study with respect to the effect of light incident position on OCT image intensities has been reported about that a non-perpendicular incident light cause a significant variance in the measurement of the articular cartilage [35]. In the followup studies of the bioresorption progress of the BVS strut, the bias in light intensity caused by the eccentric catheter was claimed to be minimized with normalization, yet involve more manual input and time consuming. On the other hand, results from IVUS cannot be applied directly to IVOCT, due to the differences in physical properties between both modalities.

The aim of this work is to analyze the effect of the catheter position, with regards to both the distance to the vessel wall and the incident angle of light, on IVOCT image intensities. Based on this analysis a compensation algorithm is proposed to reduce this effect. As an application of compensated images, images

with foam cells have been enhance and compared with histological slides. Furthermore, the compensation algorithm is used in combination with an existing BVS detection algorithm.

The general structure of the paper is as follows. In 2.2.1, a light transmission model incorporating both distance-dependent and angle-dependent factors is introduced. In 2.2.2, a hierarchical multi-variant linear regression model is proposed to further investigate the relationship and estimate the both factors. The regression result is further used in 2.2.3 to propose a method to compensate images. Results are presented in Section 2.3. The compensated images were inspected comparing to the pathological images in 2.4.1. Furthermore, a BVS struts detection experiment with the compensated images was carried out in 2.4.2. All the experiments and results are discussed in Section 2.5 with limitations and the future works given as well. Conclusions are drawn in Section 2.6.

2.2 Materials and Methodology

Images of non-pathological segments from 9 IVOCT pullbacks recorded with a C7XR swept-source OCT system and a C7 Dragonfly Imaging Catheter (St. Jude Medical, Minnesota, USA) were used. The technical details are listed in Table 2.1 and Table. 2.2.

Table 2.1: Technical details of the IVOCT system

swept laser source	center wavelength	1310 nm	wavelength range	110 nm
	sweep rate	50 kHz	output power	20 mW
	coherence length	12 mm		
pullback	pullback speed	20 mm/s	pullback length	54 mm
frames	image frames	271	frame rate	0.2 mm

Table 2.2: Number of selected frames in each pullback

Pullback No.	1	2	3	4	5	6	7	8	9	Total
No. of Frames	28	17	33	21	5	13	14	29	9	169

2.2.1 Distance and Incident Angle Extended Light Transmission Model

A schematic overview of light propagation for IVOCT imaging is shown in Fig. 2.2. The lights emitted from the catheter first travels through the flush medium before reaching the arterial wall with a distance denoted as x_t. At the interface between the flush medium and the arterial wall, both reflection and refraction occur. θ represents the incident angle of the light entering the arterial wall. Δx represents the light transmitting distance of the refracted

light beam inside the arterial tissue. For the convenience of explanation, we introduce $x = x_t + \Delta x$.

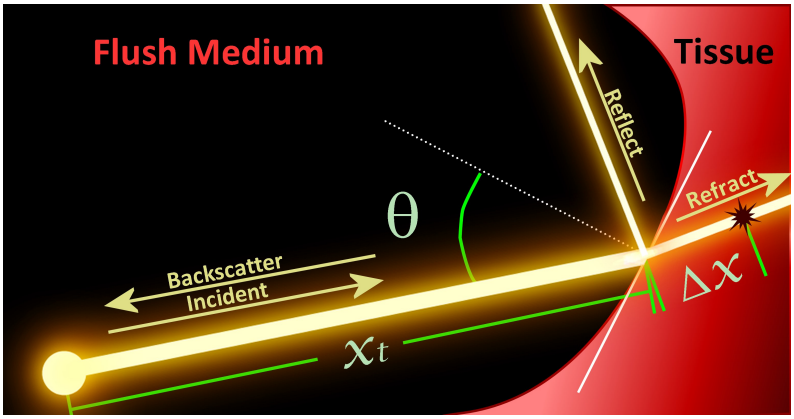

Figure 2.2: Light transmission. x_t denotes the distance between the light source and the arterial wall, Δx denotes the distance between the arterial wall and the detected position inside the arterial tissue, and θ is the incident angle of the light beam.

2.2.1.1 Light Transmission Model

As the light propagates inside the arterial wall, the intensity of an OCT signal is typically modeled as the first order scattering function of x and Δx as [48]:

$$I_b(x) \cong \frac{1}{2} I_{in} \mu_b T(x) \cdot e^{-2\mu_t \Delta x}, \tag{2.1}$$

where I_{in} denotes the light intensity upon entering the arterial wall. $I_b(x)$ denotes the back-scattered light intensity from the distance x. μ_b represents the back-scattering coefficient, and μ_t is the total attenuation coefficient (summation of scatter and absorption). $T(x)$ is the confocal function which is defined as [28]:

$$T(x) = \left[\left(\frac{x - z_0}{z_R} \right)^2 + 1 \right]^{-1}. \tag{2.2}$$

where z_0 and z_R are the beam waist and the Rayleigh length, respectively.

The intensity entering the luminal wall is affected by two factors; the attenuation in the flush medium region (FMR), and the reflection and refraction at the interface of flush medium and the arterial wall. In a well-flushed artery, the FMR region can be regarded as homogeneous, non-scattering and weakly attenuating, obeying the Lambert-Beer law [49]. With a constant attenuation, μ_f, the light decay is determined by the distance from the catheter to the lumen wall, x_t.

The interaction of the light is more complex at the interface between FMR and the lumen tissue due to the relative irregular surface of the arterial wall. To analyze the effect of the incident angle on image intensities, the total effect of the incident angle is normalized into 0 to 1 by using a term similar to the Fresnel transmission ratio. Thus I_{in} is modeled as:

$$I_{in} \sim I_0 \cdot Tr(\theta, n_i, n_t)^{\beta_2} \cdot e^{-\mu_f x_t}. \tag{2.3}$$

where β_2 is the parameter to be estimated. $Tr(\theta, n_i, n_t)$ is the Fresnel like function which is calculated with the incident angle θ, index of refraction of the incident medium n_i and transmission medium n_t, respectively [49]. With Eq. 2.3 substituted in Eq. 2.1 and taking the logarithm from both sides results in:

$$\ln I_b(x) \cong -\mu_f x_t + \beta \ln Tr(\theta, n_i, n_t) + \ln T(x_t + \Delta x) - 2\mu_t \Delta x + C(I_0, \mu_b). \tag{2.4}$$

where $C(I_0, \mu_b) \cong \ln(I_0 \cdot \mu_b)$ is a constant term.

2.2.2 Parameter estimation of the linear model with Hierarchical linear regression

2.2.2.1 Hierarchical linear regression

Hierarchical linear models are specifically utilized for data with hierarchical structures [50]. Here, a hierarchical linear model is designed to analyze the potential relationship between OCT image intensities and three factors; distance: (x), angle: $\ln Tr(\theta, n_i, n_t)$ and the constant term $C(I_0, \mu_b)$. The linear model for regression is:

$$\ln I_b(x) = \beta_0 + \beta_1 \cdot x + \beta_2 \cdot \ln Tr(\theta, n_i, n_t). \tag{2.5}$$

In order to keep the consistency of the notations, the parameters were denoted as β_0, β_1 and β_2. The A-lines can be hierarchized into different frames, which in turn can be hierarchized into different pullbacks. Based on this observation, a three-level linear model is considered for this study (see Fig. 2.3).

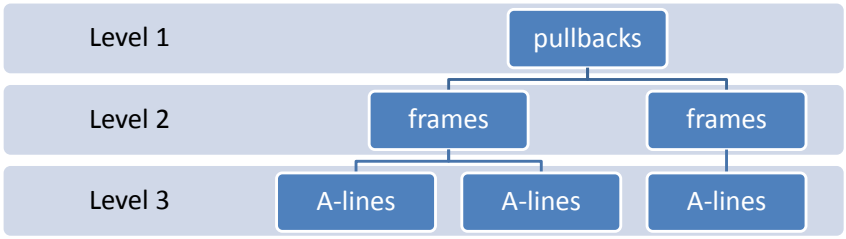

Figure 2.3: Multi-level linear model

2.2.2.2 Implementation

The lumen border in the Cartesian images was used to estimate the incident angle. To compensate for the polar to Cartesian transformation, the lumen border points were resampled with respect to the depth. The angle was calculated in a window of 9 points.

The index of refraction of the flush solution is 1.449 mm (read from the stored data). The refraction index of intima is about 1.358 mm [51]. Therefore the incident angle is the only variable during the calculation of the transmission ratio for each point.

Intensities of only a thin inner layer of the arterial wall are used for the statistical analysis, then $\Delta x \approx 0$, and thus $x = x_t + \Delta x \approx x_t$. The general trend of the signal regards to the distance x_t is decreasing due to both the attenuation of the flush medium and the confocal function. Approximating this term as linear, the object model for hierarchical linear regression can be written as:

$$\ln I_b(x) = C(I_0, \mu_b) + \beta_1 \cdot x_t + \beta_2 \ln Tr(\theta). \tag{2.6}$$

This can be equalized to the hierarchical linear regression model if we denote $\beta_0 = C(I_0, \mu_b)$, thus the linear regression can be used to investigate the linear relationship regarding the distance and the incident angle.

2.2.3 Compensation

The linear model which describes the effect of the catheter position can also be used for the compensation of this effect.

Based on the linear regression model, the primary goal for the compensation is to normalize the IVOCT image intensities within the superficial layer of the non-pathological artery. This can be achieved with the following equation involving the regression result:

$$I_{compensated}(y) = \frac{I_{original}(y) \cdot e^{\hat{\beta}_0}}{I_b(x)}. \tag{2.7}$$

As defined, $I_{original}(y)$ and $I_{compensated}(y)$ denote the original and the compensated IVOCT signals at the depth y. β_0 is the estimated constant term in the regression model. With a thin layer with thickness Δx selected, $I_b(x)$ is the average intensity within the superficial thin layer:

$$I_b(x) = \int_{y=x_t}^{x_t+\Delta x} I_{original}(y)/\Delta x. \tag{2.8}$$

Noting the following mathematical equation holds,

$$I_b(x) \sim \hat{\beta}_1 \cdot \int_x^{\infty} I_b(t)\, dt, \tag{2.9}$$

where $\hat{\beta}_1$ is the estimated parameter. The intensities can be normalized as follows:

$$I_{compensated}(y) = \frac{I_{original}(y) \cdot e^{\hat{\beta}_0}}{\hat{\beta}_1 \cdot \int_x^{\infty} I_b(t)\, dt} \cong \frac{I_{original}(y) \cdot e^{\hat{\beta}_0}}{\hat{\beta}_1 \cdot \sum_x^{M} I_b(t)}. \tag{2.10}$$

Here M is a large depth selected far enough away from the lumen border. Noting that:

$$\sum_{y=x}^{M} I_{compensated} = \frac{e^{\hat{\beta}_0}}{\hat{\beta}_1} = constant, \tag{2.11}$$

the principle of this compensation method is to normalize the summation of intensities behind the lumen border. Since arterial tissues are strong scattering and weak absorbing, the summation of the IVOCT intensities should be approximately constant (linearly related to the total emitting energy from the catheter) for most arterial tissue types, thus this method is not limited to only compensate the IVOCT images of non-pathological arteries.

2.3 Results

2.3.1 Hierarchical linear regression

The hierarchical linear regression considers three fixed effects and two random effects. The F-tests result for each of the fixed effects specified in the model indicate that all three effects contribute to the model statistically significantly with $p < 0.001$.

Table 2.3: Estimates of Fixed Effects[a]

Parameter	Estimate	Std.Error	*df*	*t*	*Sig.*	95% Confidence Interval	
						Lower Bound	Upper Bound
β_0	6.512	0.162	8.013	40.318	0.000	6.140	6.884
β_1	-0.00227	0.000	79838	-279.2	0.000	-0.00229	-0.00226
β_2	2.818	0.073	80041	38.848	0.000	2.676	2.960

a. Dependent Variable: Natural logarithm of Intensities.

Table 2.3 shows the results of the fixed model. It was found that the constant related to light source ($\beta_0 = 6.5121, SE = 0.1615, p < 0.001$), the distance between catheter and artery wall ($\beta_1 = -0.0023, SE = 0.0000, p < 0.001$) and the logarithm of 'Fresnel' transmission ratio ($\beta_2 = 2.8178, SE = 0.0725, p < 0.001$) – all were significant predictors.

Table 2.4 shows the results for the two random factors and residual covariance matrices. Results indicate that both of the defined random effects - the frame number ($Nu = 0.0060, SE = 0.0007, p < 0.001$) and pull-back number ($Nu = 0.2342, SE = 0.1173, p < 0.05$)– contribute to the covariance statistically

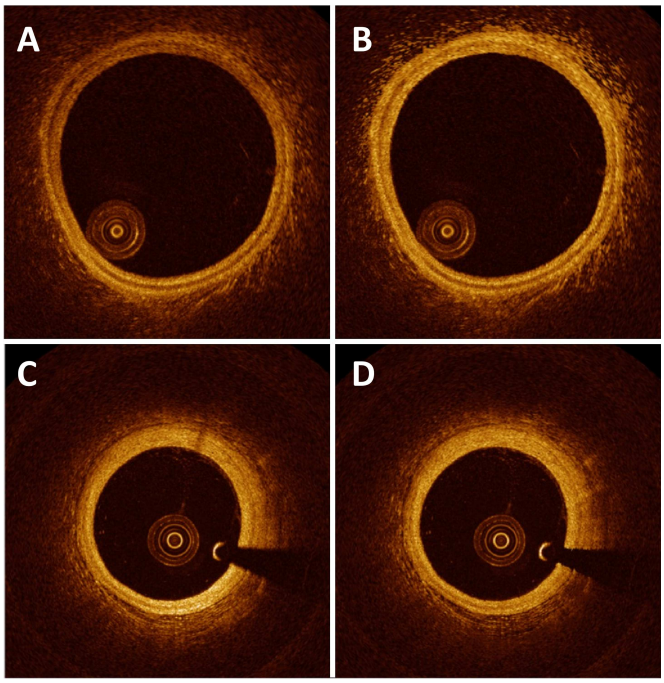

Figure 2.4: **A** and **C** are the images before compensation and on the right side **B** and **D** are the compensated images. The image in **A** is a clear example of the effects caused by the eccentric position of the catheter, the compensated image **B** shows more evenly distributed intensities around the artery wall. In the second example **C**, the light intensities are more or less homogeneous but there is information missing at 1 o'clock. After compensation, the shadow region is removed (**D**).

significantly with almost two thirds of the total variance. However, the influence of the frame number is relatively very small ($\sim 1.6\%$) compared to the other contributors. Based on this observation, this random effect can be ignored during modeling.

The histogram of the residual ($Epsilon = 0.1276, SE = 0.0006, p < 0.0001$) is distributed symmetrically around zero with a mean value of -$2.01E-11$ and a standard deviation of 0.3568, thus indicating the model can fit the data well.

2.3.2 Compensation

With the results of the linear regression, images can be compensated using Eq 2.10 proposed in Section 2.2.3. Figure 2.4 demonstrates the compensation of IVOCT images of non-pathological arteries. The non-uniform image intensities behind the lumen border and even a small shadow artifact on the lumen wall were compensated. The non-uniform image intensities and even a small

Table 2.4: Baseline patient characteristics (n = 30)

Parameter		Estimate	*Std.*	Wald Z	*Sig.*	95% Confidence Interval	
						Lower Bound	Upper Bound
Residual		0.128	0.001	199.864	0.000	0.126	0.129
Intercept[Frame]	Variance	0.006	0.001	8.541	0.000	0.005	0.008
Intercept[Pull-back]	Variance	0.234	0.117	1.997	0.046	0.088	0.625

a. Dependent Variable: Natural logarithm of Intensities.

unusual shadow on the lumen wall were compensated.

2.4 Application of the compensated images

2.4.1 Pathological images with foam cells

The performance of compensated algorithm is compared with histological cross sections. Selected frames from two ex-vivo OCT pullbacks on explanted hearts [52] were used. OCT imaging was performed with the Ilumien PCI Optimisation system and a C7 Dragonfly Imaging Catheter of LightLab Imaging, St. Jude Medical, Minnesota, USA. The proximal 5 cm of the vessels were cut out and standard paraffin embedding was performed. For every 200 μm, 3 μm-thick sections were cut and stained with haematoxylin-eosin. These slices were annotated by a pathologist and matched with the corresponding OCT frames based on anatomical landmarks.

Two examples with bright spots are given in Fig. 2.5. In Fig 2.5 A-C, the image intensities marked with red arrows were darkened due to the residual of blood within lumen. In the compensated image, the darkened regions were compensated and the edges between the calcified region and the fibrous region are more clear. In Fig 2.5 E-F, the image regions near side branches were darkened due to the eccentric catheter position. The foam cells, marked with the red arrows, are more accentuated in the compensated image than in the original image.

2.4.2 BVS strut detection

In order to examine the performance of the compensation algorithm for automated image segmentation, it is tested combining with the BVS detection proposed by Wang et al [47]. For this purpose, 8 post-stenting follow-up pullbacks were used which were acquired with a C7-XR imaging system and C7 imaging catheter (St. Jude Medical Inc., St. Paul, MN, USA) at 6-12 months. All the stent struts are the ABSORB 1.1 BVS (Abbott Vascular, Santa Clara, CA, USA). The ground truth (GT) data contains 7933 black cores in total.

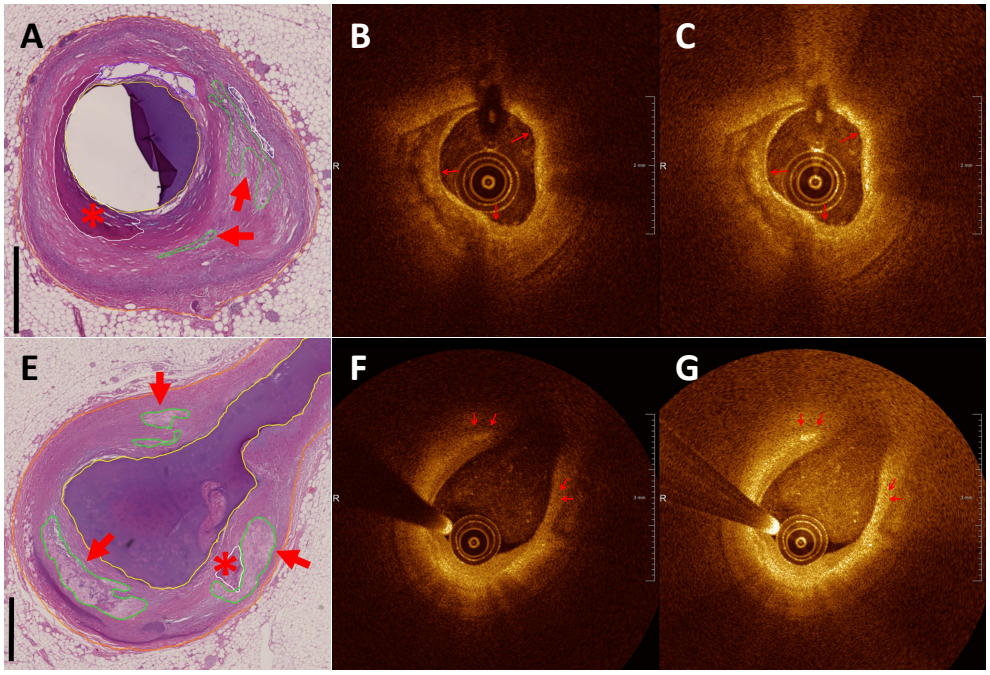

Figure 2.5: Demonstration of the effect of compensation. From right to left are histology images, original IVOCT images and compensated images. In the histology images, red arrow indicates the location with form cells, and stars mark the calcified lesions as landmarks. The original and the compensated images are displayed at the same contrast and brightness level, and the red arrows mark noticeable regions for comparison.

For a impartial comparison, the compensated pullbacks were rescaled linearly by aligning the 99.5 percentile value of the histogram to that of the original pullbacks, thus the same parameters can be applied. The results were evaluated by counting the true positive (TP), the false positive (FP), false negative (FN), and the F-score was calculated as the measurement of the detecting performance [53].

With the described data and experimental settings, the compensated images were used for automatic BVS strut detection. The detection results can be seen in Table 2.5, where the outperformed F-score is marked with bold font. An example of improved BVS detection image can be seen in Fig 2.6.

2.5 Discussions

The aim of this work is to investigate the influence of the position of the catheter on IVOCT intensities and to use this knowledge to compensate for it. Two aspects of the catheter's position were analyzed, the distance between the catheter and

Table 2.5: The stent struts detection results

Data set	No. of GT	Original Pullback (%)				Compensated Pullback (%)			
		TP	FP	FN	*F*-score	TP	FP	FN	*F*-score
1	776	86.5	21.4	13.5	**83.2**	88.9	27.3	11.1	82.2
2	891	94.2	8.5	5.8	92.9	95.2	6.7	4.8	**94.3**
3	1158	82.6	2.7	17.4	89.1	83.9	2.3	16.1	**90.1**
4	910	78.2	1.4	21.8	87.1	88.8	0.8	11.2	**93.7**
5	1389	91.9	8.9	8.1	91.5	95.2	6.9	4.8	**94.2**
6	847	85.0	22.8	15.0	81.8	89.7	19.4	10.3	**85.8**
7	1059	81.7	17.2	3.6	88.7	80.6	9.3	4.6	**92.1**
8	903	96.6	4.3	3.4	**96.1**	96.1	4.1	3.9	96.0
Total	7933	87.2	10.4	10.9	89.1	89.8	8.8	8.3	**91.6**

GT: ground truth; TP: true positive; FP: false positive; FN: false negative
F-score = 2TP/(2TP+(FN+FP))

the arterial wall, and the angle of incidence of the light penetrating the arterial wall.

2.5.1 Hierarchical linear regression

The statistic analysis focuses on intima-media regions on the artery wall, thus the tissue-dependent effects were minimized in the study. Similar region selection criteria have been used by Courtney on IVUS images [36]. The statistical results show that the amount of light that enters the artery wall is significantly related to the catheter position. In the linear model, an angle related transmission ratio has been used to model the trend. The trend of this transmission ratio is conforming to empirical observations.

As the angle of incidence increases, the IVOCT intensities decrease accordingly. The more the angle of incidence approaches to a critical angle, the faster the IVOCT intensities decrease. When the angle of incidence approaches this critical angle, light propagation into the tissue in the artery wall is limited. This can explain the 'signal dropout' reported by van Soest et al [34]. When the incident angle becomes equal or even larger than the critical angle, there is no light entering the artery wall, and thus the transmission ratio will be zero. This results in the appearance of disconnecting tissue along the arterial wall, which has been reported as dissection artifacts in an IVUS study by Mario et al [39].

As random variables, the pullback number and frame number contribute to the hierarchical linear model significantly in terms of covariance. The covariance contribution of frame number is relatively small enough to be ignored. The covariance of the pullback number occupies almost two thirds of the total covariance. Since the same flush medium was used, this suggests that the distance-dependency can differ between IVOCT imaging catheters. This confirms the statement of van Soest et al., that the parameters of catheters differ from each other [28].

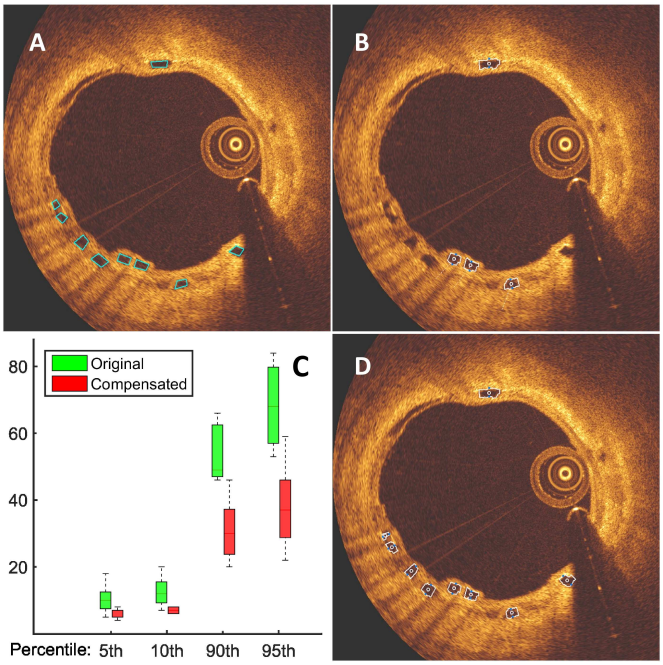

Figure 2.6: An example of image with improved BVS detection. **A.** The cross section with ground truth BVS delineated with cyan color. **B.** Detection results with the original image delineated with white color. **D.** Detection results with the compensated image delineated with white color. Within each black core of the ground truth, the percentile of both original and compensated image can be seen in **C**.

2.5.2 Compensation

The compensation of the intensities in the OCT images can enhance the visualization of arterial tissues in IVOCT images. An eccentric position of the catheter or the residual blood inside the lumen can result in inhomogeneous intensity in homogeneous tissue, which requires the contrast and brightness levels to be constantly adjusted during visual inspection. Our proposed compensation algorithm improves the visualization by balancing the signal levels within each pullback, which can be seen in both in-vivo (Fig. 2.4 and ex-vivo images (Fig. 2.5).

Noting in Fig. 2.5 C and D, a shadow artifacts caused by the residual blood in the protective sheath were compensated as well. This is because our compensation algorithm compensates the total energy behind the lumen border for each A-line. The shadow artifacts caused by factors within the lumen, eg. residual blood, thromobosis etc., may cause a sudden drop of the total energy comparing to A-lines in the neighborhood. Therefore, normalizing the total energy can compensate such local shadow artifacts as well. The principle of the

algorithm is that for each pixel at the lumen boundary, the same amount of light enters the tissue, such that further analysis can be carried out without the bias caused by the catheter position. It is designed to overall enhance the absolute intensities for each A-line rather than changing the relative trend. Therefore, it will not affect the parameters like attenuation and backscatter. This is why the proposed algorithm preserves the dark trend within regions with weak backscattering (calcified lesion, dark square inside BVS stent struts, etc) or behind tissue with high attenuation (macrophages, foam cells, etc). Because of the total reflection, the tangential signal dropout cannot be compensated.

The compensation algorithm improves the BVS struts detection for 6 out of 8 pullbacks by 0.8-6.4 percent in F-score. In general, the overall result indicates that the compensation algorithm can potentially improve the performance of the BVS struts detection. A example can be seen in Fig 2.6. From the box-and-whisker plot of the percentile values within the black cores, we can observe that the percentiles in the compensated image are lower than that in the original images. Furthermore, it is worth noting that the lower percentiles over all the black cores are more condensed distributed. This can be the main reason that the proposed algorithm improves detection, since the lower percentile is used as a threshold in the BVS strut detection [47].

Meanwhile, in the results of the other two pullbacks with lower performances, the FP ratio tends to be higher in the detected results with compensated images. A FP example can be seen in Fig 2.6 D between the catheter and the guidewire. This is because our algorithm is designed to compensate the tissue region, which may cause structures with certain black-core-like appearance inside the lumen to be enhanced and detected, thus the FP ratio was increased. The method as described by Wang was not adjusted for the compensation experiment. Further optimization might improve the perforamnce for the two case.

2.5.3 Limitations

The range of the estimated incident angles in the experiment is relatively small due to the elliptical shape of the artery wall, which is an inevitable issue of in-vivo IVOCT data. Since the angle related term is between 0 and 1, the logarithm operation can enlarge the range of the transmission term in the linear model. Another potential issue related to the angle estimation is that the angle of incidence has been estimated with 2-D IVOCT images: the best estimation that can be achieved at present. The estimation can approximate the spatial angle well because the imaging catheter has elasticity to resists over-bending, and can thus be assumed parallel to the longitudinal direction of the artery. Nevertheless, it would be interesting to measure the angle of incidence in 3-D in a future study.

There are two catheter related terms for modeling the IVOCT signal. One is the confocal function, the other is the spectral coherence term. Both terms can be different for different catheters. This can be the reason for the variation which lies in the estimated intercept for the hierarchical regression results. So

the compensation factor can be different as well. This can be solved by using statistical analysis of non-pathological images typically present in each pullback. Normalizing the signal to noise ratio (SNR) can be another solution to incorporate the differences [54].

With a long distance between the catheter and the lumen wall, the light was assumed to be attenuated mainly by the flush medium. The cofocal function can be another potential reason. Limited by the linear regression purpose, the logarithm of the confocal function has been incorporated into the model with a fitted linear function.

2.5.4 Future work

In this paper, the compensation algorithm shows its potential to be as a preprocessing step for automatic BVS stent struts detection. For further incorporating the algorithm into the standard BVS detection workflow, more validation studies are needed, thus the parameters can be further optimized with the compensated images. Meanwhile, it is interesting to see if the compensation algorithm can improve the automatic detection of metal stent struts [ref] as well. Further experiments will be carried out for the metal stent strut detection in the future.

Additionally, for the statistical analysis, a more complex model can be used by involving higher power multivariate regression for example, then the higher power approximation of the confocal function can be used.

2.6 Conclusions

Both aspects regarding to the catheter position, the distance from the catheter to the artery wall and the angle of light incident upon the artery wall, significantly affect IVOCT image intensities. The hierarchical linear regression result shows that, as either aspect increases the intensity decreases. Using the hierarchical linear regression result, the proposed mathematical solution can compensate both pathological and non-pathological images. Results show that the proposed compensation algorithm potentially improves the visualization of IVOCT images, and allows a improved performance for the BVS struts detection.

CHAPTER THREE

TISSUE CHARACTERIZATION WITH DEPTH-RESOLVED ATTENUATION COEFFICIENT AND BACKSCATTER TERM IN INTRAVASCULAR OPTICAL COHERENCE TOMOGRAPHY IMAGES

Abstract — A new and important application of intravascular optical coherence tomography (IVOCT) for atherosclerotic tissue analysis is using it to estimate attenuation and backscatter coefficients. This work aims at exploring the potential of the attenuation coefficient, a proposed backscatter term and image intensities in distinguishing different atherosclerotic tissue types with a robust implementation of depth-resolved (DR) approach. Therefore the DR model is introduced to estimate the attenuation coefficient and further extended to estimate the backscatter-related term in IVOCT images, such that values can be estimated per pixel without predefining any delineation for the estimation. In order to exclude noisy regions with weak signal, an automated algorithm is implemented to determine the cut-off border in IVOCT images. The attenuation coefficient, backscatter term and the image intensity are further analyzed in regions of interest, which has been delineated referring to their pathology counterparts. Local statistical values were reported and their distributions were further compared with 2-sample t-test to evaluate the potential for distinguishing six types of tissues. Results show that the IVOCT intensity, DR attenuation coefficient and backscatter term extracted with the reported implementation are complementary to each other on characterizing six tissue types: mixed, calcification, fibrous, lipid-rich, macrophages and necrotic core.

This chapter was published as: S. Liu, Y. Sotomi, J. Eggermont, G. Nakazawa, S. Torii, T. Ijichi, Y. Onuma, P. W. Serruys, B. P. F. Lelieveldt, J. Dijkstra, **Tissue Characterization with Depth-Resolved Attenuation Coefficient and Backscatter Term in Intravascular Optical Coherence Tomography Images**, *J. Biomed. Opt.* 22(9) 096004, 2017.

3.1 Introduction

Optical coherence tomography (OCT) is an imaging modality with a high resolution [55]. Since the light can be transmitted via an optical fiber, OCT has been introduced into the intravascular imaging by embedding an optical fiber into an imaging catheter [5]. The acquired intravascular OCT (IVOCT) images with a high resolution (10-20μm) boosted the understanding of the composition of atherosclerosis in the coronary artery, which is one of the fatal diseases that is responsible for most of the death in the world [31]. In IVOCT images, different tissue types can be recognized [8], e.g. the fibrous tissue is bright, both lipid-rich and calcified plaque appear as low intensities, while the border of the former tends to be diffused and the latter as sharper.

To achieve automated analysis of IVOCT images for diagnosis and risk assessment, much attention has been spent on the quantitative characterization of the tissue composition of the coronary vessel wall [56, 8, 57, 58, 27, 28, 59, 60, 61, 62, 30, 63]. Inspired by the literature on tissue optics in general OCT [64, 65, 66, 67, 68, 69], one of the important features that has been analyzed is the OCT-derived attenuation and backscatter coefficient. For the accurate estimation, the modeling of the transmitting light through biological tissue usually requires taking into consideration of the complex interactions [66, 67] such as multiple scatter and concentration dependency. On the other hand, estimations have been reported at an adequate accuracy for tissue quantification based on a simplified model involving a single exponential decaying term [68, 69].

Based on the simplified model, one of the commonly used approaches for the estimation of the attenuation is the least square fitting either an exponential curve to a 1D OCT signal or a linear function to the logarithm of 1D OCT signal. The curve-fitting (CF) attenuation has been widely used to quantify biological tissue such as bladder urothelial carcinoma [70], human skin [71], nasopharyngeal carcinoma cells [72], collagen content in ovarian tissue [73], breast tissue [74], and human atrial tissue [75]. Specifically for the analysis of tissue in the coronary arteries, an earlier work of Xu et al. [27], has shown that the CF approach can be used to estimate both the attenuation and backscatter coefficients, which can improve the differentiation of atherosclerotic tissue. In order to improve the reproducibility and the robustness of the CF approach, Gargesha, et al. [76] estimated the attenuation coefficient within volumes of interest (VOI). The method has been validated with different combinations of noise reduction filtering and outlier rejecting to optimize a goodness-of-fit. Furthermore, attenuation and backscatter coefficients were analyzed to characterize the neointima formation after the stent implemented from different manufacturers. [77, 78] Van Soest, et al. [28] proposed an automated optimization scheme to estimate the attenuation coefficient by expanding fitting windows within regions assumed to be homogeneous. This approach has been validated with a later study from the same group [79]. Since the automated algorithm allows for a high robustness and reproducibility, the CF-attenuation is increasingly used for region-based tissue characterization combined with

machine learning tools, such as random forest [40], Gaussian likelihood map [74] and supported vector machine [75].

Another approach for the estimation of attenuation coefficient has been recently introduced by Vermeer et al [59]. It is based on a depth-resolved (DR) model, and allows for local pixel-wise estimation with two fundamental assumptions, the light should be attenuated completely and the backscatter and attenuation are linear related to each other. Despite strict assumptions have been made, their measurements did show a good consistency in both homogeneous and layered phantom experiments. This DR attenuation has been used for the detection of the cerebral edema in OCT images [80]. Taking the confocal function and the fall-off of the system into consideration, the DR model has been reported to estimate the attenuation more accurately and potentially further improve the pixel-wise tissue characterization in combination with a noise removal approach [81]. Besides estimating the attenuation, it should be noted that the DR model has been widely used for the enhancement of OCT images [82, 83, 84, 85, 86]. Due to its recent introduction, no quantitative analysis with DR model for tissue characterization has been reported on IVOCT images.

The aim of this work is to explore the potential of DR attenuation coefficient, backscatter term and image intensities in distinguishing different atherosclerotic tissue types with a robust implementation of DR approach. In order to achieve this goal, the DR attenuation is introduced to IVOCT, the model is further extended to estimated a backscatter term, and a cut-off border is determined to remove noisy region. Six types of tissue were labeled by two pathologists referring to their histological counterparts. Combining with the image intensities, the estimated attenuation coefficient and the backscatter term are analyzed for the differentiation of these six types of tissue. To the best of our knowledge, no such study has been published so far for intravascular tissue analysis.

The structure of this paper is organized as follows. In 3.2.1, the light propagation model and the DR-attenuation are introduced, the estimation of a backscatter term is derived in 3.2.2, and the DR model is combined with CF approach to determine the cut-off depth border in 3.2.3. The experimental materials and the implementation of the experiment are described in 3.3. The results are reported in 3.4 and further discussed in 3.5, where the estimated values are extensively compared with that in the literature. The conclusion is drawn in 3.6.

3.2 Depth-resolved model analysis

We continue to use the model of light transmission as it has been introduced in the work of Vermeer, et al. [59]

$$I_b(d) \cong \beta \cdot L_0 \cdot \mu_b(d) \cdot e^{-2\int_0^d \mu_t(u)du}, \tag{3.1}$$

where $I_b(d)$ is the digitalized signal detected at depth d, β accounts for both the quantum efficiency of the detector [67] and the converting factor of the digitizer, L_0 is the source light power (Wm^{-2}), the attenuation is denoted as μ_t and the backscatter coefficient is denoted as μ_b.

3.2.1 Depth-resolved attenuation

With an assumption that the backscattered light is a fixed fraction to the attenuated light $\mu_b(d) = \alpha\mu_t(d)$ the integration from d to infinite of Eq. 3.1 will be:

$$\int_d^\infty I_b(u)du \cong -\frac{\alpha\beta L_0}{2} e^{-2\int_0^u \mu(v)dv} + C\Big|_d^\infty = -\frac{I_b(u)}{2\mu_t(u)} + C\Big|_d^\infty = \frac{I_b(d)}{2\mu_t(d)}. \tag{3.2}$$

The fraction of Eq. (3.1) and Eq. (3.2) is then the estimated attenuation:

$$\mu_t(d) \cong \frac{I_b(d)}{2\int_d^\infty I_b(u)du}. \tag{3.3}$$

The attenuation can be estimated with the OCT image intensities as:

$$\mu[i,j] \approx \frac{I[i,j]}{2\triangle\sum_{y=j+1}^{\infty} I[i,y]}, \tag{3.4}$$

where an OCT image is denoted as I with size of $M \times N$, i indicates the A-line number (pixel), j indicates the depth number (pixel) and $\triangle$ is the pixel size (mm/pixel). In order to avoid the accumulation of noise during the calculation, the image is first denoised with a median filter.

3.2.2 Backscatter term estimation

Suppose an A-line from a homogeneous region starts at depth d_1 and ends at depth d_2. Within this region, both the attenuation and the backscatter coefficients at each depth $d \in (d_1, d_2)$ are the same $\mu_t(d) = \tilde{\mu}_t$ and $\mu_b(d) = \tilde{\mu}_b$, thus Eq. 3.1 can be simplified as:

$$I_b(d) \cong L' \cdot \tilde{\mu}_b \cdot e^{-2\cdot r\cdot\tilde{\mu}_t}, \tag{3.5}$$

where $r = d - d_1$ and $r \in [0, d_2 - d_1]$. The term $L'\beta = L_0 \cdot e^{-2\int_0^{d_1}\mu_t(u)du}$ is the diminished source intensity along the path from the catheter to the defined region. Using the same notation, L' is the diminished light power that enters at depth d_1 with the same unit as L_0 (Wm^{-2}) divided by the imaging factor β.

Within the homogeneous region, $\tilde{\mu}_t$ and $\tilde{\mu}_b$ can be estimated as the slope and the offset of the linear function fitted with $\ln[I_b(d)/\beta L']$, as it has been proposed that in the work of Schmitt, et al [64]. Noting that the L' is a constant relative to d, linear fitting $\ln[I_b(d)]$ gives the same estimation of the attenuation coefficient. However, the estimation of L' is necessary for the estimation of backscatter coefficient.

With DR model, we consider d_1 and d_2 are the start and the end of a pixel, then $e^{-2 \cdot r \cdot \tilde{\mu}_t}$ approximates to 1 since r is then very small. Dividing Eq. 3.5 by a factor of $e^{-2\int_0^{d_1} \mu_t(u)du}$ and taking the logarithm we get a similar intersection to be our backscatter term as:

$$T_b(d) = \ln \frac{L_0}{\beta} \cdot \tilde{\mu}_b \cong \ln I_b(d) + 2\int_0^{d_1} \tilde{\mu}_t(u)du \tag{3.6}$$

where $\tilde{\mu}_t(u)$ is the estimated attenuation at depth u. The defined term $T_b(d)$ is linear related to the logarithm of the backscatter coefficient with a constant offset related to the initial incident energy L_0 and the imaging parameter β.

3.2.3 DR-CF cut-off algorithm

One of the main concerns regarding the pixel-wise DR algorithm is the assumption that the integral of intensity should be taken to infinity. However, in practice infinity is substitute with a large value, the maximum depth D of the signal in case of OCT images. This causes little effect on the estimated attenuation of the superficial tissue region, where the signal is much stronger than the noise. However, as it approaches to the end of an A-line, the estimated attenuation coefficient with the noise-dominant signal will be exaggerated thus is unreliable.

In order to avoid this, we applied the DR-CF algorithm to determine a cut-off depth. Noting that:

$$\int_d^{\infty} I_b(u)du = \frac{\alpha\beta L_0}{2} e^{-2\int_0^{d_1} \mu(u)du} e^{-2\int_{d_1}^{d} \tilde{\mu}du} = \frac{\alpha L'}{2} e^{-2r\tilde{\mu}}, \tag{3.7}$$

thus taking natural logarithm to the both sides, Eq. 3.7 becomes:

$$\ln\Big(\int_d^{\infty} I_b(u)du\Big) \cong -2r\tilde{\mu} + \ln\frac{\alpha L'}{2}. \tag{3.8}$$

The second term is a constant, the logarithm of the integral intensities follows a linear function with respect to the depth within this region, and the attenuation can be calculated from the slope. With the DR-CF algorithm, the left term is always decreasing, thus it guarantees that the estimated values are positive and the high noise tolerance of the CF-approach is maintained. Since the deeper signals are influenced strongly by noise, it is difficult to perceive the local variations, but the general decreasing trend can still be estimated with the DR-CF algorithm.

The cut-off algorithm is described in Algorithm 1. The linear fitting is implemented in Matlab (R2016a, The MathWorks, Inc., Natick, Massachusetts, USA) with the Least Square approximation. In Algorithm 1 Step 2, the size of the sliding window size is chosen to be 21 pixels for each A-line. After fitting, an error image I_{err} is calculated, and then a threshold of the squared error 5×10^5 was experimentally chosen to create a binary image I_{bw} in Step 3. In order to

determine a continuous border with the regional maximum got in Step 3, a morphological closing of I_{bw} is used in Step 4, where the octagon operator is used with a radius of 6 pixels.

Algorithm 1: Determine the DR-CF cut off border

1: Calculate the $cum_I_b = \int_d^D I_b(u)du$;
2: From the backside of each A-line, estimate the attenuation with linear fitting according to Eq. 3.8 with a sliding window calculate the image of
3: the fitting error I_{err} (the total norm of fitting residuals) is found.
4: Threshold the fitting error and extract a binary image I_{bw} marking the regional maximum.
5: Morphologically close I_{bw} with a octagon of radius R, and the backborder defined binary image is the defined cut-off depth border.

3.3 Experiment and Implementation

In order to analyze the potential of the IVOCT-estimated optical values for distinguishing the coronary artery tissue, six types of tissue were delineated according to their pathological counterparts harvested from two cadaver hearts, resulting in 135 of IVOCT images for the analysis. The data and the implementation for the analysis are described in more detail as follows.

3.3.1 Data description

Coronary segments were dissected from the cadaver hearts and imaged ex-vivo by OFDI. The samples were pinned on a rubber sheet and immersed in a water bath with 0.9% saline solution. A 0.014-inch guidewire was introduced into the vessel followed by an OFDI catheter (LUNAWAVE, Terumo). Sequential images were acquired at a pullback rate of 20 mm/s (158 frames/s, 512 A-lines per frame). The source light has a center wavelength of 1300 nm and a bandwidth of 124 nm. The depth resolution for each A-line used in this work is 5.4 $\mu m\ per\ pixel$, which has been calculated with the refractive index stored in the raw data as 1.447.

3.3.1.1 Tissue Preparation and Plaque Assessment

After the intracoronary imaging, samples were X-rayed and then decalcified using ethylene diamine tetraacetic acid as required. Coronary segments were sectioned at 3 to 4mm intervals and embedded in paraffin to obtain 4 to 6 μm thick sections followed by hematoxylin $\&$ eosin (H$\&$E) and Movat pentachrome stain.

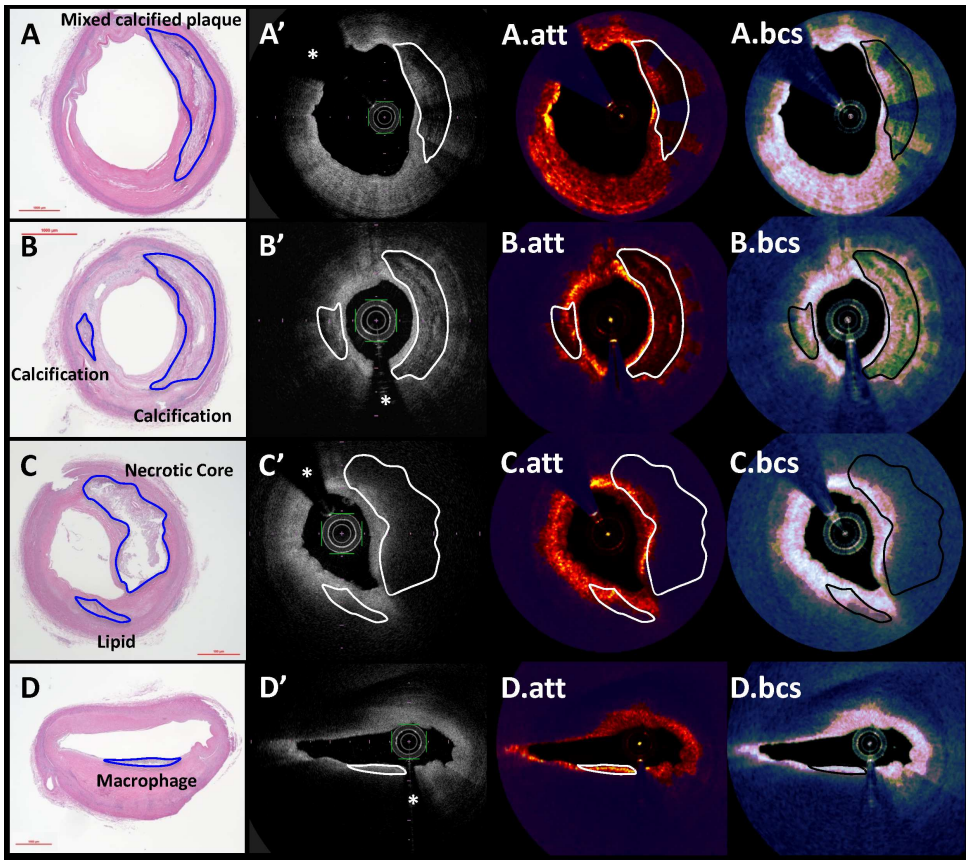

Figure 3.1: The histological cross-sections (**A**-**D**) and the corresponding IVOCT cross-sections (**A**'-**D**'). Star (*) marks the guide wire. The attenuation coefficients and the backscatter term are labeled as (**A**-**D**).att and (**A**-**D**).bcs, respectively. Noisy region behind the determined cut-off border is marked with dark blue overlay in attenuation and backscatter cross section. Plaques of interest are labeled in pathological cross-sections, which have been aligned with other related IVOCT images.

3.3.1.2 Matching and delineating IVOCT images

In each pathological cross-section, two pathologists (CN and ST) identified the following tissue categories in histology: lipid, calcification, mixed calcified plaque, necrotic core, and macrophage. The remaining tissue was identified as fibrous plaque. The identified tissues in histology were independently delineated by the pathologists such that each regions of interest (ROIs) only included one type of tissue (Fig. 3.1 A-D).

The histological cross-section and the corresponding IVOCT cross-section

were matched using the lumen shape and tissue appearance in both images by two cardiologists [YS and YO]. IVOCT cross-sections with insufficient image quality and significant artifacts such as tangential artifact were not used for the analysis. Based on the contours delineated by the pathologists in histology, the two cardiologists delineated the same tissue in matched IVOCT images in QCU-CMS (LKEB, Leiden University Medical Center, Leiden, The Netherlands) (Fig. 3.1 A′-D′). When the border of the tissue could clearly be detected on IVOCT, the delineation followed the borderlines. When the border could not be clearly perceived, the contours in histological images were superimposed on the IVOCT images in order to yield a high reproducibility. If there were more than two layers of different ROIs in one cross-section, only the most adluminal ROI was employed for the analysis considering the light property.

The two pathologists [GN and ST] were blinded to the IVOCT delineation and IVOCT light property analysis. At the stage of IVOCT delineation, to enable accurate co-localization of the histology with IVOCT images, two cardiologists [YS and YO] were unblinded to the histological identification. However, these cardiologists were blind to the following IVOCT light property analysis. The IVOCT light property analysis was performed independently from the either histological identification or IVOCT delineation process.

3.3.2 Implementation

The experimental flow of analyzing the IVOCT values was designed as it is shown in the Fig. 3.2.

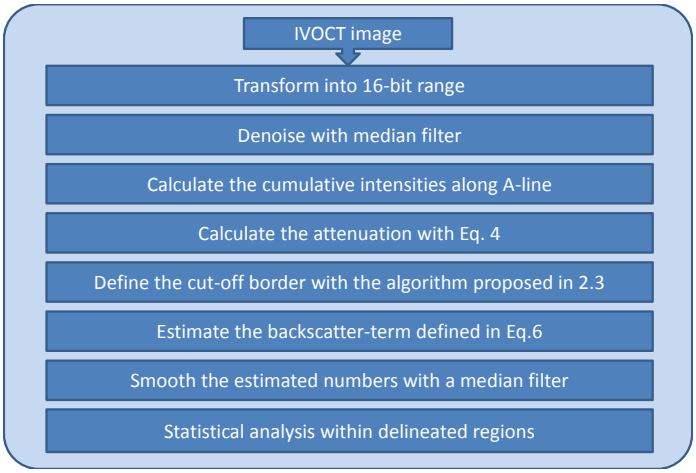

Figure 3.2: The work flow for the experiment.

3.3.2.1 Data transformation

In the Terumo Lunawave imaging system, images are saved at 8-bit depth to allow for a high system sensitivity, resulting into a lower dynamic range than those saved at 12-14 bit depth [87]. The algorithm has been proposed based on a transition model that is linearly related to the detected light signal. Once the image is compressed nonlinearly, the estimated values can be in different ranges. As optical properties, it is expected that the estimated attenuation coefficient and backscatter term are in the same range for the same type of tissue rather than depending on the imaging systems. In order to overcome this issue, we used a matching look-up table to match 8-bit images generated with Lunawave from Terumo (Tokyo, Japan) to 16-bit range of images generated with Illumien Optis from St. Jude Medical (St. Paul, MN, USA) [88].

3.3.2.2 Denoising

A median filter with small window size is applied to the pixel-wise DR estimated values to remove noise. Pixel-wise DR estimation allows statistical analysis within local regions. Although it might blur the edges between different types of tissue, the median filter will hardly affect the statistical distribution within the local region.

The median filter window size was chosen as $[3, 11]$ for calculation of cum_I_b and the same window size was applied for noise removal. With a pixel size of 5.4 μm, this length accordingly covers a range about 60 μm. The window size eleven is chosen to be the maximum odd number that covers approximately the thickness of small identifiable structures e.g. a thin cap defined in the literature [89] ($< 65\ \mu m$).

3.3.3 Statistical analysis

The data was processed and analyzed with MATLAB. For each delineated region, the distribution of intensities, attenuation and the backscatter term is analyzed. The mean, standard deviation (std), median, maximum (max), $95th$ percentile ($95th$ Per.), minimum (min), skewness and kurtosis values were calculated within each delineated region. Values between different tissue types were compared with the two-sample $t - test$. Both 3D scatter plots of the intensity, attenuation coefficient and backscatter term and their principle component analysis (PCA) projected 2D scatter plot are generated.

3.4 Results

In MATLAB, the current code has been implemented with 3-D matrices calculation. Median filtering with a window size of 11 pixels on a PC with a 2.83-GHz dual-core processor currently takes 7 s for every 100 IVOCT polar images of 512 A-lines with 900 depth points. The total time of calculating the attenuation coefficient and the backscatter term with cut-off border

Table 3.1: Statistical Values

		Intensity (no unit) average ± std	Attenuation (mm^{-1}) average ± std	Backscatter (no unit) average ± std
Mixed	mean	156.84±2.08	1.68±0.14	5.81±0.09
	median	157.14±2.24	1.44±0.17	5.85±0.13
	std	26.00±0.59	1.14±0.07	0.71±0.03
	max	236.64±3.04	7.34±1.01	7.56±0.19
	95th Per.	198.93±2.09	3.89±0.25	6.91±0.07
	min	43.27±13.31	0.11±0.06	3.43±0.61
	skewness	-0.15±0.07	1.11±0.23	-0.17±0.26
	kurtosis	3.01±0.08	4.38±0.94	2.51±0.40
Cal	mean	142.49±15.05	0.87±0.24	5.24±0.42
	median	143.06±15.11	0.68±0.16	5.21±0.41
	std	26.43±2.19	0.63±0.21	0.65±0.07
	max	232.68±16.39	5.35±1.10	7.37±0.29
	95th Per.	185.07±17.10	2.17±0.73	6.37±0.49
	min	31.21±20.63	0.13±0.03	3.54±0.36
	skewness	-0.11±0.12	2.22±0.49	0.24±0.21
	kurtosis	3.03±0.16	10.72±4.87	2.78±0.29
Fib	mean	172.17±10.39	1.75±0.48	6.22±0.32
	median	173.93±10.42	1.67±0.47	6.24±0.34
	std	21.31±1.33	0.61±0.17	0.36±0.04
	max	228.53±8.80	4.55±1.20	7.19±0.24
	95th Per.	204.07±9.49	2.86±0.75	6.78±0.30
	min	73.77±19.97	0.50±0.20	5.06±0.35
	skewness	-0.47±0.10	0.79±0.36	-0.24±0.35
	kurtosis	3.29±0.26	4.05±1.35	3.01±0.60
Lip	mean	160.40±3.27	2.60±0.13	6.23±0.11
	median	161.60±3.78	2.45±0.12	6.27±0.10
	std	24.97±1.69	1.16±0.08	0.58±0.08
	max	221.80±3.27	6.47±0.58	7.40±0.11
	95th Per.	199.80±1.92	4.73±0.28	7.06±0.08
	min	64.00±15.43	0.64±0.10	4.60±0.28
	skewness	-0.27±0.07	0.56±0.10	-0.35±0.15
	kurtosis	2.82±0.15	2.71±0.36	2.41±0.43
Mac	mean	173.02±4.76	3.41±0.38	6.50±0.13
	median	173.97±4.89	3.22±0.45	6.59±0.13
	std	24.63±3.91	1.49±0.36	0.57±0.15
	max	232.05±6.70	7.78±1.11	7.57±0.18
	95th Per.	211.47±6.09	6.05±0.85	7.27±0.16
	min	76.58±25.30	0.62±0.35	4.67±0.87
	skewness	-0.28±0.14	0.38±0.31	-0.56±0.37
	kurtosis	2.92±0.39	2.53±0.42	2.91±1.30
Nec	mean	159.98±4.79	1.89±0.54	6.10±0.17
	median	160.06±4.83	1.72±0.44	6.11±0.19
	std	22.43±2.06	0.84±0.37	0.51±0.10
	max	228.28±10.94	5.54±1.86	7.44±0.25
	95th Per.	196.51±7.55	3.51±1.26	6.93±0.26
	min	68.25±11.44	0.42±0.12	4.54±0.31
	skewness	-0.10±0.20	0.96±0.31	-0.07±0.29
	kurtosis	3.04±0.21	4.09±1.22	2.64±0.35

determination is 2.7 minutes. Meanwhile as implemented in QCU-CMS, median filtering with a window size of 11 pixel points currently takes 24 s on a PC with a 2.66-GHz quad-core processor with hyperthreading for every 553 IVOCT polar images of 512 A-lines with 1024 depth points. The total time of calculating the attenuation coefficient and the backscatter term without cut-off border determination is 23 s and 22 s, respectively. Currently, the processing time is reasonable fast and it is not a major concern. For the future clinical orientated on-the-fly application, the code and the implementation can be further optimized.

The statistical results are presented in Table 3.1. The average and the standard deviation values were reported for all the regions from each tissue type, and the number of analyzed regions is given under the name of the tissue. The reported IVOCT intensity is the Terumo image intensity. Using the known calibration factor of the IVOCT images, the unit of the estimated attenuation coefficient is mm^{-1}.

The comparison results of median values, mean values, standard deviation, maximum values, $95th$ percentile, minimum values, skewness and kurtosis are shown in Fig. 3.3-3.10, respectively. The whisker box plot is given with 6 tissue groups. When the result of 2-sample t-test indicates the numbers are not significantly different, the two groups are marked with an **X**-mark.

In the graph in the second row of each figure, the comparison of six tissues is shown as a relationship grid graph. For each paired tissue types, the square is colored as green if they are significantly different, red otherwise. Three graphs are combined into one graph shown on the right hand side of the bottom row in a way that as the square is colored green as long as there is a green in this square in the other three graphs, red otherwise. The 3-D scatter plots can been seen in Fig. 3.11 and 3.12. The PCA projected 2-D scatter plots are shown on the right hand side of the top row for each figure.

In general, we found that the values within the delineated regions had a strong correlation with tissue types at the 5% significance level by comparing the median, mean, std, 95th percentile and minimum values of IVOCT intensity, estimated attenuation coefficient and the backscatter term. This can be observed from the combined comparative graphs in Fig. 3.3 and 3.4 where the red color is not presented. Also from the PCA projected 2-D plot, the other values did not show clusters as distinguishable as they are in the mean and median values. The PCA projected 2-D plot of std values shows clear clusters of fibrous and the calcified plaques. Furthermore, it is worth noting that clear cluster patterns of the calcification, fibrous and macrophages can be observed from the 2-D plot of the skewness values.

Most of the time, the three IVOCT numbers are complementary to each other for the differentiation of the six tissue types. For example, the median values (Fig. 3.3) of the attenuation are not significantly different between tissue types of mixed calcified (Mixed) and the fibrous but the median values of intensities and backscatter values are significant different, and the vice versa when comparing necrotic core to lipid-rich regions. This complementary can be observed in all the all the comparing figures (Fig. 3.3-3.9), but most notable in median, mean, std

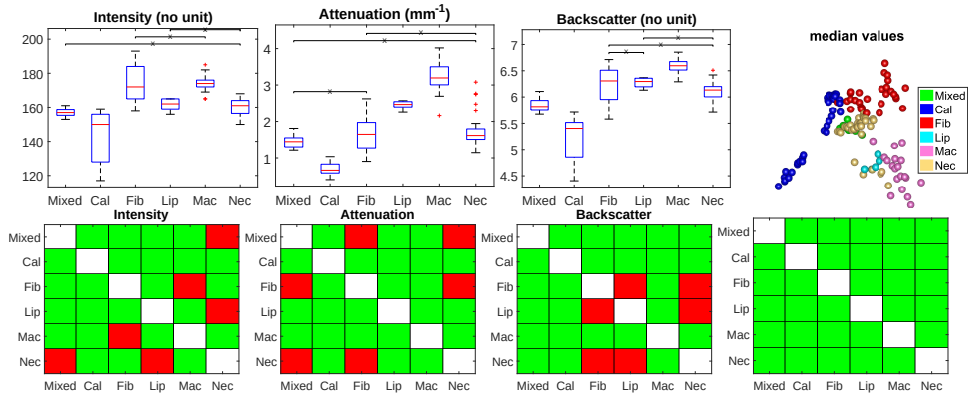

Figure 3.3: Comparison of the median values of intensities (no unit), attenuation coefficient (mm^{-1}) and backscatter term (no unit) within each delineated region. The median values of the six types of tissue were compared to each other with two-sample t-test with significance $\alpha = 0.05$. The whisker box plots can be seen on the top row, where paired tissue types that are not significantly different were connected with an 'X' mark. This statistical results are furthermore shown as a binary matrix, where the square is filled with green and gets a value 'TRUE' if the relative tissue pair is statistically different, red and 'FALSE' otherwise. Since it does not make sense to compare each tissue type to itself, the diagonal is filled with white. On the right hand side at the bottom row, the three matrices are integrated with an 'OR' operation. On the right hand side of the top row, the PCA projected 2-D scatter plot is displayed.

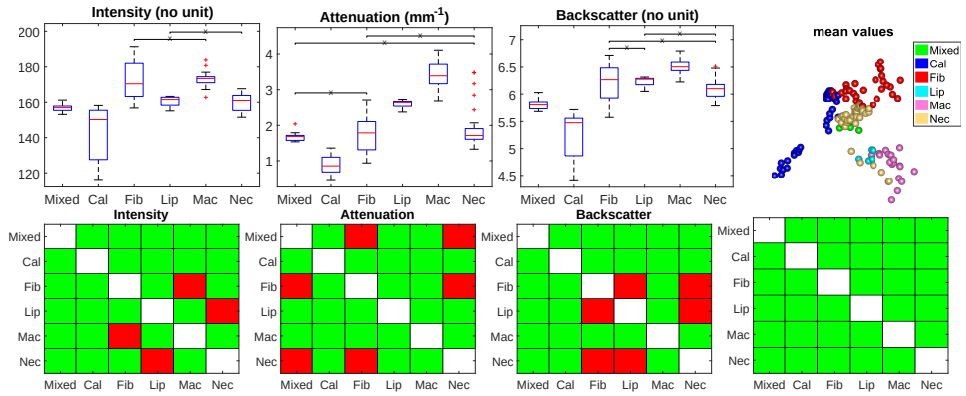

Figure 3.4: Comparison of the mean values of intensities (no unit), attenuation coefficient (mm^{-1}) and backscatter term (no unit) within each delineated region. The layout information of the figure is the same as it is in Fig. 3.3.

and maximum values (Fig. 3.3-3.6)

In order to give an overview of the estimated values for the entire pullback, a 'carpet view' image is generated. For a given stack of polar images, the maximum value for each A-line is determined in the first 1 mm depth below the lumen surface. In order to maintain the relative size of the plaques, the images are displayed with the lumen contour circumference normalized by the largest circumference over the entire pullback. The maximum projected attenuation and backscatter carpet views are shown in Fig. 3.13 and 3.14, where the largest circumference is 7.71 mm. In order to show the values in a proper window level, key points of generating the color map are appointed both experimentally and referring to the work by Gnanadesigan et al [79]. As it can be seen in Fig. 3.15, multiple pathological images shown macrophage infiltration. The corresponding locations are marked as 'M' in blue, and they are much brighter than other tissue in both carpet-views. This is consistent with the our quantification analysis showing that both attenuation coefficient and the backscatter term are high. In order to show the estimated values for all six types of tissue, the attenuation coefficient and the backscatter term of IVOCT images in Fig. 3.1 are generated as well.

3.5 Discussion

The work aims at exploring the potential of DR attenuation coefficient, backscatter term and image intensity in distinguishing different atherosclerotic tissue types with a robust implementation of DR approach. We describe the implementation of DR approach for the estimation of the attenuation coefficient in IVOCT images, and extend it to estimate a backscatter term. To exclude the noisy regions, we describe an algorithm to automatic determine the cut-off

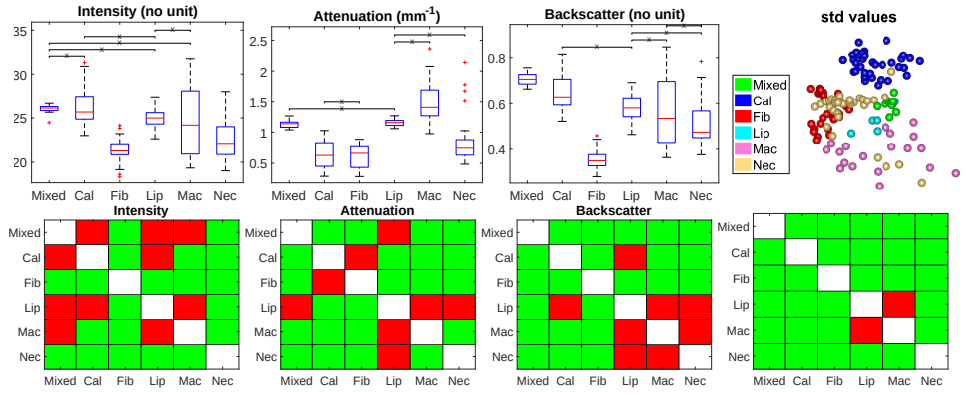

Figure 3.5: Comparison of the standard deviations of intensities (no unit), attenuation coefficient (mm^{-1}) and backscatter term (no unit) within each delineated region. The layout information of the figure is the same as it is in Fig. 3.3.

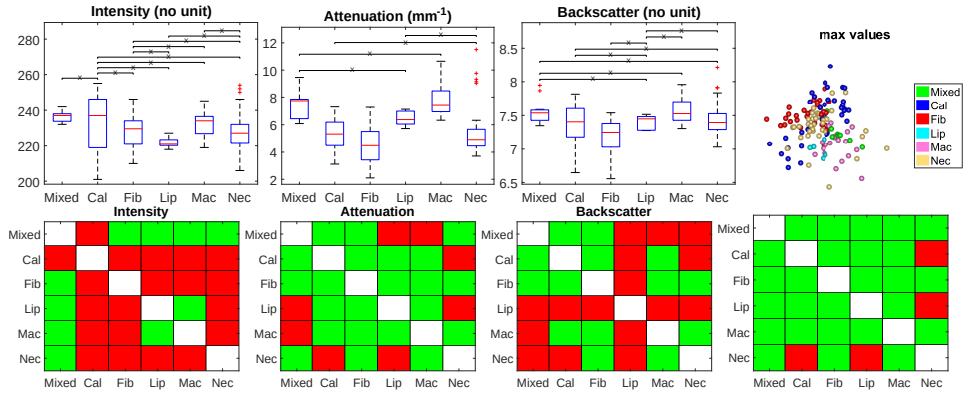

Figure 3.6: Comparison of the maximum values of intensities (no unit), attenuation coefficient (mm^{-1}) and backscatter term (no unit) within each delineated region. The layout information of the figure is the same as it is in Fig. 3.3.

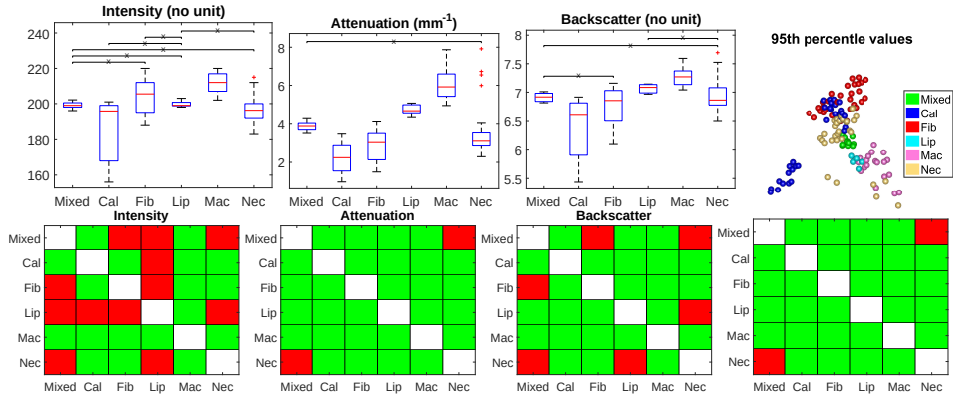

Figure 3.7: Comparison of the $95th$ percentiles of intensities (no unit), attenuation coefficient (mm^{-1}) and backscatter term (no unit) within each delineated region. The layout information of the figure is the same as it is in Fig. 3.3.

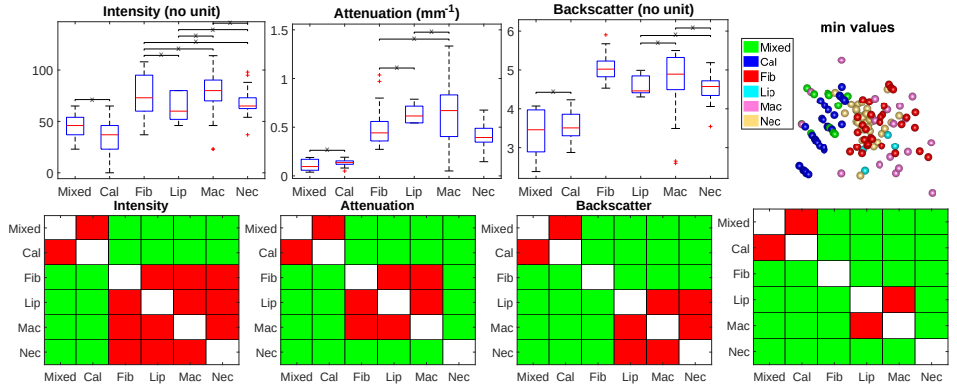

Figure 3.8: Comparison of the minimum values of intensities (no unit), attenuation coefficient (mm^{-1}) and backscatter term (no unit) within each delineated region. The layout information of the figure is the same as it is in Fig. 3.3.

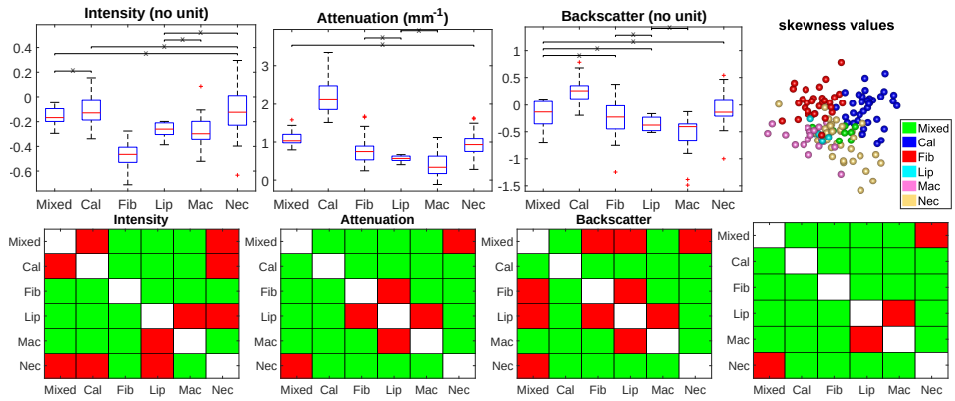

Figure 3.9: Comparison of the skewness values of intensities (no unit), attenuation coefficient (mm^{-1}) and backscatter term (no unit) within each delineated region. The layout information of the figure is the same as it is in Fig. 3.3.

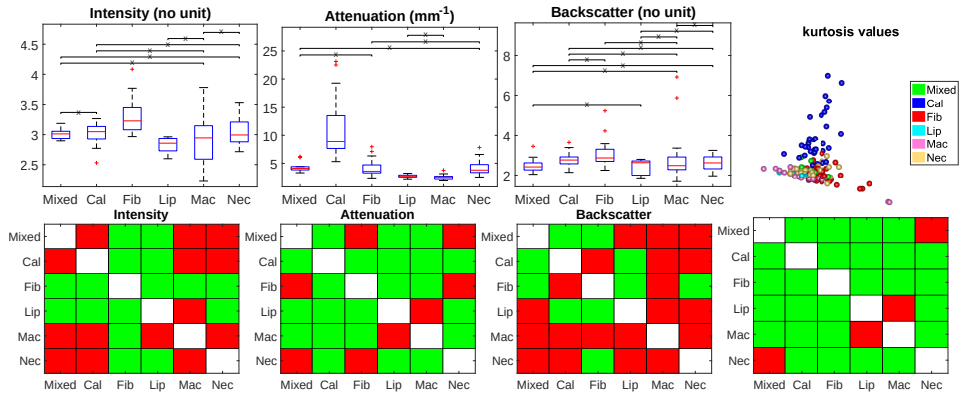

Figure 3.10: Comparison of the kurtosis values of intensities (no unit), attenuation coefficient (mm^{-1}) and backscatter term (no unit) within each delineated region. The layout information of the figure is the same as it is in Fig. 3.3.

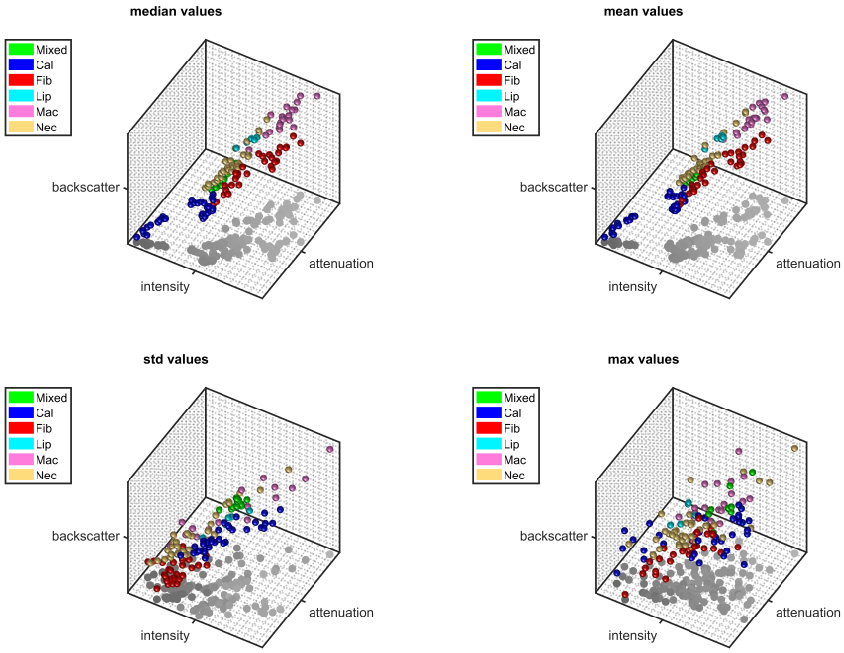

Figure 3.11: 3-D scatter plots of median, mean, std and maximum values, which were normalized into $[0, 1]$

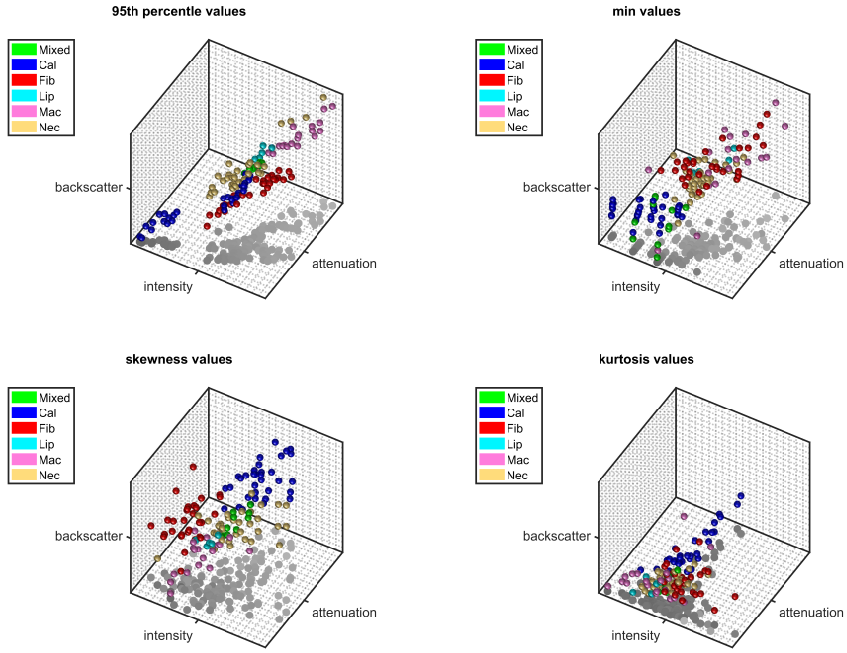

Figure 3.12: 3-D scatter plots of 95th percentile, minimum, skewness and kurtosis values, which were normalized into $[0, 1]$

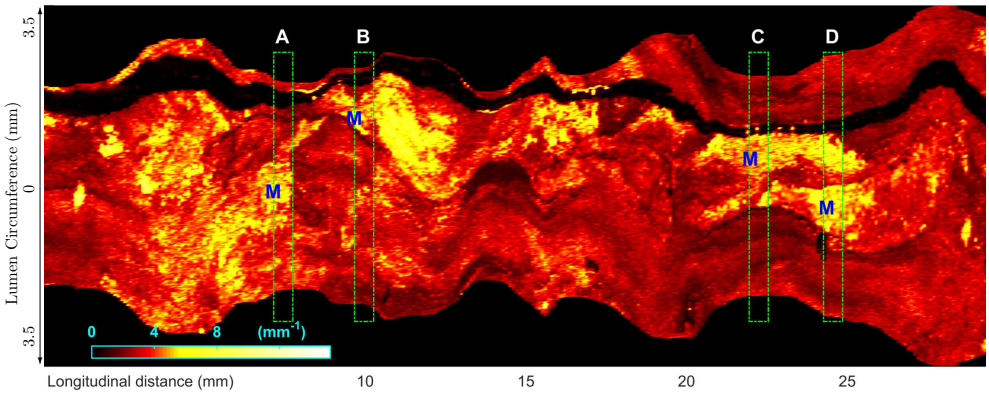

Figure 3.13: The carpet view of the maximum attenuation coefficient within 1 mm depth. Four locations are marked with green squares and labeled as A, B, C and D. 'M' in blue marks the corresponding locations shown in the pathological images in Fig. 3.15 where macrophages are labeled. The cross-sections of estimated attenuation coefficients can be seen in Fig. 3.15, labeled as '*.att'.

border. Combining the estimated attenuation coefficient and the backscatter term with the image intensity, we report that it is possible to differentiate six types of clinically important tissue [8, 5, 56] including the mixed calcified plaque, calcified plaque, fibrous plaque, lipid-rich plaque, plaque with macrophage and plaque with necrotic core.

3.5.1 Attenuation coefficient

The light transmission model of OCT signals was used as it has been introduced in the work of Vermeer, et al. The attenuating term is modeled as $e^{-2\mu_t r}$, while it has been modeled as $e^{-m_t r}$ in some CF approaches in the work of, e.g. van Soest et al. The direct result of using this factor 2 in the exponential term is that the estimated attenuation coefficients are expected to be smaller than that have been previously reported in some of the studies. This difference only affects the absolute values rather than the comparative trend, therefore we focus more on the comparative trend of the estimated values when comparing to the literature.

The attenuation coefficients of neointima has been reported as 0.35 ± 1.38 mm^{-1} without lipid-laden and 2.00 ± 1.16 mm^{-1} with lipid-laden in the work of Yonetsu et al [77]. For the in-stent restenosis lesions of drug-eluting stents (DES) and bare-metal stents (BMS), the attenuation coefficients have been estimated as 1.69 ± 0.84 mm^{-1} and 1.74 ± 0.81 mm^{-1}, respectively in the study of Nagoshi, et al [78]. These values have been estimated with the LightLab software. Despite the estimation algorithm is unknown, these reported values are within the similar range of estimated attenuation coefficients of the fibrous

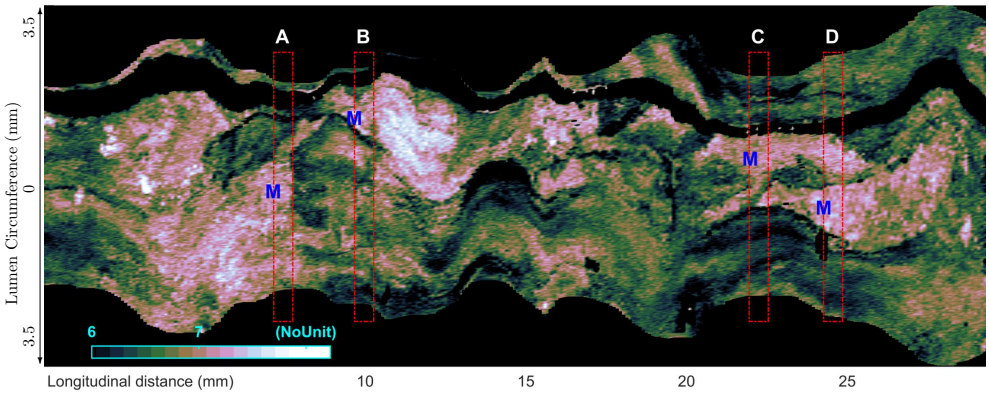

Figure 3.14: The carpet view of the maximum backscatter term within 1 mm depth. Four locations are marked with red squares and labeled as A, B, C and D. 'M' in blue marks the corresponding locations shown in the pathological images in Fig. 3.15 where macrophages are labeled. The cross-sections of estimated backscatter term can be seen in Fig. 3.15, labeled as '*.bcs'.

tissue (mean: 1.75±0.48 mm^{-1}, median: 1.67±0.47 mm^{-1}). Taking the factor 2 into consideration, the estimated attenuation coefficient of the fibrous tissue (mean: 3.52±1.92 mm^{-1}, median: 3.36±1.88 mm^{-1}) is comparable to that reported as 2-5 mm^{-1} in the work of van Soest et al [28] and relatively lower than that reported as 6.4±1.2 mm^{-1} in the work of Xu et al [27].

For regions with macrophages infiltration, the range reported by van Soest et al. is 12 mm^{-1}, and even can be as high as 15 mm^{-1} in a given example, which tends to be much higher than the other tissue types. Although we found attenuation coefficients of regions with calcification and macrophages much lower than what has been reported in these two studies, the comparative relationship of the values is the same, where the value of macrophages (mean: 3.41±0.38 mm^{-1}, median: 3.22±0.45 mm^{-1}) is the highest, and the value of the calcification (mean: 0.87±0.24 mm^{-1}, median: 0.68±0.16 mm^{-1}) is lower than that of fibrous tissue (mean: 1.75±0.48,median: 1.67±0.47).

For the lipid rich regions we found a mean attenuation value of 2.60±0.13 mm^{-1} and median 2.45±0.12 mm^{-1}. This is lower than what has been reported in the literature; 13.7±4.5 [27] and > 8.5 [79]), but higher than fibrotic tissue which fits in the reported trends. A reason for this is that the cardiologists did draw the similar shape in IVOCT as was seen in the pathological slides (Fig. 3.1). Due to the high attenuation, the back border of the lipidic region is not seen in IVOCT and the deeper regions are dominated by noise. To avoid the inclusion of noise in the statistical parameters, we introduced the cut-off algorithm to remove the noisy regions. In order to compare relatively high values within the superficial limited regions of the lipid plaque, a higher percentile (95th) was considered for comparison as well. It should be noted that

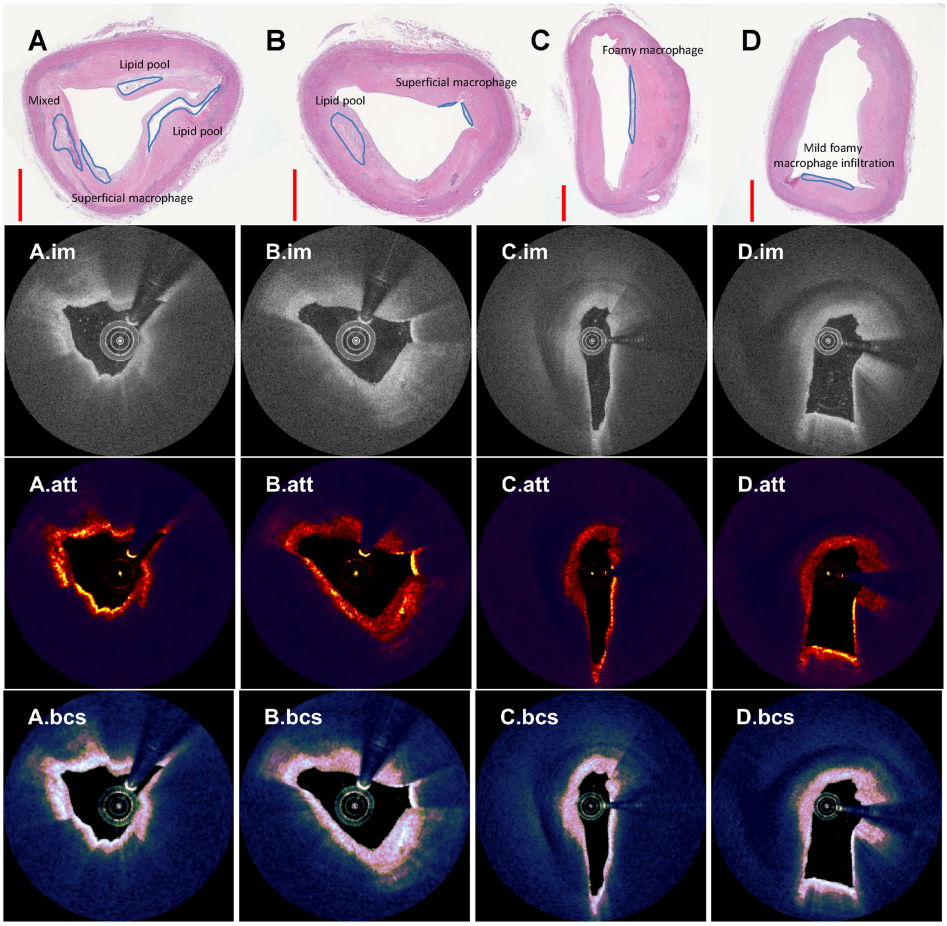

Figure 3.15: The pathological cross-sections, the IVOCT images (*.im), the attenuation coefficients (*.att) and the backscatter term (*.bcs) at four locations A, B, C and D given in Fig. 3.13 and 3.14. Deeper region behind the determined cut-off border is marked with dark blue overlay in attenuation and backscatter cross section. Plaques of interest are labeled in pathological cross-sections, which have been aligned with other IVOCT related images.

the 95th percentile of the estimated values within the lipid rich region can be as high as 4.73 ± 0.28 mm^{-1} and that of macrophages can be 6.05 ± 0.85 mm^{-1}, which is much higher than that for other tissue types. The comparative relationship in the mean, median and 95th percentile values of the estimated attenuation coefficient is Cal<Fib<Lip<Mac.

With respect to the necrotic tissue cores, since the plaques with macrophages and lipid were labeled separately, the necrotic cores chosen in this work are expected to be with less macrophages infiltrations. This is shown in the estimated attenuation that the necrotic core (mean 1.89 ± 0.54, median 1.72 ± 0.44) is lower than lipid (mean 2.60 ± 0.13, median 2.45 ± 0.12) and macrophages (mean 3.41 ± 0.38, median 3.22 ± 0.45), and is just above the fibrotic tissue (mean 1.75 ± 0.48, median 1.67 ± 0.47). In van Soest's work [28], the necrotic core ($\geq$ 10 mm^{-1}) has been 'read' as lipid plaque when comparing to the study of Xu et al. We carefully inspected the regions in the IVOCT images which were annotated as necrotic core by pathologists, but could not identify bright regions or spots like was shown in the van Soest's work thus resulting in a lower mean and median attenuation and backscatter. Therefore, the discrepancy comparing to van Soest's work is caused by a difference in the data.

It should be noted that two clusters of values are observed in the median and mean values of the calcified plaque in the PCA projected 2-D plot (Fig. 3.3 and 3.4). This can be caused by the large variation in the median/mean values of the intensities (mean: 142.49 ± 15.05, median: 143.06 ± 15.11) and the backscatter term (mean: 5.24 ± 0.42, median: 5.21 ± 0.41). However, it is worth noting that the distribution of the median/mean values in the attenuation is relatively condensed (mean: 0.87 ± 0.24, median: 0.68 ± 0.16), and the range of values are significantly different from any other tissue type.

3.5.2 Backscatter term

As it has been stated, the DR attenuation was estimated with the precondition that the attenuation and the backscatter coefficients are linear related to each other. Rather than estimating the backscatter coefficient, the proposed calculation of the backscatter term in our work is based on the principle that the 'offset' of the linear fitting is the backscatter-related term, the exponential of which has been shown to be linear related to the actual backscatter coefficient in the work of Schmitt, et al. [64]. Applying this principle, the DR model was extended to estimate this term pixel wise. Our analysis of the optical model shows that this term is related to both the backscatter coefficient and the initial power of the incident light. Results show that this term provides different comparative graph and additional information for tissue differentiation. For example, fibrotic tissue was not significantly different from macrophages for the mean intensities, but they are statistical different in mean values of the estimated backscatter term (Fig. 3.4).

To the best of our knowledge, only three studies have reported the backscatter coefficient in the literature of tissue analysis within vessel walls [77, 78, 27]. The estimated values with the LightLab software have been

reported for neointima as 6.19±0.81 without lipid-laden and 6.56±0.60 with lipid-laden [77], and have been reported as 6.92±0.42 and 7.14±0.41 for the in-stent restenosis lesions of drug-eluting stents (DES) and bare-metal stents (BMS), respectively [78]. This range is comparable to that of our estimated values of fibrous region (mean: 6.22±0.32 mm^{-1}, median: 6.24±0.34 mm^{-1}).

The backscatter coefficient has been measured by Xu et al [27] as 18.6±6.4 mm^{-1} for fibrous tissue, 28.1±8.9 mm^{-1} for lipid rich tissue and 4.9±1.5 mm^{-1} for the calcified plaque. Although the absolute values are not comparable to our values due to different experimental settings and a fundamentally different approach for the estimation as mentioned before, we still observe similar patterns. The fibrous plaque has been reported to have ′high backscatter and low attenuation′, while our results do show that backscatter for fibrotic tissue is relative high with relatively low attenuation. When comparing fibrous regions to macrophage regions, it is worth noting that the mean, median and the 95th percentile values for the former are lower, suggesting a more compact distribution. This may relate to the speckle pattern caused by the inhomogeneous distribution of the foam cells. The estimated value in calcified regions (mean: 5.24±0.42, median: 5.21±0.41) is significantly lower than that in fibrous regions (mean: 6.22±0.32, median: 6.24±0.34). The Lipid is not significantly different from fibrous in the mean and median of the estimated backscatter term, but the prior is higher that the latter in the 95th percentile values (95th percentile: 7.06±0.08 Vs 6.78±0.30).

3.5.3 IVOCT intensity

Most studies in literature focused on the comparisons of only the attenuation coefficient [70, 68, 69, 71, 72, 28, 40, 76], or the IVOCT intensities [58, 57], while a few studies combined the attenuation and the backscatter coefficients [78, 77, 27]. The 2-sample t-test results suggest that the IVOCT image intensity does additionally contribute to the differentiation of the tissue types. For example for the fibrotic versus necrotic tissue, the mean values of neither the attenuation nor the backscatter term are significantly different (Fig. 3.7), while the mean values of the intensities are significantly different.

On the other hand, it has been found in our previous work that the IVOCT intensities can be affected by the eccentric position of the catheter when light travels a long distance through the flush medium or enters the arterial wall with a large incident angle [90]. In this analysis, this bias on intensities has been minimized by using only the lesions with front edges that are almost perpendicular to the incident light from the catheter. However, it is usually difficult to avoid this bias in clinical data. It has been shown that the intensities can be normalized with the summation of the total amount of incident light, yet additional statistical analysis on healthy tissues is required. From the principle equations for estimating attenuation coefficient and backscatter term, one may note that these two optical parameters are normalized with the summation of the total amount of intensities, thus are expected to be less affected by this particular bias. Therefore, practical analysis with *in-vivo* data are suggested to

be focused more on these two estimated optical properties.

3.5.4 Limitations

The catheter related terms were not considered in this work. As far as we know, even in the most recently published studies in the literature of the experimental optical measurements, the catheter related term was reported to be calibrated either with OCT measurements in a weakly scattering media [67], or a particular phantom [91]. Since we only had access to the image data and not the used catheter, the catheter specific calibration could not be done. However, as it has been discussed in the work of Vermeer, et al. the maximum bias caused by the confocal function to the estimated DR attenuation is $\pm 1/(4z_R)$ at depth $z = z_0 \pm 2z_R$ where z_0 is the focus position and the z_R is the Rayleigh length. Calculating with $z_R = 2$mm used in the work of Ughi et al. [40], the maximum bias is expected to be around $\pm 0.125\text{mm}^{-1}$, which is relatively small comparing to the scale for the estimated DR attenuation coefficient with IVOCT images.

Another potential issue could be that different tissue types have a different refractive index. This is not taken into account during the reconstruction process. This could lead to a difference in image resolution in different tissue types, while a fixed resolution is used. Ideally, different refractive indices should be applied for different types of tissue during the reconstruction. However, it requires prior knowledge of tissue compositions, which is almost impossible in practice.

When the resolution term is modeled as a function related to depth and tissue type, the impact on the accuracy of estimated optical coefficients can vary. Equation 3.4 will become:

$$\mu[i,j] \approx \frac{I[i,j]}{2\sum_{y=j+1}^{\infty} \Delta[i,y|X] \cdot I[i,y]}, \tag{3.9}$$

X is a certain tissue type, $\Delta[i,y|X]$ is the pixel size at location $[i,y]$. The pixel size is inversely proportional to the refractive index. As it has been reported in the literature [27], the refractive indices of fibrous tissue, lipid pool and calcification tend to be around 1.35, 1.43 and 1.50 with a center wavelength of 1320 nm, thus the pixel size in the previous two types of tissue should be larger than 5.4 μm, while calcified lesions yield a smaller pixel size. Then it is expected that estimated values can be maximum overestimated by a factor of 1.447/1.35 in normal/fibrotic tissue or underestimated by a factor of 1.447/1.50 when a large calcified lesion is present. Taking macrophages in this study as an example, the median value of estimated attenuation is 3.22 μm. When the pixel size is considered to be the only factor that affects the estimation, the real value is expected to be within an interval of [3.00, 3.34]. Given the large difference in attenuation to the other types of tissue, the impact caused by the imaging resolution in detecting the presence of macrophages is expected to be small.

For the sake of real-time computing, a median filter is applied rather than a more complex speckle noise removal filter such as the iwhTV denoising published recently [81] or the Entropy filter used by Jmenez et al [92]. A fixed window size

has been selected as around 60 μm. As it was discussed, the median filter only blurs the attenuation at the border of different tissues, and it affects the local statistical numbers minimally.

The statistical numbers for different tissue types have been calculated within the manual delineated regions. Other tissue types such as loose connective tissue, proteoglycans, calcified nodules and smooth muscle cell-rich fibrous tissue were not assessed in the present study because of the limited study sample size and the absence of specific staining [89]. Artifacts would inevitably affect the light property analysis. These points can be limitations in the future for tissue classification, and subjects for a further investigation.

3.5.5 Future directions

Generating a distribution map indicating the probability of each type of plaque is one of the interesting directions in future work. Towards this goal as it has been proposed in literature [74], the following works need to be done. Enough features should be extracted, including the first and second order statistical features [75] of intensities, attenuation coefficient and backscatter term, the power spectrum parameters, etc. Feature selection should be used to remove strongly linear related features, which can result in a non-invertible covariance matrix. Then a likelihood density map can be generated for each type of tissue. For a fair comparison between tissue types to determine the most likely tissue type for each pixel, the prior probabilities are necessary to be obtained in advance. Usually, manually reviewing a pullback series is time-consuming and points of interest easily cannot be overlooked due to the huge amount of data (up to over 1000 images). Integrated with the automated lumen detection in QCU-CMS [47], carpet views as shown in Fig 3.13 and 3.14 can be generated robust and fast without the need of predefining the segmentation of the lumen tissue. This overview of the examined coronary vessel wall can potentially improve the abnormality determination and further help with the treatment decision [93, 94] for coronary diseases, e.g. for stent placement and risk assessment of the patient in an automated way which is lacking in the current clinical practice.

3.6 Conclusion

In order to differentiate atherosclerotic tissue with IVOCT images, the depth-resolved approach has been implemented in the intravascular OCT images to robust estimate the attenuation coefficient and the backscatter term. A cut-off algorithm has been proposed to efficiently exclude noisy regions. The reported values for each type of tissue are consistent with the findings in the literature. Despite assumptions are made in the DR approach, statistical analysis shows that the estimated attenuation coefficient and the backscatter term can differentiate six tissue types in the lumen vessel; mixed calcified

plaque, fibrous, calcification, lipid, macrophages and necrotic core in combination with the image intensity.

CHAPTER FOUR

HISTOGRAM-BASED STANDARDIZATION OF INTRAVASCULAR OPTICAL COHERENCE TOMOGRAPHY IMAGES ACQUIRED FROM DIFFERENT IMAGING SYSTEMS

Abstract — Intravascular optical coherence tomography is widely used for analysis of the coronary artery disease. Its high spatial resolution allows for visualization of arterial tissue components in detail. There are different systems on the market, each of which produces data characterized by its own intensity range and distribution. This limits the comparison of the results, especially when intensity values are used. In order to overcome the difference in the intensity range and distribution, we developed an intensity mapping framework to match intensities based on an exact histogram matching technique. Experiments were performed with aligned data from systems of the two major vendors, St.Jude and Terumo. A leave-one-out cross validation was used to compare the global and local schemes for the determination of the target histograms. Our results show that: 1) The intensities can be matched well with good generalization, and 2) Even though the local scheme marginally outperforms the global scheme, the latter is better suited for practical usage.

This chapter is based a submitted manuscript: S. Liu, O. Dzyubachyk, J. Eggermont, S. Nakatani, B. P. F. Lelieveldt, and J. Dijkstra, **Histogram-Based Standardization of Intravascular Optical Coherence Tomography Images Acquired from Different Imaging Systems**, *Med. Phys.*, Accepted for publication.

4.1 Introduction

Cardiovascular diseases (CVDs) are the leading cause of death worldwide [31]. Introduction of intravascular optical coherence tomography (IVOCT) has largely advanced understanding and treatment of one of the most common CVDs, the coronary artery disease [5, 14, 8, 15]. Design of IVOCT enables visualization of superficial tissue structures of the arteries with resolution as high as 5–10 μm. The wavelength of its light source is around 1300 nm, which permits a relatively deep penetration into the vessel wall. The *intravascular* term indicates that the images are acquired from the inside of the blood vessel. For current commercial systems, this is achieved by inserting a catheter into the coronary artery, pushing away the blood by injecting a flush media and pulling it back through the lesion location. The catheter has been designed to emit near-infrared light towards the artery wall and to receive the back-propagated light. The received light is recorded as a one-dimensional signal (A-line) containing the back-propagated intensities ordered by ascending distances to the catheter. By rotating the catheter tip with a constant speed, two-dimensional images can be generated. Centering at the catheter, each cross-sectional image contains about 500 A-lines from different directions. These A-lines are recorded as a raw image in polar coordinates, as shown in Fig. 4.1(b,e), or transformed into the Cartesian coordinates, as shown in Fig. 4.1(c,f). As the catheter is pulled back at a constant speed using a motorized pullback device, a stack of images, referred to as a *pullback* is acquired.

The use of IVOCT in clinical studies increases exponentially [15]. Because of its high resolution, IVOCT contributed to confirmation of pathological findings on progression of (neo)atherosclerosis by visualizing morphologies like intimal erosion, fibrous plaque, calcified nodule, lipid pool, macrophages distribution, intraluminal thrombus, etc. [95, 4, 96, 97, 98, 99, 100]. Attracted by the conspicuous clinical prospects, many efforts were paid to detection and characterization of IVOCT morphologies, such as fibrous, lipid-rich and calcified plaques [18], macrophages distributions [95], thrombus [101], side-branches [102, 103], struts [104, 105, 44] and struts embedding [106] with image intensities, and/or optical parameters [28, 40]. However, diversity of IVOCT data can limit comparison of the results, especially when intensity values are used. In particular, there is no consented standard for the imaging range, unlike e.g. in computed tomography (CT), meaning that IVOCT images generated with different commercially available systems are typically characterized by different intensity ranges. The most commonly used commercial systems are Illumien Optis from St. Jude Medical (St. Paul, MN, USA), which saves the raw data in a 16-bit format, and Lunawave from Terumo (Tokyo, Japan), which saves the raw data in a 8-bit format.

As a concrete example, the Cartesian images from these two systems are shown in Fig. 4.1(c,f), and their polar counterparts are shown in Fig. 4.1(b,e). Images were acquired shortly after each other during the same intervention at the same location inside an artery of one patient. The histograms of the corresponding regions on the IVOCT images acquired by the two systems

indicate different intensity ranges within the same tissue type. Furthermore, different shape of these histograms suggests that relationship of intensities between these two systems is not simply linear. In fact, an exponential relationship has been observed in our previous work [88].

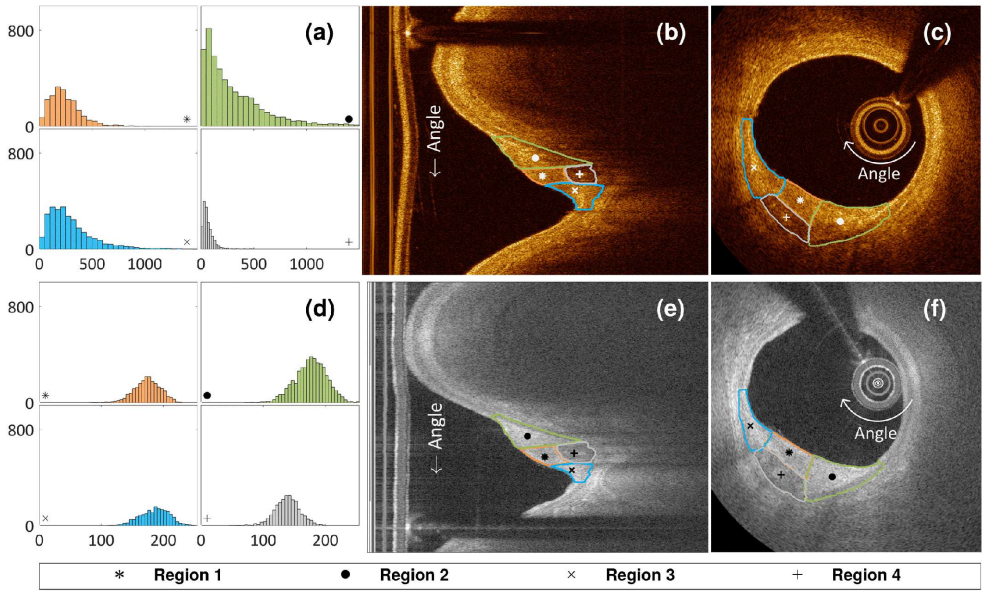

Figure 4.1: Histograms (a) of regions delineated in St.Jude polar (b) and Cartesian (c) images. Histograms (d) of regions delineated in Terumo polar (e) and Cartesian (f) images. Side-branches and lesions were used as landmarks to find the corresponding locations in St.Jude and Terumo images. Regions were separated according to their morphological appearance and visible borders and are correspondingly delineated in the polar images. Delineated regions on both polar and Cartesian images and the corresponding histogram bars are shown using the same colors.

Most OCT studies used the same type of IVOCT system to guarantee high reproducibility. On the other hand, doing so limits the scope of developed applications: when the same method is applied to data from another vendor that has different intensity distribution, repeated validation is required. To improve efficiency of development, images need to be standardized across devices. Only few papers on this topic have been published in the IVOCT field, whereas several papers on increasing the comparability of ophthalmological OCT images were published. In particular, a normalization approach was proposed for comparing images from two vendors [107]. This approach involves three steps: density scaling and sampling, noise reduction, and amplitude normalization. It was later improved by integrating virtual averaging [108]. This A-line normalization approach was shown to reduce the measurement difference [109] and the appearance disparity [110].

In this work, we explore the possibility of converting the data between different OCT systems and propose a matching scheme with good generalization and minimal loss of detail. Our pretrained algorithm can also be used for intensity matching when the target data is not given. By doing this, when a method developed for data acquired with system-A needs to be evaluated with data acquired with system-B, we can modify the data from system-B to follow the intensity distribution of system-A, such that the method can be tested on the data from system-B with minimum modification. Such data conversion is referred to as the *histogram modification* [111, 112, 113, 114]. The basic histogram matching theory has been proposed in the work of Hummel et al. [111]. Since then, this study has been widely used as the fundamental theory in image modification studies at the histogram level. Later, the exact histogram specification (EHS) was proposed as a successful discrete solution to the model in practice [112, 113, 114]. This approach was used to produce comparable measurements in ophthalmological OCT images generated with low signal strength to that generated with high signal strength [115] and to compensate light attenuation in confocal microscopy [116].

Our main goal in this paper is to propose a framework for matching intensities in OCT images from different vendors using EHS. A straightforward approach would be to match intensities per pullback. We compare this *global* scheme to a *local* scheme that takes the local intensity variations into the consideration. All the analysis is conducted with raw polar images, whereas the Cartesian images are only used for the visualization of results. The *in vivo* patient data used in this study is unique in the sense that both St.Jude and Terumo pullbacks were specially acquired for this study. More elaborate explanation of this is provided further in the manuscript.

The paper is structured as follows. For better understanding of the underlying principles and terminology, we explain both the model and the EHS in Section 4.2. In Section 4.3, the data and its processing are described, the distance measures are introduced, and the matching schemes are proposed and validated. Results are reported and discussed in Section 4.4 to Section 4.6. Finally, in Section 4.7 we draw the conclusions.

4.2 Theory and terminology

Each 2-D image can be represented as a matrix $I(x, y)$, which is the discrete subsample of a bounded surface function $f(x, y)$, where $\{(x, y) \mid 0 \leqslant x \leqslant N, 0 \leqslant y \leqslant M\}$. The intensity function $f(x, y)$ follows a distribution function $P_f(t)$ that indicates the chance of $f(x, y)$ being less or equal than t. Given two images $f_s \sim P_{f_s}(z_s)$ and $f_t \sim P_{f_t}(z_t)$, the goal of histogram transformation is to search for a mapping T such that composition $T \circ f_s \sim P_{f_t}(z_t)$. In this work, f_s and f_t are referred to as the source and the target image, respectively. This search has been formulated by Hummel et al.

[111] as an optimization problem:

$$\hat{T} = \arg\min_{T} \int_{a_1}^{a_2} \left[p_{T \circ f_s}(z) - p_{f_t}(z) \right]^2 dz, \tag{4.1}$$

where $[a_1, a_2]$ defines the range of image intensities. Here $p_X(z)$ is the probability density function (*pdf*) of image X, which is the derivative of the distribution function $P_X(z)$, and z is intensity level.

A unique monotonic solution of this model was given in [111]:

$$\tilde{T}(z_s) = P_{f_t}^{-1}\left(P_{f_s}(z_s)\right),\ p_{f_s}(z_s) > 0,\ \text{for } \forall z_s. \tag{4.2}$$

In practice, p_X in both source and target spaces is usually estimated as the normalized histogram vector: $p_X = \left\{ p_i \mid \sum p_i = 1, i \in \{0, ..., 2^{L_0} - 1\} \right\}$, where L_0 denotes the maximum gray level of the images, p_i denotes the frequency of the image intensity corresponding to the interval $[z_i, z_{i+1})$. Conventionally, the interval is referred to as a *bin*; $\{z_i\}$ are the bin edges; the average of every two adjacent bin edges $c_i = (z_i + z_{i+1})/2$ is the bin center, and p_i is the bin value. We define the bin edges for the i_{th} bin as $[c_i - 0.5, c_i + 0.5)$ in this work.

To ensure that the distribution function P_X is monotonically increasing, the following approximation is used:

$$P_j = \frac{c_j - z_j}{z_{j+1} - z_j} p_j + \sum_{i=0}^{j-1} p_i. \tag{4.3}$$

This approximation is equivalent to interpolating $P_j(z)$ for $z \in [z_j, z_{j+1})$ with a piecewise-linear function, the slope of which is p_j and the intercept is $\sum_{i=0}^{j-1} p_i$. Using this monotonic approximation, $\tilde{T}$ can be estimated with Eq. 4.2. However, this estimation only shifts bins centers, and splitting of bins is not possible. This becomes especially problematic when the source and the target images are within different intensity range, such as e.g. transforming 8-bit images to 16-bit images or the other way around. Since the bins cannot be split, information can only be retained based on the image that is represented by less bins. Attempts have been made to include local information [111] (local mean, entropy, etc.) into the objective function as a "context-aware" term, but doing so introduces more parameters, and the transformed images tend to be blurred.

The aforementioned issues can be overcome by a technique called exact histogram specification (EHS) [113, 114, 112]. In the following, we will use the previously introduced notations. For an image of size $M \times N \times P$ with gray values in $\{0, 1, ..., 2^{L_0} - 1\}$, the histogram divides $M \times N \times P$ pixels into 2^{L_0} bins. The fundamental idea behind EHS is to strictly order all the pixels, such that the ordered pixels can be divided according to any given target histogram. This usually cannot be done by using intensities only, thus auxiliary information needs to be introduced.

Local means and wavelet coefficients have been reported to be successful source of auxiliary information for achieving strict ordering [113, 114]. In a

more recent study [112], a moderately improved performance in nature images has been reported with a proposed auxiliary term involving three hyper-parameters. Compared to the other two aforementioned approaches, local-means approach better copes with noise and involves no hyper-parameters, thus it is chosen in this study as the noise level of OCT images is known to be high.

Considering the intensity at each pixel as the first scale of the local mean, for each pixel i we calculate a vector of multi-scale local means with increasing window size $\boldsymbol{\mu} = [\mu_1(i), \mu_2(i), ..., \mu_K(i)]$, K being the number of scales. Consequently, all the pixels in the image can be ordered lexicographically with a relational operator defined as:

$$\left\{ i \prec j \mid \mu_\ell(i) = \mu_\ell(j)\ _{\forall \ell < \ell_0},\ \mu_{\ell_0}(i) < \mu_{\ell_0}(j) \right\}. \tag{4.4}$$

As result of using this approach, pixels in one image are expected to be ordered strictly by using just a few scales. It was observed that $K = 6$ scales are usually enough to arrange all the pixels in a strictly ascending order [113]. Once the strict ordering is achieved, the pixels can be easily grouped again following the histogram defined in the target image.

In practice, the EHS is often used to estimate the target image(s) given the source image(s) and the target histogram. In our case, however, the target histogram is unknown and should first be defined using a group of matched source and target images. Thus our task is two-fold: 1) To estimate the target histogram(s) from the matched images, and 2) To apply the estimated histogram(s) to a new source image. The following section describes our method in full detail.

4.3 Materials and methodology

As it was previously elaborated, the key step for using EHS is to define the target histogram.

4.3.1 Global and Local matching schemes

To determine the target histogram, the most straightforward approach is to use the overall histogram generated with all the images. However, using the global histogram as a reference might result in information loss as some of the less represented tissue structures might get overshadowed in the global histogram. Using local histograms might help resolving this issue.

Therefore, we introduce a *Global* scheme and a *Local* scheme for determination of the target histogram. For applying the Local scheme, each pullback is split into smaller sections (our pullback alignment and splitting algorithm is described in the following section). For providing a formal definition, we denote the database of matched histogram pairs as $\mathcal{H} = \{(H_1^k, H_2^k) \mid k = \overline{1, N_H}\}$, where H_1^k denotes the histogram of k^{th} section in

the original space (e.g. St.Jude), H_2^k denotes its counterpart in the target space (e.g. Terumo), and N_H is the size of the database.

For matching a given image with histogram H_1^*, the Global scheme uses one overall histogram as the target histogram, i.e.:

$$H_2^G = \sum_{k=1}^{N_H} H_2^k. \tag{4.5}$$

The Local scheme determines the target histogram for each section as the second component of the database entry whose first component is the most similar to H_1^*.

$$H_2^L = H_2^{\operatorname{argmin}_{k=\overline{1,N_H}} d(H_1^*, H_1^k)}. \tag{4.6}$$

Here $d(H_i, H_j)$ denotes dissimilarity between two histograms H_i and H_j. The remainder of this section describes creation of the histogram database and introduces the dissimilarity measures.

4.3.2 Data description and alignment

In our case, the target histogram is estimated using a dataset of matched images. As the final goal of this study is to transform OCT images both from intensity space of St.Jude system (St.Jude space) to that of Terumo system (Terumo space) and the other way around, the target histograms in both St.Jude and Terumo spaces need to be determined. To achieve this, eight *in vivo* pullbacks were acquired from left anterior descending artery (LAD) of two different patients, marked as A and B. The data acquisition strictly followed the clinical guideline of Sakurabashi Watanabe Hospital (Osaka, Japan), and the analysts from Leiden University Medical Center (Leiden, The Netherlands) were blinded from all patients' information. For each patient, IVOCT pullbacks from the same vessel segment were acquired shortly after each other with St.Jude and Terumo systems, before and after the stent implanting procedure. As a result, four pairs of corresponding St.Jude–Terumo pullbacks were made available for the study. The St.Jude pullbacks were acquired at a pullback speed of 36 mm in 180 frames per second with a frame interval of 0.2 mm, and the Terumo pullbacks were acquired at a pullback speed of 40 mm in 158 frames per second with a frame interval of 0.25 mm. Raw polar images as provided by the vendors are used in this study. St.Jude images are 16-bit "linear" with a transversal pixel size of 0.0050 mm, and Terumo images are 8-bit "log-like" compressed with a transversal pixel size of 0.0049 mm.

Due to different distal and proximal locations in two corresponding pullbacks, images within overlapping part of the vessel should be matched. We determine the start and the end frames of overlapping part by searching for identical side-branches that are closest to the proximal and the distal parts of the pullbacks. Since we primarily aim at analyzing the tissue region, images with stent struts points are excluded (more elaborate discussion about this is provided in Section 4.6).

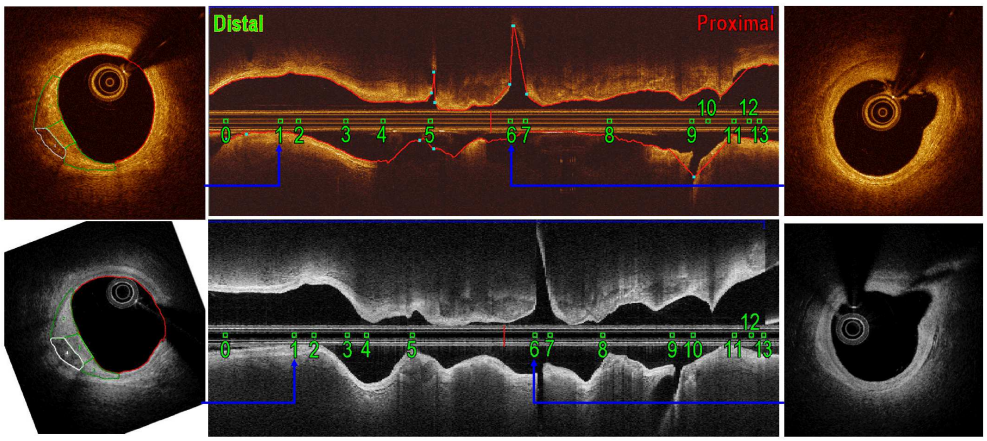

Figure 4.2: The landmarks for aligning the pullbacks.

Compared to the histogram of the entire overlapping part of pullbacks, histograms of smaller sections may preserve more local structural information. Therefore, we further split the overlapping part into small sections using key frames defined by two main types of anatomical landmarks (as shown in Fig. 4.2): the side-branches and the tissue types with identical patterns, e.g. culprit lesion visible in Fig. 4.1(c,f). For the post-stenting pullbacks, the proximal and distal edges of the stent struts are also considered to be crucial landmarks. Key frames were identified independently by two experienced IVOCT readers, using QCU-CMS (Quantitative Coronary Ultrasound—Clinical Measurement Systems; Leiden University Medical Center, Leiden, The Netherlands), which is the research version of QIVUS (Quantitative IntraVascular UltraSound; Medis, Leiden, The Netherlands). Only landmarks with consensus were selected.

Even though the catheter is pulled back with a uniform speed, the number of frames within a certain section can be affected by the heartbeat cycle, slight bending of the artery, interaction between the catheter and the artery wall, and so on. Due to this effect, finer splitting or frame-to-frame matching is not possible without introducing an interpolation error.

Table 4.1 gives an overview of the aligned data. Patient-A had no stent planted beforehand, while Patient-B did have one. Hence, the number of frames without stent struts in Patient-B is smaller than in Patient-A. Overall, the pullbacks were aligned with twenty-three key frames. Within these frames, regions of clinical interest (ROI) were delineated based on their appearance and visible borders according to the consensus [8]; see Fig.4.1. In total, we have eighteen corresponding pairs of sections and thirty-eight ROIs. After correspondence between the sections had been established, the database of matched histogram pairs was generated using foreground regions bounded by the lumen border and 1 mm behind. This corresponds to the depth of 200 pixels

Table 4.1: Data description

Patient	Treatment	St.Jude				Terumo				Landmark	Section	ROI
		PL[a](mm)	All[b]	Max[b]	Min[b]	PL[a](mm)	All[b]	Max[b]	Min[b]			
A	Pre-stenting	108	507	80	10	168	389	88	9	14	13	32
	Post-stenting	108	69	52	17	147	53	41	12	4	2	4
B	Pre-stenting	75	40	21	19	152	33	19	14	3	2	1
	Post-stenting	75	12	12	12	111	10	10	10	2	1	1
Total			628	80	10		485	88	9	23	18	38

ROI	Adventitia	Calcification	Fibrous	IML[c]	Lipid	Neointima	Total
No.	4	11	10	4	3	6	38

[a]PL: total length of the entire pullback
[b]All, Max, and Min: the total, maximal, and the minimal numbers of frames in the aligned sections
[c]IML: intima-media layer

in St.Jude polar image and 204 pixels in Terumo polar image. The lumen border is detected by the QCU-CMS software in an automated manner.

4.3.3 Dissimilarity between histograms

The Euclidean and the Kolmogorov-Smirnov distances are used for comparing two histograms. They are first used in the analysis of the local variations and, after that, for evaluation of matching schemes.

For calculating the distances, the histograms are normalized to obtain the probability density functions (*pdf*'s) and the corresponding cumulative density functions (*cdf*'s). The Euclidean distance for measuring dissimilarity between two *pdf*'s $\boldsymbol{p}$ and $\boldsymbol{q}$ is defined as:

$$d_{x2}(\boldsymbol{p}, \boldsymbol{q}) = (\boldsymbol{p} - \boldsymbol{q}) \cdot (\boldsymbol{p} - \boldsymbol{q})', \tag{4.7}$$

the discrete approximation of which is equivalent to the objective function in Eq. 4.1. The Kolmogorov-Smirnov distance measures dissimilarity between the distribution functions (also known as *cdf*'s) $\boldsymbol{P}$ and $\boldsymbol{Q}$:

$$d_{KS}(\boldsymbol{P}, \boldsymbol{Q}) = \max_i |P_i - Q_i|. \tag{4.8}$$

4.3.4 Validation

Leave-one-out validation is used to compare the Global and Local schemes. One of the four pullback pairs is left out in turn, and the target histogram is determined with the other three. Consequently, the intensities of the left-out pullback are matched. As part of each leave-one-out experiment, median intensities within each ROI are compared in both target and matched images. The target and matched median values are shown in the scatter plot and compared in the Bland-Altman plot. The scatter plot can show whether two groups of data are linearly related and how much the trend line deviates from the diagonal line, which is the ideal case indicating that two groups of data

match perfectly. The Bland-Altman plot shows the average versus the difference of each two compared values, which reveals the difference of two groups of data more explicitly. The mean and the standard deviation values of the difference are also called the systematic difference and the random error. With a properly low random error, the closer the systematic difference to zero level is, the more likely that two groups of data are originating from the same distribution. For reference, also the key frames are matched using the target histograms extracted directly from their corresponding aligned frames.

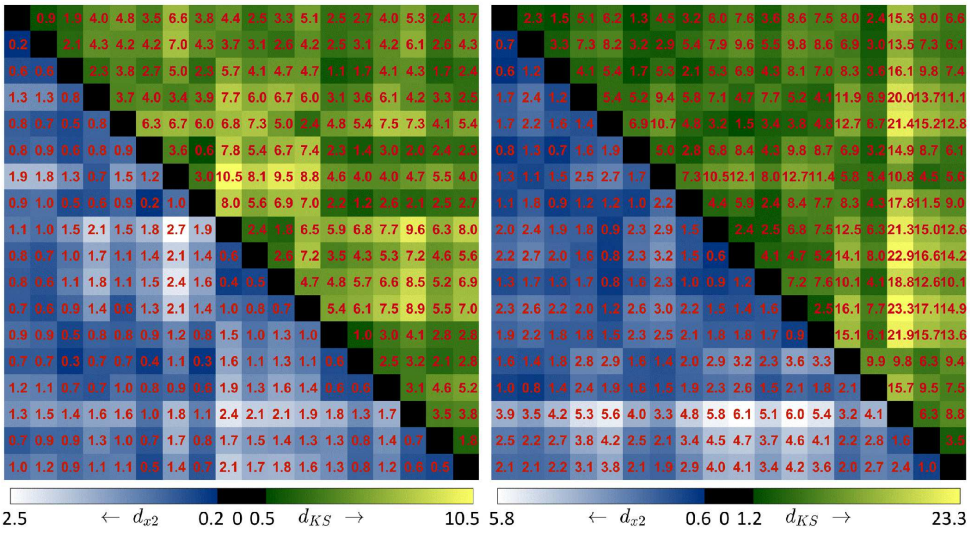

Figure 4.3: The distances between all the histograms in the database for St.Jude (left) and Terumo (right) spaces. All the distances were multiplied by a factor of 100 for presentation purposes. In each distance map, d_{x_2} and d_{KS} are shown in the lower and upper triangles, respectively.

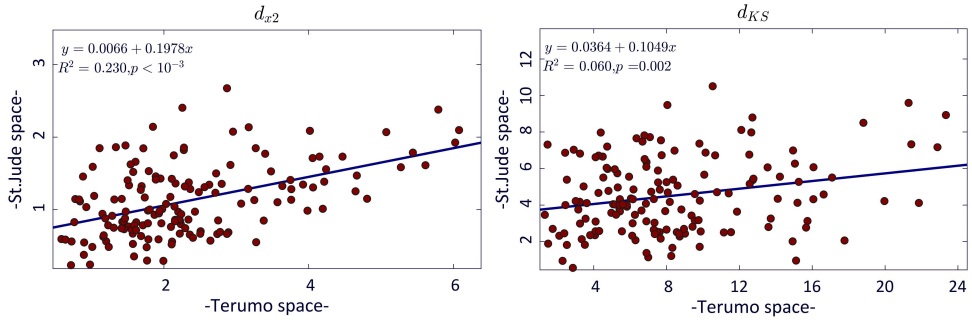

Figure 4.4: Linear regression of distances of all the histograms in our database for St.Jude and Terumo.

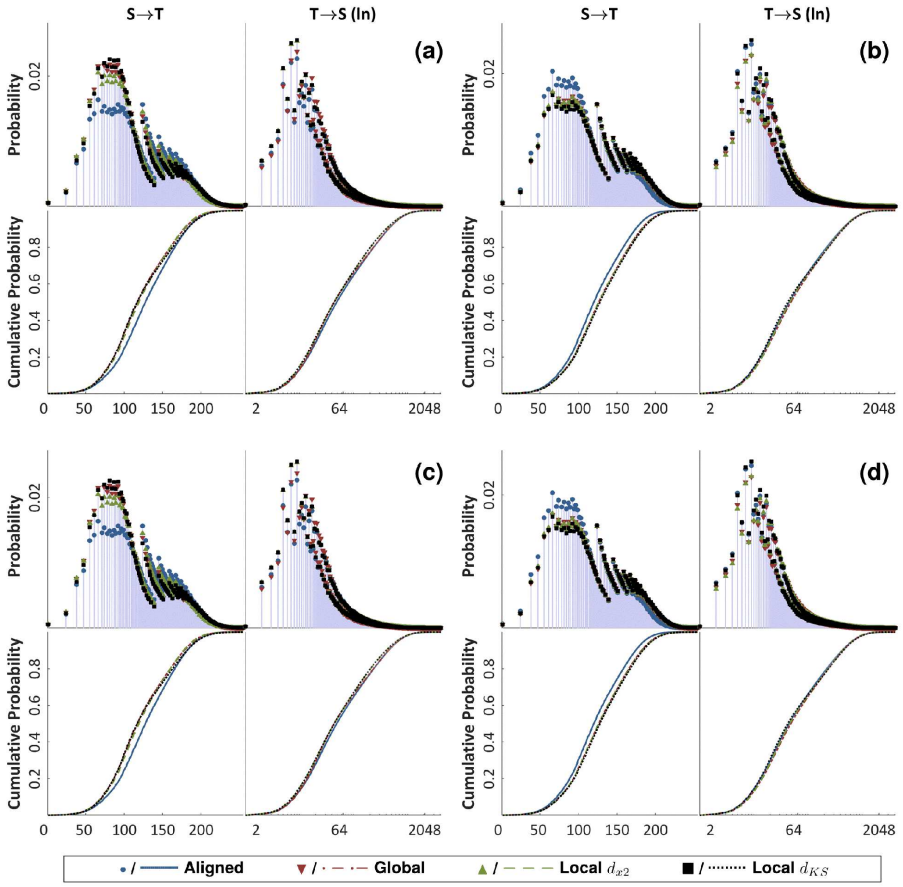

Figure 4.5: The aligned and trained probability and the cumulative probability distributions for leaving the 1st (a), the 2nd (b), the 3rd (c) and the 4th (d) pullback out. Target profiles for both St.Jude (S→T) and Terumo (T→S) images are shown. For the latter case, the x-axis is shown in the logarithm scale (ln) for the sake of better visualization.

4.4 Results

We calculated the distances between all the histograms in two spaces. Figure 4.3 gives a general overview of all the dissimilarities. In the scatter plot of distances in Fig. 4.4, we observed a linear trend and further performed the regression analysis. The statistical results show that the dissimilarities in two spaces are correlated significantly with $p<0.005$. This validates the assumption and supports the Local matching scheme.

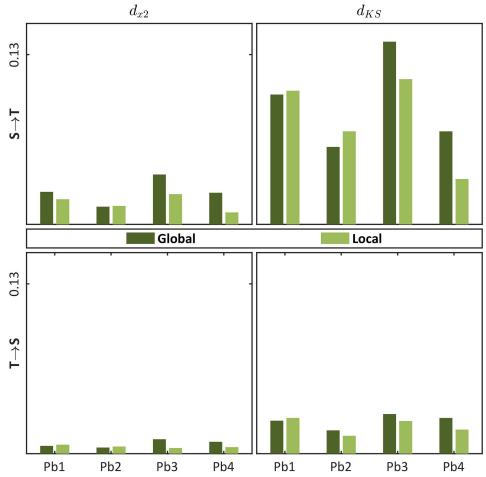

Figure 4.6: The bar chart of the distances for leave-one-out experiment for matching St.Jude to Terumo (S→T) space and Terumo to St.Jude (T→S) space. 'Pb' = 'pullback'.

Results of the leave-one-out validation for both St.Jude-to-Terumo (S→T) and Terumo-to-St.Jude (T→S) images are reported in Figs. 4.5, 4.6 and summarized in Table 4.2. For a section containing 70 images, generating the histograms takes 10 seconds. For the Local scheme, the time for searching in our database of 34 histograms using our Matlab (MathWorks, R2016a with Statistics and Machine Learning Toolbox) implementation is 1.25 seconds. Figure 4.5 shows the estimated target probability profile (normalized histogram) together with that determined by the aligned data (in red color; will be further referred to as the *aligned histogram*). The corresponding cumulative probability plots are shown as well. Both d_{x2} and d_{KS} are shown as bar charts in Fig. 4.6, and the numbers are reported in Table 4.2. The distances between matched and reference distributions for both Global and Local schemes are low and robust; see Fig. 4.6 and Table 4.2. The average distance of all four validation experiments (*Aver* in Table 4.2) indicates that, in general, the Local scheme outperforms the Global scheme.

Table 4.2: Results of leave-one-out cross validation

		S→T					T→S				
		Pb1	Pb2	Pb3	Pb4	*Aver*[a]	Pb1	Pb2	Pb3	Pb4	*Aver*[a]
d_{x2}	Global	.0248	.0135	.0381	.0241	.0251	.0058	.0046	.0110	.0090	.0076
	Local	.0192	.0141	.0231	.0091	***.0164***	.0069	.0053	.0042	.0049	***.0053***
d_{KS}	Global	.0994	.0593	.1398	.0711	.0924	.0252	.0179	.0303	.0273	.0252
	Local	.1022	.0724	.1110	.0347	***.0801***	.0276	.0137	.0246	.0183	***.0210***

[a] The average performance of all the four leave-one-out experiments.

Scatter plots and Bland-Altman plots of the median intensities within ROIs are shown in Fig. 4.7. When comparing intensities in St.Jude space, an increasing trend is observed in the absolute systematic error; see Fig. 4.7(b,e,h,k). Following the conventional statistical procedure for Bland-Altman analysis [117], the St.Jude intensities were compared in the logarithm scale; see Fig. 4.7(c,f,i,l). Without an obvious trend in Terumo space, the intensities are compared in the linear space; see Fig. 4.7(a,d,g,j).

For the reference matching between the corresponding key frames, the systematic differences are -4.50 for S→T and 0.15 for T→S; see Fig. 4.7(a,c).

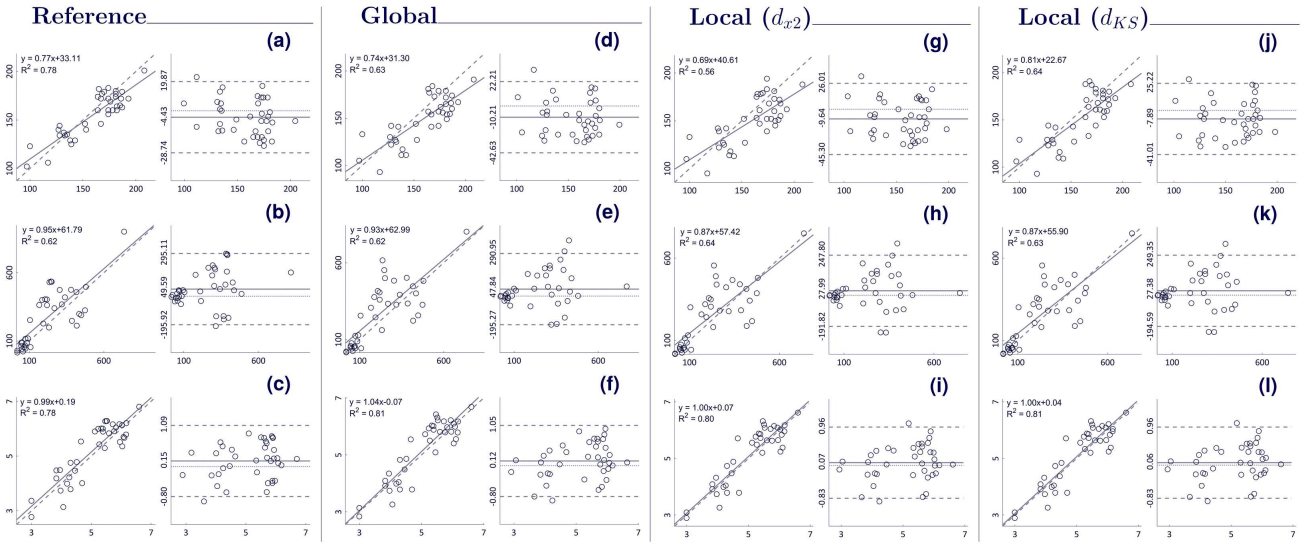

Figure 4.7: Scatter and Bland-Altman plots for comparing the median intensities within ROIs in target and matched frames ($n = 38$). Reference intensities, matched according to the aligned key frames (a,c), compared to that matched with the Global scheme (d,f), the Local scheme with d_{x_2} (g,i) and the Local scheme with d_{KS} (j,l). In the scatter plots, the regression line is shown as the solid line and the dashed line indicates the $y = x$ line. In the Bland-Altman plots, the x-axis and the y-axis are the average and the difference of the target and matched intensities, respectively. The solid line indicates the mean error, and the dashed lines mark the 95% confidence interval. The matched intensities are compared in Terumo (a,d,g,j), St.Jude (b,e,h,k) and logarithmic St.Jude (c,f,i,l) spaces, respectively.

This difference is the most likely to be caused by the selection of data and is independent of the scheme used. Using this intrinsic systematic difference as a reference, the absolute systematic differences yielded by the Local scheme are relatively small: 9.67 (S→T) and 0.07 (T→S) for d_{x2}, 7.92 (S→T) and 0.06 (T→S) for d_{KS}, compared to the Global scheme: 10.26 (S→T), 0.12 (T→S). Taking into consideration the described intrinsic difference, the Local scheme yields absolute values closer to zero for both S→T and T→S matching. All comparisons in Bland-Altman analysis suggest that the Local scheme outperforms the Global scheme for EHS-based intensity transformation in IVOCT images between St.Jude and Terumo systems. The images matched with the target histogram determined by the Global scheme are shown in Fig. 4.8. The matched images, see Fig. 4.8(e–h,m–p), and the corresponding aligned images, see Fig. 4.8(a–d,i–l), show comparable intensity levels in both St.Jude and Terumo spaces.

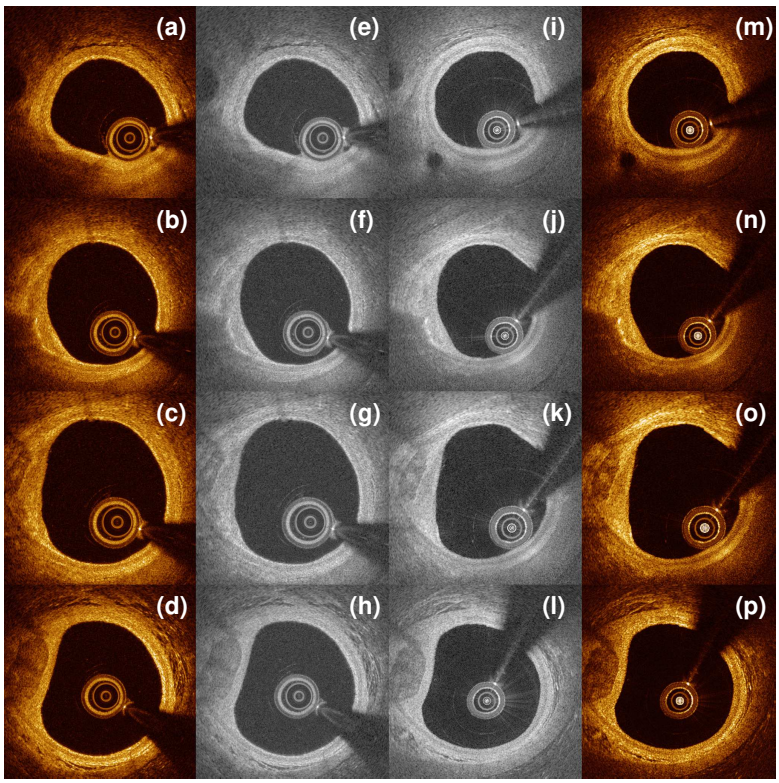

Figure 4.8: Images matched using the Global scheme. Raw St.Jude images (a–d) were mapped to the Terumo intensity space (e–h). Raw Terumo images (i–l) were mapped to the St.Jude intensity space (m–p). For visualization, St.Jude images are shown in its conventional golden color scheme.

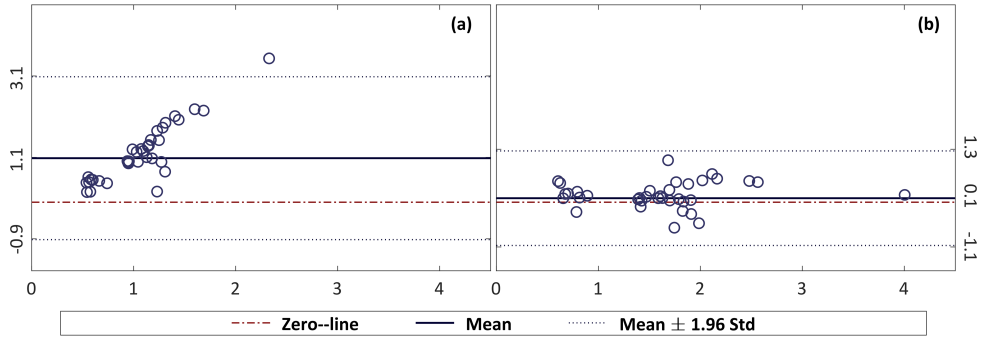

Figure 4.9: Bland-Altman plot of the comparison between estimated attenuation coefficients in ROI's in (matched/original) Terumo images and in corresponding ROI's in St.Jude images. (a) Attenuation values were estimated directly using original Terumo images. (b) The values were estimated using the Terumo images matched to St.Jude intensity space. Here 'Std' stands for 'standard deviation'.

4.5 Comparing attenuation coefficient values

One of the post-processing steps in IVOCT data analysis is estimation of the attenuation coefficients, which are defined as the distinction rate of light passing through a volume of tissue with a unit of μm^{-1}. It is considered to be a key feature for identification of different tissue types in the arterial wall. In our previous work [118], we reported the depth-resolved (DR) estimation using St.Jude images. However, applying this estimation directly to Terumo images results in values in different range. Therefore, we applied this estimation approach to the matched Terumo images (in St.Jude range) to validate the assumption that proposed matching scheme facilitates generalization of the attenuation estimation algorithm developed for St.Jude data to Terumo images. The results described above show comparable performance for both schemes. We further illustrate performance of the Global scheme for the estimation of attenuation coefficient using the DR method.

The attenuation was estimated both in the matched and original Terumo images. The median values within ROIs were compared to those estimated using St.Jude images. The paired t-test at 5% significance level was used with a null hypothesis that the mean difference between two sets is zero.

Figure 4.9 shows the Bland-Alman plots of the comparison of median attenuation coefficient in ROIs in (matched/original) Terumo images and in corresponding ROIs in St.Jude images. In the plot presented in Fig. 4.9a, original Terumo images were directly used for the estimation. Comparing to those estimated using the corresponding St.Jude images, the points are not evenly distributed around the zero-line, and both systematic difference and the range of random error are high. Paired t-test indicates that the mean difference is significantly different from zero with $p < 0.001$, and the 95% confidence interval (CI) is [0.74,1.42]. In Fig. 4.9b, the matched Terumo images were used

for the estimation. In this case, the difference with the values estimated using the St.Jude images is much smaller, which is indicated by lower systematic difference and random error range, and the points are more randomly distributed around the zero-line. For this case, paired t-test gives $p = 0.320$ with a 95% CI of [-0.10,0.30].

4.6 Discussion

Clinical significance of IVOCT structures has been reported extensively in clinical research. The use of IVOCT for the analysis of CADs grows exponentially. For more efficient analysis with minimum manual intervention, automated methods for tissue quantification, characterization, and classification are needed. However, lack of standardized image intensities can increase the difficulty of designing algorithms or restrict the possibility of generalization of algorithms developed for one specific imaging system. Therefore, standardizing image intensity is a crucial processing step to speed up the development and validation of methods for intravascular tissue analysis.

This study aims at exploring a proper scheme to match IVOCT image intensities with the local-mean EHS technique. In our case, the most essential step is to determine the target histogram. Preliminary statistical analysis suggests that distances in both spaces are significantly correlated. Based on this analysis, we propose a Local matching scheme and compare it with the Global scheme. Target histograms determined with both schemes turned out to be successful in matching IVOCT intensities at relatively low cost. In this, Local scheme marginally outperforms the Global scheme, which is in line with the results of our preliminary statistical analysis. Moreover, the attenuation estimation experiment presented in Section 4.5 illustrates benefits of using the Global scheme in practice by showing that it, in particular, largely improves the compatibility of the estimated attenuation coefficient across vendors.

Significant variation in the histograms of different sections is caused by many reasons, the difference in tissue composition being the major factor. As it has been reported in [8], tissue types are mainly visually assessed by recognizing bright speckle, presence of following shadow, sharpness of border, etc. Quantitative results confirm that these image structures yield variations in the histogram. Our previous study [90] demonstrated that image intensities can also be affected by position of the catheter. This effect can cause large variation in distances and thus can explain the low R^2 in the reported statistical analysis.

The Bland-Altman analysis shows a systematic difference in median intensities within selected regions of interest, even when the exact histogram is specified using the matched key frames. This intrinsic variation may be caused by many factors, such as the data alignment bias, intrinsic difference in systems for data acquisition, etc. Although this difference is relatively low, it should be accounted for in future applications of this method.

For clinical application, both schemes can also be easily embedded as an independent function for automated intensity standardization. For the global

scheme, the target histogram needs to be saved within the program. During calculation, this target histogram is loaded and used in EHS. For the local scheme, the database of histogram pairs needs to be saved. During calculation, the target histogram needs to be searched in the database and then it is used in EHS. Furthermore, the proposed experimental setup is not limited to the two considered IVOCT systems and can be used to standardize image intensities between other OCT systems or even for other modalities, e.g. MRI. Matching images to St.Jude or Terumo images can also further speed up the validation of newly developed IVOCT systems. As long as the order of intensities of different structures in both systems is consistent, strict ordering can be applied to insure that the exact histogram can be specified.

In this work we developed and presented a framework for minimizing intensity variation between two different IVOCT systems. At the same time, there might be variations caused by differences between systems from the same vendor, differences between catheters for the same imaging machine, and even differences in the pullbacks acquired using the same hardware and catheter. Since the images were calibrated by design during the acquisition, we expect these variations to be small.

Bare metal stents (BMS) were implanted in two out of the four pullbacks used in this particular study. Due to their high light reflectance, the BMS struts appear on the images as saturated bright spots with dark shadows behind them. They disturb the intensity distribution. Since this work mainly focused on matching images of the arterial tissue, images with stent struts were deliberately excluded from the analysis.

4.6.1 Limitation

The data used in this study is specially generated for construction of this intensity matching framework. Performing (virtually) simultaneous acquisition with two IVOCT systems is not done in clinical practice. Therefore, the amount of data used in this study is limited, which is a major limitation of this work. However, this data is unique and more representative for the analysis on intensity matching than *ex vivo* and animal data. Furthermore, results of leave-one-out validation show reasonable robustness through pullbacks and patients. At the same time, we acknowledge that extending the histogram database might potentially improve the histogram matching as using a larger database will most likely lead to more reliable estimation of the target histograms for both Global and Local schemes.

4.6.2 Future work

This histogram matching scheme will be used for standardization of IVOCT image intensities as a crucial first step for further quantification. Our future work will focus on comparing the outcome of existing quantification methods, such as attenuation estimation, quantification of the degradation of

bio-resolvable struts and differentiation of neointima, to data acquired by different IVOCT systems.

Once the matching framework is extensively validated, this approach can be routinely used as a pre-processing step for data standardization. The standardized images can be used for development of universal algorithms for segmentation (of e.g. fibrous cap of TCFAs) or tissue analysis (e.g. for estimation of attenuation coefficients).

In this study, we did not include the stented segments of the pullbacks due to the high reflectance of the metallic struts. However, for future work the database could be extended with the stented segments of the pullbacks by excluding individual strut points and their shadows from the images (rather than excluding the entire frame).

4.7 Conclusion

In this work, we presented our contribution to the construction of an intensity standardization framework for IVOCT images. We further contribute to the validation of two proposed schemes in the framework with data acquired by two of the most commonly used IVOCT systems in clinical research. Both local and global schemes are robust and produce accurate intensity matching. While local scheme performs marginally better than the global scheme, it requires a predefined histogram data set and is more time-consuming. Thus, for offline standardization of the images, the local scheme should be preferred for being more accurate. For online standardization or when another system is involved, the global scheme can be used as a simple and nearly-as-accurate alternative.

CHAPTER FIVE

QUALITY DIFFERENCE OF NEOINTIMA FOLLOWING THE IMPLANTATION OF BVS AND COCR-EES

Abstract — Quality of neointima after the implantation of everolimus–eluting bioresorbable scaffold (BVS) could be dissimilar to that of cobalt chromium everolimus-eluting scaffold (CoCr–EES). We aimed to quantitatively assess the neointimal quality after BVS implantation in comparison with CoCr–EES by optical frequency domain imaging (OFDI). This study is a post-hoc analysis of TROFI II randomized controlled trial focusing on the quantitative neointimal quality assessment 6-month after the implantation of BVS (N=82) and CoCr–EES (N=87) in ST elevation myocardial infarction (STEMI) patients. Neointimal light property analysis by OFDI full-automatically computed light attenuation, backscatter and light intensity for superficial and deep neointima separately. High light attenuation/backscatter and high light intensity are reportedly associated with lipidic change and tissue maturation, respectively. Superficial and deep neointima in BVS presented lower light attenuation than CoCr–EES (superficial: 0.77 ± 0.15 vs. 1.27 ± 0.55 mm^{-1}, $p<0.001$; deep: 0.88 ± 0.20 vs. 1.17 ± 0.27 mm^{-1}, $p<0.001$). Superficial neointima in BVS showed comparable backscatter to that of CoCr–EES (4.81 ± 0.52 vs. 4.94 ± 0.61, $p=0.141$), while deep neointima in BVS showed lower backscatter than that of CoCr–EES (4.60 ± 0.62 vs. 4.97 ± 0.62, $p<0.001$). Light intensity of superficial neointima was comparable between both arms (139 ± 13 vs. 144 ± 30, $p=0.236$), whereas light intensity of deep neointima in BVS was lower than CoCr–EES (129 ± 14 vs. 138 ± 21, $p<0.001$). The comparable light intensity and lower light attenuation/backscatter of the superficial neointima after BVS implantation than CoCr–EES implantation suggested that tissue maturation was comparable but lipidic change of neointima was less prominent after the BVS implantation.

This chapter is based a submitted manuscript: Y. Sotomi, Y. Onuma, **S. Liu**, et. al, **Quality Difference of Neointima Following the Implantation of Everolimus Eluting Bioresorbable Scaffold and Metallic Stent in Patients with ST Elevation Myocardial Infarction: Quantitative Assessments by Light Intensity, Light Attenuation, and Backscatter on Optical Coherence Tomography in TROFI II Trial**, *EuroIntervention*. 2018.

5.1 Introduction

Recent report from randomized trials and registry data evaluating everolimus-eluting Absorb bioresorbable vascular scaffold (Absorb BVS, Abbott Vascular, Santa Clara, CA) revealed relatively high incidence of early and late scaffold thrombosis [119, 120]. Physicians keep making every effort to understand the pathophysiological cause of scaffold thrombosis. Optical coherence tomography (OCT) assessments of scaffold thrombosis cases demonstrated that a peri-strut low intensity area (PSLIA) is one of the major imaging findings associated with scaffold thrombosis [121]. PSLIA is defined as homogenously appearing, nonsignal-attenuating zones around struts of lower intensity than the surrounding tissue, which might be correlated with vascular edema and vulnerability [122]. Although the direct relationship between this finding and scaffold thrombosis still remains unknown, the quality assessment of neointimal growth would be a key to get a better understanding of the underlying pathogenic mechanism of scaffold thrombosis.

Several studies reported the usefulness of OCT light intensity, light attenuation and light backscatter to characterize the tissue components of coronary artery. In a histological study, it was demonstrated that the increased light attenuation and light backscatter were associated with lipid-rich plaque and macrophages [27, 123]. Van Soest et al. reported that necrotic core and macrophage infiltration exhibit strong attenuation, while calcific and fibrous tissue have a lower light attenuation [28]. Nakano et al. evaluated 14 human stented coronaries with optical frequency domain imaging (OFDI) and demonstrated that light attenuation and light intensity were associated with morphological features of in-stent neointima [124]. Malle et al. reported the correlation of gray-scale signal intensity (light intensity) and maturation of the neointimal tissue [125]. Nakatani et al. demonstrated the association of light intensity with biointegration process of BVS in porcine models [58]. This supports the use of OCT light property analysis for the quantitative assessment of the tissue components.

It could be hypothesized that quality of neointima after the implantation of BVS would be dissimilar to that of metallic stents and the differential neointima could lead to differential clinical outcomes. In the present study, we evaluated the neointimal light intensity, light attenuation, and light backscatter on OCT as a surrogate of neointimal quality 6 months after the implantation of BVS in comparison with cobalt chromium everolimus-eluting scaffold (CoCr–EES) using dedicated software in patients with ST elevation myocardial infarction (STEMI) from the TROFI II randomized controlled trial [126].

5.2 Methods

5.2.1 Study design and population

The present study is a post-hoc substudy of TROFI II trial focusing on the quantitative neointimal quality assessment after the implantation of BVS and CoCr–EES. The TROFI II trial is a multicentre, international (8 centers in 4 countries), randomised, two-arm, single-blind, controlled trial performed in STEMI patients (clinicaltrial.org, NCT01986803). This is an investigator-initiated trial, sponsored by the European Cardiovascular Research Institute (ECRI). The details of protocol and main results of the trial have already been reported elsewhere [126]. Briefly, the study included patients presenting with STEMI. All patients were randomized 1:1 to one of the two treatment arms: BVS vs. CoCr–EES (Xience^{TM} Expedition stent, Abbott Vascular, Santa Clara, CA, USA). All centres had approval of their Medical Ethics Committee.

5.2.2 PCI procedure

Primary percutaneous coronary intervention (PCI) was performed according to standard practice [126, 127]. As per protocol, manual thrombectomy was mandatory to reduce thrombus burden. The decision to perform pre- or post-dilatation was left to the operator's discretion. If these techniques were performed, specific rules had to be followed during the procedure as well as for scaffold/stent sizing [128]. Scaffold implantation was carried out following current standards [128]. The other details were previously reported elsewhere [126]. It was recommended that patients received a loading dose of aspirin and a P2Y12 inhibitor pre-procedure, followed by dual antiplatelet therapy for at least 12 months. Optimal medical therapy was mandated in all patients [127].

5.2.3 Optical frequency domain imaging analysis

Angiographic and intracoronary imaging follow-up were conducted 6 months after the index procedure. OFDI assessment of the stented/scaffolded coronary segment was performed using the TERUMO Lunawave console and the FastView catheter. The off-line OFDI measurements were performed with the QIvus software (Medis, Leiden, The Netherlands) by the core laboratory (Cardialysis B.V., Rotterdam, the Netherlands). With adjustment for the pullback speed, the analysis of continuous cross-sections was performed at each 1-mm longitudinal interval within the treated segment. It was not possible to blind the analysts to the device type based on the characteristic appearance of BVS and CoCr–EES stent struts. Taking into account the difference in optical properties of cobalt chromium and polylactide, OFDI analysis was performed using comparative methods [129].

In the current post-hoc study, light property analysis was additionally performed to investigate the neointimal quality quantitatively by independent

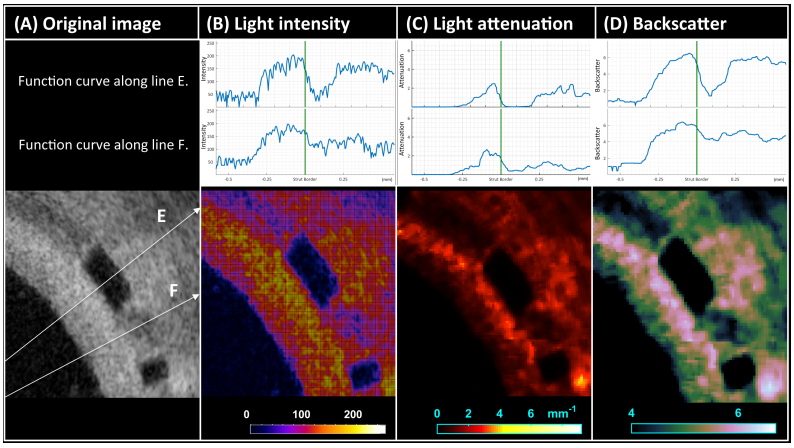

Figure 5.1: Neointimal area compartments analyzed by optical coherence tomography Raw image examples of OFDI at 6-month follow-up for BVS (**A**) and CoCr–EES (**B**) are presented. Lumen contour (**red**), endoluminal (**pink**) and abluminal (**green**) stent/scaffold contours were delineated semi-automatically by the core lab (**C** and **D**). Light property analysis was separately computed for the following the areas: 1) superficial neointima (purple area in panel **E** and **F**); 2) deep neointima (**blue** area in panel **E** and **F**); 3) entire neointima (**purple** and **blue** area in panel **E** and **F**).

investigators (YS, TA, YK, and RC). Dedicated software was employed for the quantitative light property analysis of vessel wall [QCU-CMS software version 4.69 (Leiden University Medical Center, Leiden, The Netherlands)]. The software was used to calculate the attenuation and backscattering coefficients based on a depth-resolved (DR) model [118]. The following parameters were analyzed within the neointimal area of interest defined with the contours delineated by the core laboratory (Cardialysis): 1) light intensity (no unit), 2) light attenuation (mm-1), and 3) backscatter (no unit).

Figure 5.2 illustrates the methodology and analysis example of OCT light property. The light intensity indicates the amount of light signal detected at a certain location in the vessel wall based on reflection and backscatter. The light attenuation, estimated as the DR attenuation coefficient in this study, indicates how fast the light signal is decayed. It is the rate of exponential decreasing intensity related to the light propagation depth. Concretely, the total incident light power I_0 is decreased to be I_0/e at depth $1/\mu_t$. The backscatter, estimated as the DR backscattering coefficient in this study, is related to the efficiency of tissue scattering the light backwards [118].

The neointimal area of interest was assessed separately as following three parts (Figure 5.1): 1) superficial neointima [delineated by the luminal contour

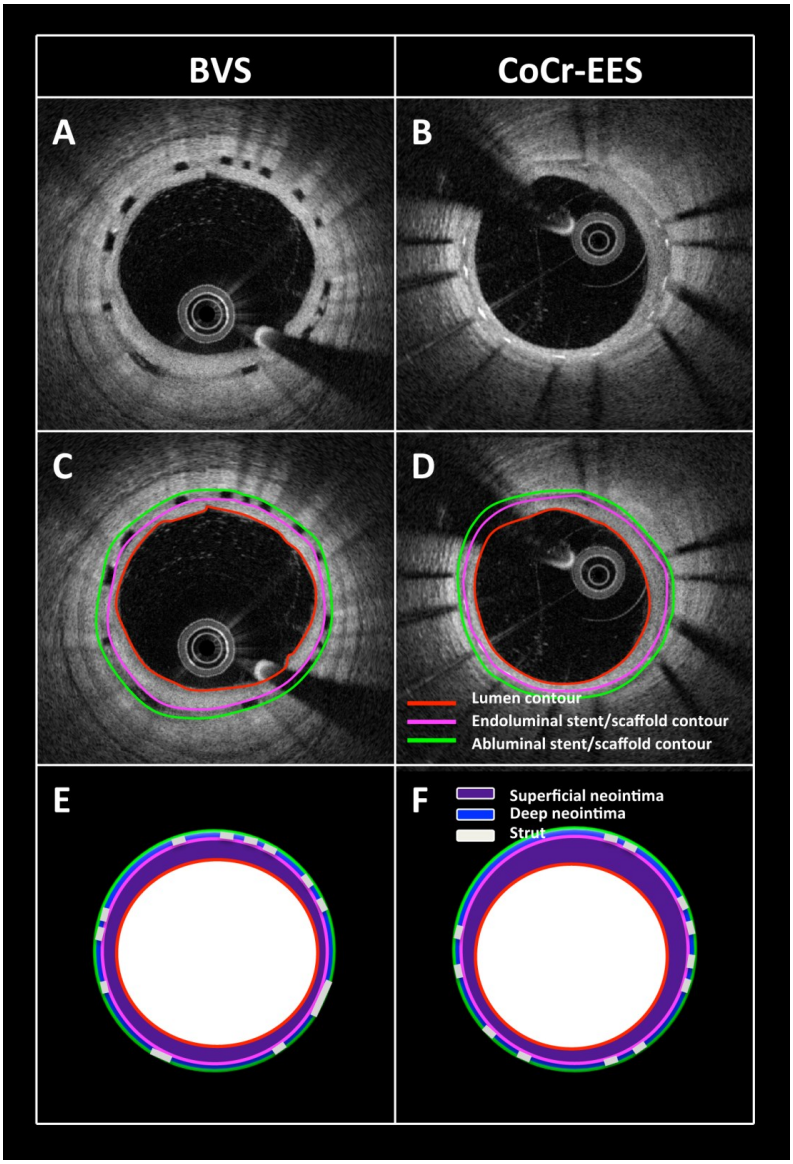

Figure 5.2: OCT image example of light intensity, light attenuation, and backscatter analyses. Image example of light property analysis is presented. The dedicated software full-automatically computed, based on the original image (**A**), three components of light property analysis 1) light intensity (**B**), 2) light attenuation (**C**) and 3) backscatter (**D**). Upper panels indicate the function curves of each parameter along the lines E and F. Lower panels show the color-coded images of each parameter.

and the interpolated contour connecting the endoluminal edges of struts (endoluminal stent/scaffold contour)], 2) deep neointima [delineated by the endoluminal and abluminal stent/scaffold contours, excluding strut area], and 3) entire (superficial AND deep) neointima. Each parameter was computed at every cross-section as an average and standard deviation (SD) in the area of interest. Mean value in each scaffold/stent lesion was calculated at a lesion level. The reproducibility of the neointimal analysis depends only on the contour delineation since the software is fully automatic. In the current study, the contour delineation was performed by the core lab, and its reproducibility was reported elsewhere [129].

5.2.4 Statistical analysis

Data are expressed as mean $\pm$ SD or median and inter-quartile range with differences [95% confidence interval]. Group means for continuous variables with normal and non-normal distributions were compared using Student's t-tests and Mann–Whitney U tests, respectively. Categorical variables were compared using the Pearson's chi-square test or Fischer's exact test, as appropriate. Mixed linear model with an assumed Gaussian distribution was used for the comparisons of continuous variables to take into an account the clustered nature of >1 scaffolds analyzed from the same patients, which might result in unknown correlations among measurements within the clusters. Statistical significance was assumed at a probability (p) value of <0.05. All statistical analyses were performed with SPSS (version 24.0.0, IBM, New York).

5.3 Result

5.3.1 Study subjects

A total of 191 patients were included in the trial and randomly assigned to undergo treatment with BVS (95 patients) or CoCr–EES (96 patients). Six months follow-up OCT data was available in 84 lesions in the BVS arm vs. 87 lesions in the CoCr–EES arm. Baseline demographics and procedural characteristics are previously reported and presented in Table 5.1 [126].

Medication at discharge and 6-month follow-up is summarized in Table 5.2. No differences were observed in the antiplatelet regimens and statin use between both arms. At 6-month follow-up, most of the patients were on dual antiplatelet regimen (aspirin + ticagrelor: 47.3% in BVS vs. 49.0% in CoCr–EES arm; $p = 0.82$; aspirin + prasugrel: 31.9% in BVS vs. 37.9% in CoCr–EES arm; $p = 0.39$). Statin was prescribed in 96% in the BVS arm and 93% in the CoCr–EES arm ($p = 0.40$).

5.3.1.1 OFDI analysis

Table 5.3 summarizes the OFDI results of neointimal assessments. The entire neointima area was comparable between both arms (BVS 1.26$\pm$0.38 mm^2 vs.

Table 5.1: Patient demographics and procedural characteristics

	BVS	CoCr-EES	Difference [95% CI]
Patient	N=95	N=96	
Male, n (%)	73 (76.8)	84 (87.5)	-10.7% [-21.4%, 0.1%]
Age, years	59.1±10.7	58.2±9.6	0.9 [-2.0, 3.8]
Current smoking, n (%)	46 (48.4)	47 (49.5)	-1.1% [-15.3%, 13.2%]
Previous smoking, n (%)	22 (23.2)	22 (23.2)	0.0% [-12.0%, 12.0%]
Diabetes mellitus, n (%)	18 (18.9)	14 (14.7)	4.2% [-6.4%, 14.8%]
Insulin dependent, n (%)	5 (5.3)	3 (3.2)	2.1% [-3.6%, 7.8%]
Non-insulin dependent, n (%)	13 (13.7)	11 (11.6)	2.1% [-7.3%, 11.5%]
Hypertension, n (%)	41 (44.1)	35 (36.5)	7.6% [-6.3%, 21.6%]
Hypercholesterolemia, n (%)	60 (63.8)	55 (57.3)	6.5% [-7.3%, 20.4%]
LDL cholesterol (mmol/L)*	3.1±0.8	3.1±1.2	-0.0 [-0.4, 0.3]
Chronic obstructive pulmonary disease, n (%)	3 (3.2)	3 (3.1)	0.0% [-4.9%, 5.0%]
Body mass index, kg/mm2	27.0±4.1	27.7±4.2	-0.7 [-1.9, 0.5]
Lesions	N=95	N=98	
Infarct related target lesions			
Right coronary artery, n (%)	44 (46.3)	44 (44.9)	1.4% [-12.6%, 15.5%]
Left anterior descending artery, n (%)	34 (35.8)	41 (41.8)	-6.0% [-19.8%, 7.7%]
Left circumflex artery, n (%)	17 (17.9)	13 (13.3)	4.6% [-5.6%, 14.9%]
Successful thrombectomy, n (%)	89 (81.1)	72 (73.5)	7.6 [-4.2, 19.4]
Mode of stenting			
Direct stenting, n (%)	42 (44.2)	48 (49.0)	-4.8 [-18.8, 9.3]
Pre-dilatation, n (%)	53 (55.8)	50 (51.0)	4.8 [-9.3, 18.8]
Grade of perfusion			
TIMI 0, n (%)	60 (63.2)	61 (62.9)	0.3% [213.4%, 13.9%]
TIMI 1. n (%)	3 (3.2)	3 (3.1)	0.1% [24.9%, 5.0%]
TIMI 2, n (%)	8 (8.4)	13 (13.4)	25.0% [213.8%, 3.8%]
TIMI 3, n (%)	24 (25.3)	20 (20.6)	4.6% [27.2%, 16.5%]
Device deployment			
Number of study devices	1.2±0.4	1.1±0.4	0.0 [-0.1, 0.2]
Nominal length of scaffold/stent	20.6±5.8	20.7±6.7	-0.1 [-1.8, 1.5]
Nominal diameter of scaffold/stent	3.25±0.30	3.12±0.37	0.13 [0.04, 0.22]
Maximum deployment pressure, atm	14.1±3.8	13.3±3.0	0.8 [-0.6, 2.1]
Post-dilatation performed, n (%)	48 (50.5)	25 (25.5)	25.0 [11.8, 38.3]
Use of non-compliant balloon, n (%)	43 (89.6)	13 (52.0)	37.6 [16.2, 59.0]
Diameter of postdilatation balloon, mm	3.51±0.34	3.29±0.62	0.22 [-0.01, 0.44]
Maximum pressure, atm	15.8±3.4	18.6±3.9	-2.9 [-4.6, -1.1]
Device success, n (%)	91 (95.8)	98 (100.0)	-4.2 [-8.2, -0.2]
Procedure success, n (%)	91 (95.8)	96 (100.0)	-4.2 [-8.2, -0.2]

Data are expressed as number (%) or mean ± standard deviation.
N refers to number of patients or lesions with data available. *BVS: N=69 vs. CoCr-EES: N=64.

CoCr–EES 1.27±0.54 mm^2, $p = 0.909$). Superficial and deep neointima were also similar between both arms. Mean strut area of BVS was significantly larger than

Table 5.2: Online Table 2. Medication at discharge and 6-month follow-up

	BVS	CoCr-EES	Difference [95% CI]	p value
Patient	N=95	N=96		
Medication at discharge				
Acetylsalicylic acid	100.0% (95/95)	99.0% (95/96)	1.0% [-1.0%, 3.1%]	1
Acetylsalicylic acid + Ticagrelor	54.7% (52/95)	55.2% (53/96)	-0.5% [-14.6%, 13.6%]	0.95
Acetylsalicylic acid + Prasugrel	30.5% (29/95)	40.0% (38/95)	-9.5% [-23.0%, 4.0%]	0.17
Other antiplatelet	10.9% (10/92)	3.2% (3/94)	7.7% [0.4%, 15.0%]	0.04
ACE inhibitor	57.9% (55/95)	56.8% (54/95)	1.1% [-13.0%, 15.1%]	0.88
Oral anticoagulation	0.0% (0/95)	2.1% (2/95)	-2.1% [-5.0%, 0.8%]	0.5
AT-II	5.3% (5/95)	10.5% (10/95)	-5.3% [-12.9%, 2.4%]	0.18
Beta Blocker	78.9% (75/95)	74.5% (70/94)	4.5% [-7.6%, 16.5%]	0.47
Statins	94.7% (90/95)	94.7% (90/95)	0.0% [-6.4%, 6.4%]	1
Atorvastatin	73.7% (70/95)	73.7% (70/95)	0.0% [-12.5%, 12.5%]	1
Rosuvastatin	11.6% (11/95)	10.5% (10/95)	1.1% [-7.9%, 10.0%]	0.82
Others	9.5% (9/95)	10.5% (10/95)	-1.1% [-9.6%, 7.5%]	0.81
Other lipid lowering drugs	6.3% (6/95)	2.1% (2/95)	4.2% [-1.5%, 9.9%]	0.28
Gastric protection drug	60.0% (57/95)	68.4% (65/95)	-8.4% [-22.0%, 5.2%]	0.23
Medication at 6 months				
Acetylsalicylic acid	98.9% (90/91)	96.9% (93/96)	2.0% [-2.1%, 6.1%]	0.62
Acetylsalicylic acid + Ticagrelor	47.3% (43/91)	49.0% (47/96)	-1.7% [-16.0%, 12.6%]	0.82
Acetylsalicylic acid + Prasugrel	31.9% (29/91)	37.9% (36/95)	-6.0% [-19.7%, 7.6%]	0.39
Other antiplatelet	2.2% (2/90)	5.2% (5/96)	-3.0% [-8.4%, 2.4%]	0.45
ACE inhibitor	54.9% (50/91)	53.7% (51/95)	1.3% [-13.1%, 15.6%]	0.86
Oral anticoagulation	1.1% (1/91)	3.2% (3/95)	-2.1% [-6.2%, 2.1%]	0.62
AT-II	6.6% (6/91)	16.8% (16/95)	-10.2% [-19.3%, -1.2%]	0.03
Beta Blocker	86.8% (79/91)	82.1% (78/95)	4.7% [-5.7%, 15.1%]	0.38
Statins	95.6% (86/90)	92.6% (88/95)	2.9% [-3.8%, 9.7%]	0.4
Atorvastatin	77.8% (70/90)	73.7% (70/95)	4.1% [-8.2%, 16.4%]	0.52
Rosuvastatin	7.8% (7/90)	11.6% (11/95)	-3.8% [-12.3%, 4.7%]	0.38
Other	10.0% (9/90)	7.4% (7/95)	2.6% [-5.5%, 10.8%]	0.52
Other lipid lowering drugs	7.7% (7/91)	0.0% (0/95)	7.7% [2.2%, 13.2%]	0.006
Gastric protection drug	59.3% (54/91)	58.9% (56/95)	0.4% [-13.7%, 14.5%]	0.96

Data are expressed as percentage (n/N).
N refers to number of patients or lesions with data available.

that of CoCr–EES (0.26 ± 0.04 mm^2 vs.0.08 ± 0.01 mm^2, $p < 0.001$).

The light property analysis (Table 5.3, Figure 5.3 and 5.4) was feasible in 82 lesions in the BVS arm vs. 87 lesions in the CoCr–EES arm, except for 2 lesions with incompatible data format. To facilitate the understanding of the three-parameter distribution (light attenuation, backscatter, and light intensity) in BVS and CoCr–EES, three-dimensional scatter plots were created (Figure 5.4). In the entire lesion level analysis (Table 5.3), superficial, deep and entire neointima on BVS struts presented lower light attenuation than CoCr–EES (superficial: 0.77 ± 0.15 vs. 1.27 ± 0.55 mm^{-1}, $p < 0.001$; deep:

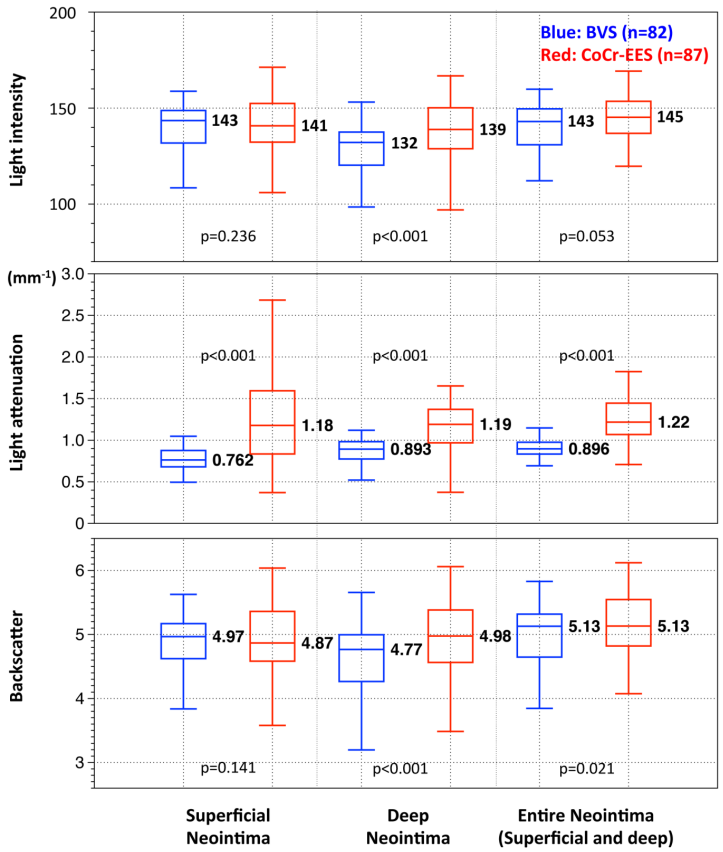

Figure 5.3: Neointimal quality assessment by light property analysis Neointimal quality was quantitatively assessed for BVS (**blue**) and CoCr–EES (**red**) by light property analysis including light attenuation (**upper panel**), backscatter (**middle panel**) and light intensity (**lower panel**). Neointimal area was separated into three parts: 1) superficial neointima, 2) deep neointima and 3) entire neointima (superficial and deep).

0.88±0.20 vs. 1.17±0.27 mm^{-1}, $p < 0.001$; entire: 0.91±0.17 vs. 1.24±0.28 mm^{-1}, $p < 0.001$). Superficial neointima on BVS struts showed comparable backscatter as compared to that of CoCr–EES (4.81±0.52 vs. 4.94±0.61, $p = 0.141$), while deep neointima of BVS showed lower backscatter than that of CoCr–EES (4.60±0.62 vs. 4.97±0.62, $p < 0.001$). Light intensity of superficial neointima was comparable between both arms (139±13 vs. 144±30, p=0.236), whereas light intensity of deep neointima were lower in the BVS arm than in the CoCr–EES arm (129±14 vs. 138±21, $p < 0.001$). SD of light attenuation and backscatter was higher in the CoCr–EES arm than in the BVS arm, while SD of

Table 5.3: Six-month quantitative neointimal assessments on OFDI

	BVS	CoCr-EES	Difference [95% CI]	p value
	N = 84	N = 87		
Mean neointimal area (superficial), mm^2	0.65±0.27	0.64±0.46	0.01 [-0.10, 0.13]	0.838
Mean neointimal area (deep), mm^2	0.61±0.15	0.64±0.12	-0.02 [-0.06, 0.02]	0.328
Mean neointimal area (entire), mm^2	1.26±0.38	1.27±0.54	-0.01 [-0.15, 0.13]	0.909
Mean strut area, mm2	0.26±0.04	0.08±0.01	0.18 [0.17, 0.19]	<0.001
Mean neointimal thickness, mm	0.11±0.03	0.09±0.05	0.02 [0.01, 0.03]	<0.001
Maximal neointimal thickness, mm	0.32±0.12	0.34±0.19	-0.01 [-0.06, 0.03]	0.56
Light property analysis	N=82	N=87		
Superficial neointima				
Light attenuation (mean), mm^{-1}	0.77±0.15	1.27±0.55	-0.50 [-0.63, -0.38]	<0.001
Light attenuation (SD), mm^{-1}	0.63±0.11	1.64±0.76	-1.01 [-1.18, -0.84]	<0.001
Backscatter (mean)	4.81±0.52	4.94±0.61	-0.13 [-0.30, 0.04]	0.141
Backscatter (SD)	1.06±0.11	1.15±0.13	-0.09 [-0.12, -0.05]	<0.001
Light intensity (mean)	139±13	144±30	-4 [-11, 3]	0.236
Light intensity (SD)	34±3	43±53	-9 [-21, 2]	0.112
Deep neointima				
Light attenuation (mean), mm^{-1}	0.88±0.20	1.17±0.27	-0.29 [-0.37, -0.22]	<0.001
Light attenuation (SD), mm^{-1}	0.79±0.14	1.14±0.23	-0.35 [-0.41, -0.29]	<0.001
Backscatter (mean)	4.60±0.62	4.97±0.62	-0.37 [-0.56, -0.18]	<0.001
Backscatter (SD)	1.43±0.19	1.35±0.22	0.09 [0.02, 0.15]	0.006
Light intensity (mean)	129±14	138±21	-10 [-15, -4]	<0.001
Light intensity (SD)	41±4	44±26	-3 [-8, 3]	0.366
Entire neointima (superficial and deep)				
Light attenuation (mean), mm^{-1}	0.91±0.17	1.24±0.28	-0.34 [-0.41, -0.26]	<0.001
Light attenuation (SD), mm^{-1}	0.76±0.13	1.40±0.31	-0.64 [-0.72, -0.57]	<0.001
Backscatter (mean)	4.97±0.50	5.15±0.52	-0.18 [-0.34, -0.03]	0.021
Backscatter (SD)	1.12±0.11	1.17±0.13	-0.05 [-0.09, -0.01]	0.009
Light intensity (mean)	140±12	146±24	-6 [-12, 0]	0.053
Light intensity (SD)	36±3	42±37	-7 [-15, 2]	0.112

Data are expressed as mean ± standard deviation (SD).
*CI: confidence interval

light intensity was comparable between both arms.

5.4 Discussion

Major findings of the present study can be summarized as follows: 1) In STEMI patients at 6-months follow-up, superficial and deep neointima on BVS presented lower light attenuation than that of CoCr–EES, suggesting more fibrotic and stable nature of the intima; 2) Superficial neointima on BVS showed comparable backscatter to that of CoCr–EES, while deep neointima in BVS showed lower backscatter than that of CoCr–EES; 3) Light intensity of superficial neointima

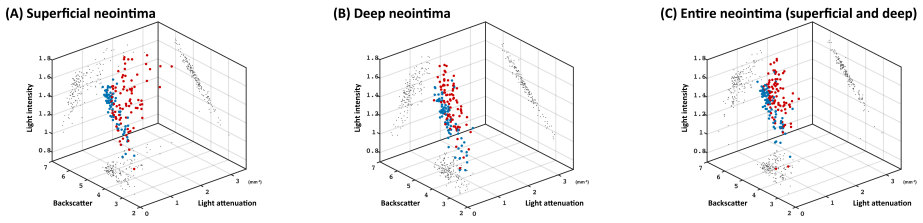

Figure 5.4: Three-dimensional plots of light intensity, light attenuation and backscatter. Light intensity, light attenuation and backscatter results for superficial neointima (**A**), deep neointima (**B**), and entire neointima (superficial and deep) (**C**) were illustrated in three-dimensional scatter plots for BVS (**blue plot**) and CoCr–EES (**red plot**).

was comparable between both arms, whereas light intensity of deep neointima was lower in the BVS arm than in the CoCr–EES arm; 4) SD of light attenuation and backscatter was higher in the CoCr–EES arm than in the BVS arm.

5.4.1 Head-to-head comparison of neointimal quality in previous publication

In the metallic stent era, a greater incidence of lipid-rich plaque was found in the drug eluting stent than in the bare metal stent in the early phase ($<$ 9 months after device implantation) [77]. After the advent of bioresorbable scaffold, OCT comparison of neointimal quality following implantation of BVS and CoCr–EES was performed in a post-hoc analysis of the pooled data from RESOLUTE and ABSORB Cohort B trials [130]. In that stable angina cohort, visual quality assessment of neointima after implantation of BVS and CoCr–EES demonstrated that there was a trend towards higher heterogenic tissue pattern of neointima (21.1% vs. 6.5%; $p = 0.12$) with CoCr–EES than with BVS [130]. However, the comparison of neointimal quality following polymeric scaffolds and metallic stents implantation has never been examined in the context of a randomized trial in STEMI population. The current study evaluated the neointimal quality in a quantitative and highly objective way and demonstrated a higher SD of light attenuation and backscatter of neointima following CoCr–EES implantation than following BVS implantation, which could represent a higher heterogeneity of the neointimal quality in the CoCr–EES arm. Although the current cohort was a STEMI population, which was different from the previously studied stable angina population, similar observations were made. Furthermore these observations are presented in a more comprehensive, quantitative and more objective manner than visual (qualitative) assessment used in the previous study.

5.4.2 Light property analysis

As previously reported, lipid-rich plaque, necrotic core and macrophage infiltration exhibit strong light attenuation and backscatter, while calcific and fibrous tissue have a lower light attenuation and backscatter [27, 123, 28]. Our group also validated our software with histology and demonstrated the similar relationship with tissue characteristics. 15 Light intensity is correlated with maturation of the neointimal tissue [125]. In animal and human autopsy specimens, mature neointimal tissue with a predominance of smooth muscle cells consistently showed higher gray-scale signal intensity values, whereas immature tissue with fiber-rich extracellular matrix, infrequent smooth muscle cells, interspersed inflammatory cells, macrophages and fibrin showed lower signal intensity values.

The present study shows comparable light intensity and higher light attenuation/backscatter of the superficial neointima of the CoCr–EES struts than that of the BVS struts. This could suggest that presence of the lipid components in the neointima (lipid plaque and form cell) might be more prominent after CoCr–EES than following BVS implantation in the early phase (6 months). On the other hand, deep neointima in BVS struts showed low light attenuation, low backscatter and low light intensity, which would be compatible with the feature of PSLIA. The PSLIA was considered as a representation of vascular edema, fibrin deposition, and plaque vulnerability. An animal study demonstrated a direct correlation between peri-strut inflammation and the degree of PSLIA at histology [131]. Based on the findings from Malle et al, the PSLIA can also be considered as immature tissue [125]. Although the incidence of PSLIA did not differ between both arms [98.8% (81/82) vs. 98.9% (86/87) in BVS vs. CoCr–EES, respectively (p=0.966)], the current quantitative results of the light property analysis suggest a more prominent inflammation, more frequent fiber-rich extracellular matrix with infrequent smooth muscle cells and more prominent fibrin deposition in the vicinity of BVS struts compared to CoCr–EES struts. This interpretation would also be supported by the report by Otsuka et al [132]. They reported in the porcine model that the mild to moderate inflammation was observed in BVS, which was greater as compared with CoCr–EES at 6 to 36 months. However, the superficial neointima on BVS, which is directly in contact with blood flow had comparable light intensity/backscatter and lower light attenuation property as compared to CoCr–EES. This finding might suggest that plaque can theoretically be shielded using BVS. Of note, since the current population comprised of STEMI patients, protruding necrotic core compartment and/or organized thrombus need to be taken into consideration as a neointimal component. Although the vessel condition (necrotic core and thrombus) should be the same in both BVS and CoCr–EES arms, difference footprint (BVS 27% vs. CoCr–EES 13%) could result in different amount of tissue protrusion [133]. In addition, the image characteristics of organized thrombus are not well understood or validated. Therefore, the abovementioned interpretation should be considered with caution. Further prospective serial imaging assessments with histological

approach and well-validated OCT methodology would be warranted to address the issue.

5.4.3 Clinical implication

The present study demonstrated the dissimilar property of neointima following the implantation of BVS and CoCr–EES. Nonetheless, the direct impact of the findings on clinical outcome still remains to be elucidated. Recent randomized trials comparing BVS vs. CoCr–EES in patients with stable coronary disease (ABSORB II and ABSORB Japan trials) demonstrated increased late clinical events (very late scaffold thrombosis) in the BVS arm, although the observation did not reach a statistical significance to detect a difference between the two devices. On the contrary, 2-year follow-up data in the current cohort of STEMI population demonstrated comparable late events (one case of very late scaffold/stent thrombosis in both arms) [134].

Both primary endpoint of the TROFI II trial (healing score) and the current results of light property analysis suggest more stable and less lipid neointima formation after BVS implantation, which appear to be supportive for the BVS usage in STEMI population. However, future trials powered for clinical endpoints are needed to assess risks and benefits of BVS use in STEMI patients.

5.4.4 Strength and limitations

The current study compared the neointimal quality after the implantation of BVS and CoCr–EES in a randomized trial using the dedicated full-automatic software. The novel neointimal assessment was quantitative and highly reproducible. Other possible confounding factors such as smoking and statin usage should be cancelled by randomization. However, some limitations need to be acknowledged. First, the study population included only STEMI patients. Caution should therefore be employed in extrapolating the present observations beyond the specific subset of STEMI patients, whose lesions and biologic responses may or may not be applicable to non-STEMI or stable coronary lesions. Second, the follow-up time of the present study was 6 months. Maturation of neointimal coverage might still be ongoing. Taniguchi et al. reported that the incidence of PSLIA of the CoCr–EES decreased from 1- to 2-year follow-up [135]. Third, since the baseline OCT images were not available in the TROFI II trial, plaque morphology pre-stent/scaffold implantation could not be assessed. Fourth, procedural difference between both arms (**Table 5.1**) could have partially impacted on the current results. Lastly, the light property can be affected by the residual blood or intraluminal mass. Although the core laboratory confirmed the sufficient quality of the OFDI images, it could confound the current results. Further serial assessments at long-term follow-up would be warranted.

5.5 Conclusion

OFDI comparison in STEMI patients at 6-month follow-up demonstrated the comparable light intensity and lower light attenuation/backscatter of the superficial neointima after BVS implantation than CoCr–EES implantation, suggesting that tissue maturation was comparable but lipidic change of neointima was less prominent after the BVS implantation. Clinical implications of the differential neointimal properties still remain to be investigated in future trials. A trial with clinically oriented endpoints would be warranted to investigate the risks and benefits of BVS in STEMI population.

5.5.1 Impact on daily practice

The present study demonstrated the dissimilar property of neointima following the implantation of BVS and CoCr–EES. Both primary endpoint of the TROFI II trial (healing score) and the current results of light property analysis suggest more stable and less lipid neointima formation after BVS implantation, which appear to be supportive for the BVS usage in STEMI population. However, future trials powered for clinical endpoints are needed to assess risks and benefits of BVS use in STEMI patients.

CHAPTER SIX

COMPARISON OF VISUAL ASSESSMENT AND COMPUTER IMAGE ANALYSIS OF INTRACORONARY THROMBUS TYPE BY OPTICAL COHERENCE TOMOGRAPHY IN CLINICAL PATIENTS

Abstract — Analysis of intracoronary thrombus type by optical coherence tomography (OCT) imaging is highly subjective. We aimed to compare a newly developed image analysis method to subjective visual classification of intracoronary thrombus type identified by OCT. Thirty patients with myocardial infarction and OCT imaging of the thrombotic culprit lesion were included. Thrombus type was evaluated by two independent readers. For comparison, the same OCT images were analyzed using QCU-CMS software. Two-observer consensus was considered to be the golden standard for the receiver operating curve (ROC) analyses. Repeatability of the computer-based measurements was good. By using a ROC, area under curve values for discrimination of white and red thrombi were examined. Results showed high values of under curve area in median attenuation, mean backscatter, mean grayscale intensity and 95^{th} percentile of attenuation/meidian grayscale intensity. The best cut-off values were identified to differentiate two types of thrombus. Repeatability of the novel computer-based analysis method was good. Attenuation, backscatter and grayscale intensity of thrombi in OCT images were found to differentiate red and white thrombi with high sensitivity and specificity. Measurement of these continuous parameters can be used as a less user-dependent method to characterize in vivo thrombi. The clinical significance of these new variables needs to be tested in further studies.

This chapter is based on a submitted manuscript: T. P. Kaivosoja, S. Liu, J. Dijkstra, H. Huhtala, T. Sheth and O.A. Kajander, **Comparison of Visual Assessment and Computer Image Analysis of Intracoronary Thrombus Type by Optical Coherence Tomography in Clinical Patients**, *Interventional Cardiology* , Under Review.

6.1 Introduction

Intracoronary thrombus is a frequent finding in patients with acute coronary syndromes undergoing invasive angiography and percutaneous coronary intervention (PCI). Research on the clinical significance of thrombus type is ongoing, and with more detailed understanding of the thrombotic process, the goal is to facilitate the development of tailored therapies for patients with acute coronary syndromes. Optical coherence tomography (OCT) is a high-resolution intravascular imaging technique with excellent contrast between the vessel lumen and intravascular structures [5]. In a consensus paper, the evidence level for image interpretation of intracoronary thrombus using OCT has been considered to be high [8]. The ability of OCT to produce images allowing differentiation between thrombus types has been validated against histology in post-mortem samples of human coronary arteries [101]. It is widely accepted in the OCT community that thrombi in OCT images can be classified as high-backscattering with a signal-free shadowing ('red', erythrocyte-rich) or low-backscattering ('white', thrombocyte-rich) [8]. This encourages further validation in clinical patients. However, valid analysis of different thrombus types *in vivo*by OCT is hindered by the high degree of subjectivity of measurement and the lack of validated methodology.

The aim of the present study is to develop a computer image analysis -based method for the assessment of thrombus morphology in OCT images that can be used for further *in vivo*validation. Computer algorithms determining backscatter, attenuation and intensity of the OCT signal are tested and compared to the present standard method, which is consensus classification of thrombus type by two independent analysts. Our hypothesis is that applying computer image analysis to assess thrombus type is feasible and can reduce observer variation in comparison to subjective evaluation.

6.2 Materials and Methods

6.2.1 Patients

The studied series included 30 patients enrolled in an OCT substudy of the TOTAL trial. The TOTAL trial was an international, multicentre, randomized trial of routine thrombectomy (using the Export catheter, Medtronic Cardiovascular, Santa Rosa, CA, USA) compared with PCI alone in STEMI patients treated with PCI (n = 10732) [136, 137]. A prospective OCT sub-study (n = 214) of TOTAL trial evaluated thrombus burden in patients with symptoms of myocardial ischaemia lasting for $\geq$ 30 min and definite electrocardiographic changes indicating STEMI who were referred for primary PCI and randomized within 12h of symptom onset [138]. Participation in the study required restoration of TIMI 2-3 flow after the first device. Patients were excluded from the OCT sub-study if they were in cardiogenic shock or had known renal failure. Informed consent was obtained from all individual participants included in the

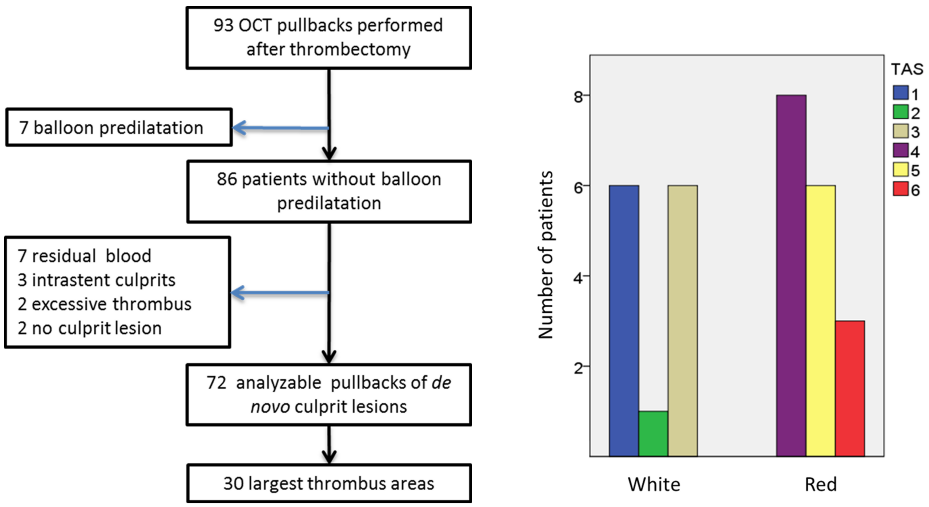

Figure 6.1: (a) Patient flow chart of the study. OCT = optical coherence tomography. (b) Qualitative thrombus classification. Consensus classification by two observers is shown. Thrombus attenuation score (TAS) from 1 to 3 equals white thrombus and from 4 to 6 red thrombus.

study. Of the patients in the OCT substudy who were randomized to thrombectomy, 72 had good quality OCT pullbacks available preceding balloon predilatation. Out of these, 30 patients with the largest maximal thrombus areas were selected for the present study (for detailed patient flow-chart, see Fig. 6.1a). All procedures performed in studies involving human participants were in accordance with the ethical standards of the institutional and/or national research committee and with the 1964 Helsinki declaration and its later amendments or comparable ethical standards. This article does not contain any studies with animals performed by any of the authors.

6.2.2 OCT Imaging

OCT imaging was performed using the Ilumien™ OCT system and C7 Dragonfly™ catheter (St Jude Medical, Minnesota, MN, USA). The radio-opaque distal marker of the OCT catheter was positioned 1-2 cm distal to the target lesion or stent and contrast was injected either manually or by automatic injector, according to local practice. Adequate image quality was checked and additional images were obtained, if the image quality was sub-optimal. OCT imaging raw data was exported in digital format for off-line analysis.

6.2.3 Optical coherence tomography image analysis

Data on thrombus cross-sectional areas at the culprit lesion was obtained from previous analysis [138]. For each patient, three OCT cross-sections with the largest thrombus areas were analyzed.

6.2.4 Visual assessment of thrombus type

Visual thrombus characteristics were evaluated by two independent readers (T.P.K. and O.A.K.) to assess the inter-observer reproducibility. One observer (T.P.K.) repeated the analysis after $>$ 4 week period to assess the intra-observer reproducibility. Thrombus was graded by a six-stage scale, where value 1 represents purely white thrombus and value 6 purely red thrombus, creating thrombus attenuation score (TAS). In accordance to published standards [5, 8], thrombus was considered white or mostly white, when the abluminal border of the thrombus or the vessel wall behind it could be seen. Conversely, the more the thrombus caused shadowing and poor visibility of the structures behind it, the redder it was scored. In addition, we applied only two additional rules. If a cross-section contained multiple fragments with different visual appearances, TAS was defined for the largest fragment. In the case of multiple same-sized thrombi, TAS was defined for the most strongly attenuating part of the thrombus.

6.2.5 Computer image analysis of thrombus

A special version of QCU-CMS version 4.69 software (Leiden University Medical Center, Leiden, The Netherlands) was used by two independent analysts. First, the thrombus areas were manually traced. The software then determined attenuation coefficient, backscatter term and grayscale intensity values for these areas and calculated several statistical parameters, including median, mean, standard deviation and 5^{th}, 10^{th}, 90^{th} and 95^{th} percentile values. Two patient cases with white and red thrombus showing the method are shown in Fig. 6.2. To avoid the inclusion of noise pixels and dark areas (low attenuation) at the abluminal side of the thrombus, we experimented with different minimum threshold values for attenuation. For the present analyses, attenuation was analyzed using both 0.15 mm^{-1} and 0.5 mm^{-1} threshold values.

The light attenuation coefficient and backscatter term have been determined based on a “depth-resolved” model [118]. The attenuation coefficient describes the total decreasing rate of light when it is traveling though the tissue. OCT images are generated by receiving the backscattered light. The backscatter coefficient describes the efficiency of tissue scattering light backwards. The backscatter term is estimated to be related to the backscatter coefficient. More information about the estimation can be referred to the technical paper [118]. The advantage of this method is its fast pixel-wise

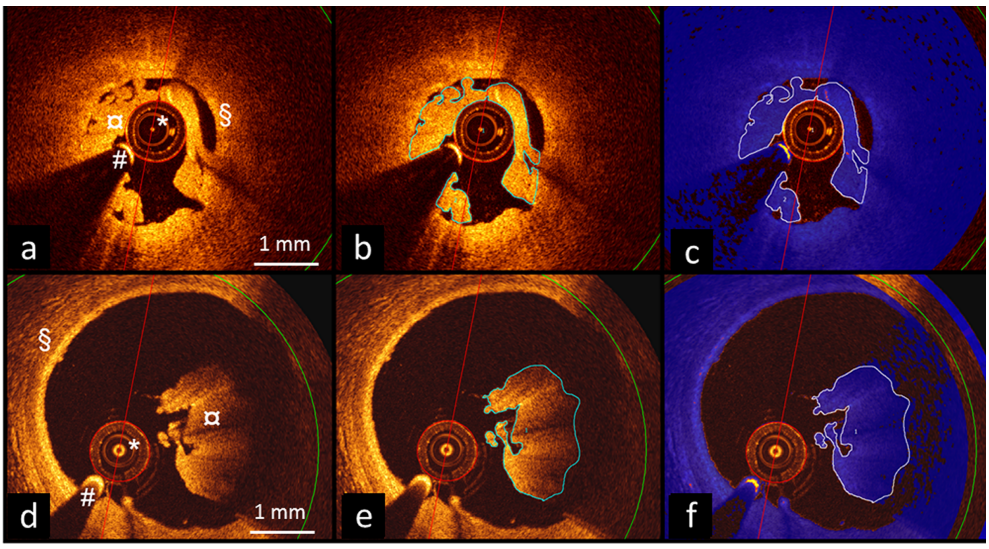

Figure 6.2: Examples of thrombus assessment by the QCU-CMS image analysis software in optical coherence tomography (OCT) image frames of two patients with **(a)** white and **(d)** red thrombus. **(b**, **e)** after manual tracing of the thrombi, **(c**, **f)** attenuation analysis was performed including regions with attenuation values above the designated threshold value (displayed in blue). Accurate segmentation of the luminal border of the thrombus and the contrast-filled flow area of the vessel can be seen in **(c)** and **(f)**. *) OCT catheter, #) guidewire artefact, ☼) thrombus, §) vessel wall.

estimation, which requires no predefined delineation and is more flexible for post analysis.

For each patient, a weighted average of each statistical parameter was calculated using the pixel count in each traced thrombus area. To study inter-observer reproducibility, two readers analyzed the same OCT cross-sections of 10 randomly selected patients independently. For intra-observer comparison, one observer repeated the analyses on these 10 patients after a 4-week period. For the repeated assessments, OCT raw data was re-imported into the QCU-CMS software. Then the thrombus areas were manually re-traced in the same transversal frames.

6.2.6 Statistical analysis

Bland–Altman (B-A) analysis was used to estimate the bias resulting from inter- and intra-observer variation [139]. In the analysis, the mean values of observer 1 and 2 were plotted against the difference of measurements between the observers. The 95% limits of agreement (equal to ± 1.96 SD) were determined for the variables. Mean relative difference for each variable was

defined as the mean absolute difference divided by mean of observers 1 and 2. Inter- and intraobserver reliability of thrombus classification was assessed using the kappa statistic (κ). Receiver-operating characteristic (ROC) curve analyses were performed to determine the best cutoff values (using highest Youden Index) of QCU-CMS parameters for discriminating red and white thrombi and the areas under the curve (AUCs), as well as the sensitivities and specificities of the diagnostic test. Statistical analyses were performed with the Stata Statistical software: Release 13 (StataCorp, College Station, TX, USA) and the IBM SPSS 21 Statistics software (IBM, Armonk, NY, USA).

6.3 Results

Baseline patient characteristics are shown in Table 6.1.

Table 6.1: Baseline patient characteristics (n = 30)

Age	57±10.1
Male sex	22 (73.3)
Risk factor profile	
Hypertension	14 (46.6)
Diabetes	4 (13.3)
Current smoking	8 (26.7)
Obesity (BMI $\geq$ 30)	14 (46.7)
Prior MI	2 (6.7)
Prior PCI	1 (3.3)
Creatinine, μmol/L	82.0 $\pm$ 16.6
Antithrombotic treatment	
Upfront glycoprotein inhibitor IIb/IIIa use	11 (36.7)
UFH prior to procedure	22 (73.3)
Enoxaparin prior to procedure	2 (6.7)
Bivalirudin prior to procedure	0 (0.0)
Culprit vessel	
RCA	16 (53.3)
LAD	12 (40.0)
LCx	2 (6.7)
TIMI flow (prior to thrombectomy)	
0	15 (50.0)
1	4 (13.3)
2	3 (10.0)
3	8 (26.7)
TIMI thrombus class (prior to thrombectomy)	
$<$ 3	4 (13.3)
$\geq$ 3	26 (86.7)

Values are mean $\pm$ SD for continuous variables and n (%) for categorical variables. BMI = body mass index, LAD = left anterior descending coronary artery, LCx = left circumflex coronary artery, MI = myocardial infarction, PCI = percutaneous coronary intervention, RCA = right coronary artery, SD = standard deviation, UFH = unfractionated heparin

6.3.1 Qualitative thrombus classification by two observers

For the purpose of statistical comparison of the thrombus assessment methods, a six-stage scale consensus TAS was used to form a binary classification, where scores 1-3 equaled white and 4-6 red thrombus. There were 13 cases classified as white and 17 as red thrombus (see Fig. 6.1b for details). Kappa values for binary classification of the thrombi were 0.74 and 0.53, respectively, for inter- and intraobserver comparisons.

Table 6.2: Interobserver variability of QCU-CMS measurements

Parameters	Observer 1 Mean (SD)	Observer 2 Mean (SD)	Range	Mean Difference confidence interval	%	Limits of agreement
Attenuation (mm^{-1})						
Median	0.61 (0.12)	0.57 (0.13)	0.35 – 0.77	0.03 (-0.02 – 0.08)	5.8	-0.11 – 0.17
Mean	0.72 (0.09)	0.69 (0.11)	0.49 – 0.83	0.03 (-0.02 – 0.08)	4.3	-0.10 – 0.16
SD	0.42 (0.09)	0.42 (0.07)	0.32 – 0.54	0.001 (-0.02 – 0.02)	0.2	-0.07 – 0.07
Skewness	1.36 (0.50)	1.46 (0.40)	0.89 – 2.18	-0.10 (-0.26 – 0.06)	-7.2	-0.55 – 0.19
Kurtosis	3.01 (2.42)	3.72 (2.45)	0.55 – 7.21	-0.72 (-2.21 – 0.78)	-21.4	-4.90 – 3.47
P_5	0.26 (0.06)	0.23 (0.06)	0.17 – 0.38	0.02 (-0.01 – 0.04)	8.6	-0.04 – 0.08
P_{10}	0.30 (0.07)	0.28 (0.07)	0.19 – 0.46	0.02 (-0.01 – 0.05)	8.3	-0.06 – 0.11
P_{90}	1.27 (0.16)	1.24 (0.17)	1.00 – 1.53	0.03 (-0.03 – 0.09)	2.3	-0.14 – 0.20
P_{95}	1.51 (0.20)	1.48 (0.19)	1.21 – 1.77	0.03 (-0.04 – 0.10)	1.9	-0.17 – 0.23
Backscatter						
Median	5.18 (0.22)	5.09 (0.28)	4.77 – 5.49	0.10 (-0.01 – 0.20)	1.9	-0.20 – 0.40
Mean	5.19 (0.18)	5.10 (0.23)	4.79 – 5.46	0.10 (0.01 – 0.18)	1.8	-0.15 – 0.34
SD	0.61 (0.09)	0.66 (0.07)	0.47 – 0.72	-0.04 (-0.07 - -0.02)	-6.9	-0.10 – 0.01
Skewness	-0.08 (0.29)	-0.22 (0.44)	-0.74 – 0.31	0.15 (-0.05 – 0.34)	96.7	-0.39 – 0.68
Kurtosis	-0.13 (0.49)	0.44 (1.24)	-0.70 – 2.37	-0.57 (-1.16 – 0.02)	-183	-2.22 – 1.08
P_5	4.22 (0.26)	4.07 (0.26)	3.77 -4.70	0.15 (0.05 – 0.24)	3.5	-0.11 – 0.41
P_{10}	4.41 (0.25)	4.28 (0.28)	3.95 – 4.93	0.13 (0.04 – 0.21)	2.9	-0.12 – 0.37
P_{90}	5.99 (0.16)	5.94 (0.18)	5.65 -6.26	0.05 (-0.02 – 0.11)	0.8	-0.14 – 0.23
P_{95}	6.17 (0.16)	6.13 (0.17)	5.85 – 6.41	0.04 (-0.02 – 0.10)	0.7	-0.14 – 0.21
Grayscale						
Median	67.19 (32.99)	63.86 (35.43)	28.16 – 147.83	3.32 (-2.53 – 9.19)	5.1	-13.05 – 19.71
Mean	104.65 (26.87)	100.04 (31.37)	69.76 – 166.69	4.61 (-2.28 – 11.49)	4.5	-14.64 – 23.85
SD	106.03 (17.46)	103.02 (15.95)	80.03 – 134.78	3.02 (-3.78 – 9.81)	2.9	-15.98 – 22.01
Skewness	2.51 (0.88)	2.65 (0.72)	1.72 – 3.99	-0.14 (-0.41 – 0.14)	-5.3	-0.91 – 0.63
Kurtosis	12.49 (11.67)	14.62 (10.83)	4.31 – 38.17	-2.13 (-6.88 -2.62)	-15.7	-15.40 – 11.14
P_5	16.59 (13.34)	14.74 (11.59)	6.66 – 48.92	1.85 (0.08 – 3.61)	11.8	-3.10 – 6.79
P_{10}	21.77 (16.88)	20.14 (16.17)	8.83 – 65.09	1.63 (-0.02 – 3.27)	7.8	-2.97 – 6.22
P_{90}	239.64 (40.18)	230.74 (48.77)	166.58 – 312.48	8.90 (-4.40 – 22.20)	3.8	-28.28 – 46.09
P_{95}	315.19 (44.98)	305.05 (53.64)	228.63 – 408.65	10.15 (-6.64 – 26.94)	3.3	-36.78 – 57.08

CI = confidence interval, SD = standard deviation, P_i = i^{th} percentile. N = 10

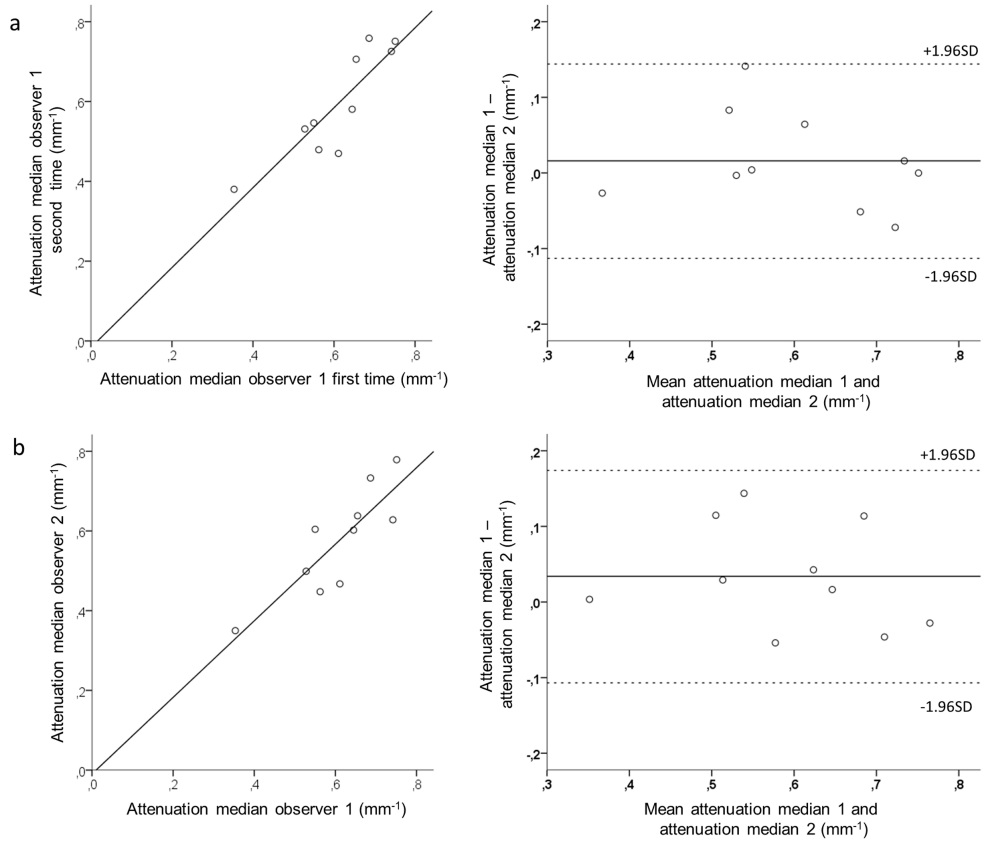

Figure 6.3: Intra- and interobserver variability of measurement of thrombus attenuation in optical coherence tomography (OCT) images using image analysis software. (Right) Scatterplot and Bland-Altman plot of **(a)** intraobserver and **(b)** interobserver comparison for median attenuation. SD, standard deviation.

6.3.2 Reproducibility of quantitative measurements using QCU-CMS software

Results presented in Tables 2 and 3 show inter- and intraobserver variability of measurements in thrombus regions. Mean differences for most statistical parameters of thrombus attenuation, backscatter and grayscale intensity were small, with narrow limits of agreement between observers. For all tested parameters, intraobserver variability was slightly smaller than interobserver variation. Limits of agreement for skewness and kurtosis of attenuation, backscatter and grayscale intensity were wider than for the other statistical parameters. B-A plot of median attenuation is shown in Fig. 6.3. B-A plots of mean backscatter and mean grayscale intensity, respectively, are shown in Figs. 6.4 and 6.5.

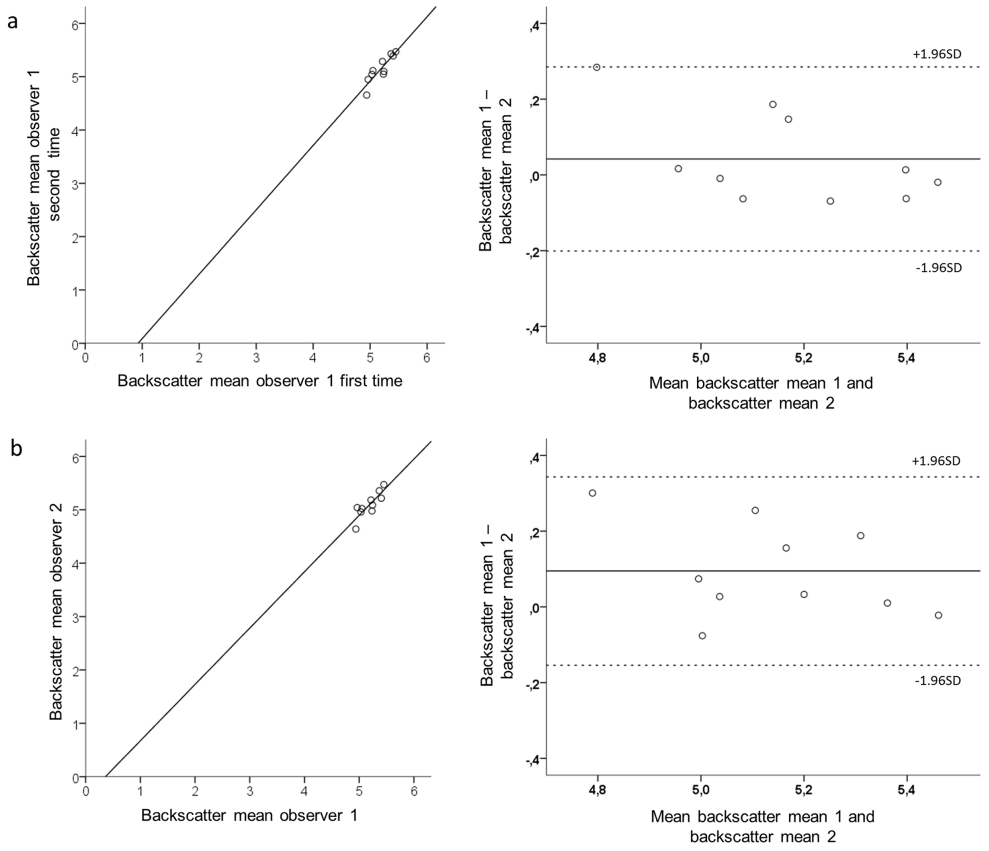

Figure 6.4: Intra- and interobserver variability of measurement of thrombus backscatter in optical coherence tomography (OCT) images using image analysis software. Scatterplot and Bland-Altman plot of **(a)** intraobserver and **(b)** interobserver comparison for mean backscatter. SD, standard deviation.

6.3.3 Comparison of visual TAS and measurements by QCU-CMS software

There was an inverse relationship between several QCU-CMS parameters of attenuation, backscatter and grayscale intensity and the visual TAS. Distribution of selected statistical parameters of attenuation, backscatter and grayscale intensity in the six-stage TAS (Fig. 6.6) and two-stage TAS (Fig. 6.7) are shown. In these analyses, a minimum threshold 0.15 mm^{-1} was used for attenuation.

The same thrombus cross-sectional areas were analyzed using a higher minimum threshold (0.5 mm^{-1}) for attenuation. This resulted in exclusion of an average of 36% (minimum 5.3%, maximum 69.8%) of the pixels of each patient previously included with the 0.15 mm^{-1} threshold. In this analysis, only low

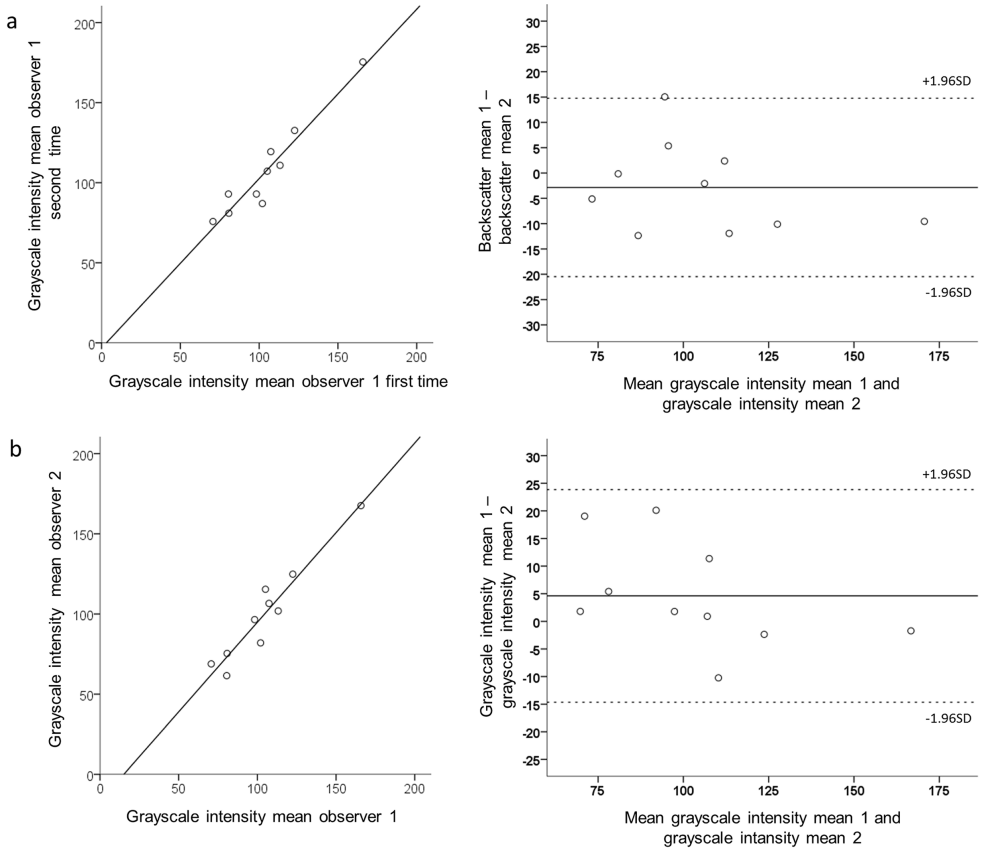

Figure 6.5: Intra- and interobserver variability of measurement of thrombus grayscale intensity in optical coherence tomography (OCT) images using image analysis software. Scatterplot and Bland-Altman plot of **(a)** intraobserver and **(b)** interobserver comparison for mean grayscale intensity. SD, standard deviation.

percentiles of attenuation values had an inverse relationship with visual TAS. Median or high percentiles of attenuation values were not related to TAS (Online Fig. 6.8).

In addition, using ratio of attenuation and intensity measurements, a new 'normalized' variable was constructed. The ratio of 95th percentile of attenuation and median intensity had a direct relationship with TAS (Online Fig. 6.9).

Table 6.3: Intraobserver variability of QCU-CMS measurements

Parameters	Observe 1 Mean (SD) first time	second time	Range	Mean Difference confidence interval	%	Limits of agreement
Attenuation (mm^{-1})						
Median	0.61 (0.12)	0.59 (0.13)	0.37 – 0.75	0.02 (-0.03 – 0.06)	3.3	-0.11 – 0.14
Mean	0.72 (0.09)	0.70 (0.11)	0.51 – 0.84	0.02 (-0.02 – 0.06)	2.8	-0.10 – 0.13
SD	0.42 (0.09)	0.41 (0.08)	0.31 – 0.54	0.001 (-0.01 – 0.02)	0.2	-0.04 – 0.05
Skewness	1.36 (0.50)	1.41 (0.43)	0.75 – 2.14	-0.05 (-0.24 – 0.14)	-3.6	-0.58 – 0.48
Kurtosis	3.01 (2.42)	3.64 (2.81)	0.52 – 6.99	-0.64 (-2.48 – 1.21)	-19.2	-5.79 – 4.52
P_5	0.26 (0.06)	0.25 (0.06)	0.18 – 0.39	0.01 (-0.01 – 0.02)	3.9	-0.03 – 0.05
P_{10}	0.30 (0.07)	0.29 (0.07)	0.20 – 0.45	0.01 (-0.01 – 0.03)	3.4	-0.05 – 0.06
P_{90}	1.27 (0.16)	1.25 (0.17)	1.02 – 1.54	0.02 (-0.03 – 0.07)	1.6	-0.12 – 0.16
P_{95}	1.51 (0.20)	1.48 (0.21)	1.23 – 1.79	0.03 (-0.03 – 0.08)	2.0	-0.13 – 0.18
Backscatter						
Median	5.18 (0.22)	5.13 (0.29)	4.78 – 5.47	0.05 (-0.06 – 0.16)	1.0	-0.25 – 0.35
Mean	5.19 (0.18)	5.14 (0.25)	4.80 – 5.46	0.04 (0.05 – 0.13)	0.8	-0.20 – 0.29
SD	0.61 (0.09)	0.62 (0.09)	0.43 – 0.69	-0.01 (-0.03 - -0.01)	-1.6	-0.06 – 0.04
Skewness	-0.08 (0.29)	-0.10 (0.31)	-0.47 – 0.29	0.02 (-0.10 – 0.14)	-22.2	-0.32 – 0.36
Kurtosis	-0.13 (0.49)	0.02 (0.56)	-0.76 – 0.86	-0.15 (-0.44 – 0.13)	-136	-0.94 – 0.64
P_5	4.22 (0.26)	4.16 (0.32)	3.78 -4.77	0.05 (-0.04 – 0.14)	1.2	-0.19 – 0.29
P_{10}	4.41 (0.25)	4.36 (0.31)	3.96 – 4.94	0.05 (-0.05 – 0.14)	1.1	-0.21 – 0.30
P_{90}	5.99 (0.16)	5.96 (0.19)	5.66 -6.27	0.03 (-0.03 – 0.09)	0.5	-0.13 – 0.19
P_{95}	6.17 (0.16)	6.14 (0.18)	5.86 – 6.43	0.03 (-0.02 – 0.08)	0.5	-0.12 – 0.32
Grayscale						
Median	67.19 (32.99)	70.05 (36.06)	30.67 – 151.52	-2.86 (-8.00 – 2.28)	-4.2	-17.23 – 11.51
Mean	104.65 (26.87)	107.50 (29.72)	73.22 – 170.61	-2.85 (-9.16 – 3.45)	-1.3	-20.48 – 14.77
SD	106.03 (17.46)	107.19 (13.59)	91.86 – 136.54	-1.16 (-7.88 – 5.56)	-1.1	-19.95 – 17.64
Skewness	2.51 (0.88)	107.19 (13.59)	91.86 – 136.54	-1.16 (-7.88 – 5.56)	-1.1	-19.95 – 17.64
Kurtosis	12.49 (11.67)	12.84 (10.82)	3.81 – 38.65	-0.35 (-5.00 -4.30)	-2.8	-13.35 – 12.65
P_5	16.59 (13.34)	17.19 (14.43)	7.17 – 54.29	-0.60 (-1.97 – 0.76)	-3.6	-4.41 – 3.21
P_{10}	21.77 (16.88)	22.96 (18.30)	9.50 – 69.53	-1.20 (-2.97 – 0.58)	-5.4	-6.15 – 3.76
P_{90}	239.64 (40.18)	244.76 (38.86)	195.65 – 319.26	-5.12 (-19.99 – 9.75)	-2.1	-46.69 – 36.46
P_{95}	315.19 (44.98)	320.95 (41.95)	273.50 – 414.96	-5.76 (-24.41 – 12.90)	-1.8	-57.91 – 46.39

CI = confidence interval, SD = standard deviation, P_i = i^{th} percentile. N = 10

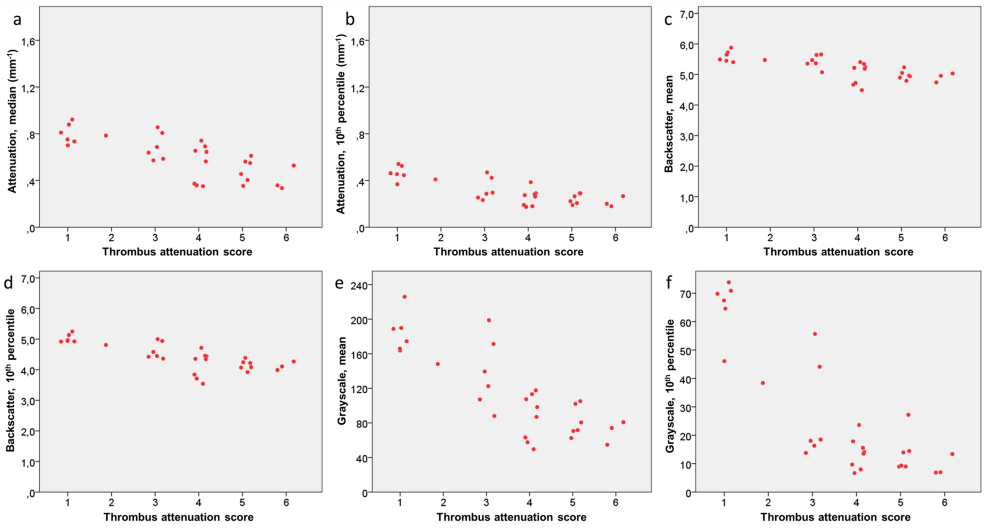

Figure 6.6: Relationship of thrombus attenuation score and parameters measured by image analysis software in thrombus areas in optical coherence tomography (OCT) images. Scatterplots for **(a)** median attenuation, **(b)** 10^{th} percentile of attenuation, **(c)** mean backscatter, **(d)** 10^{th} percentile of backscatter, **(e)** mean grayscale intensity and **(f)** 10^{th} percentile of grayscale intensity.

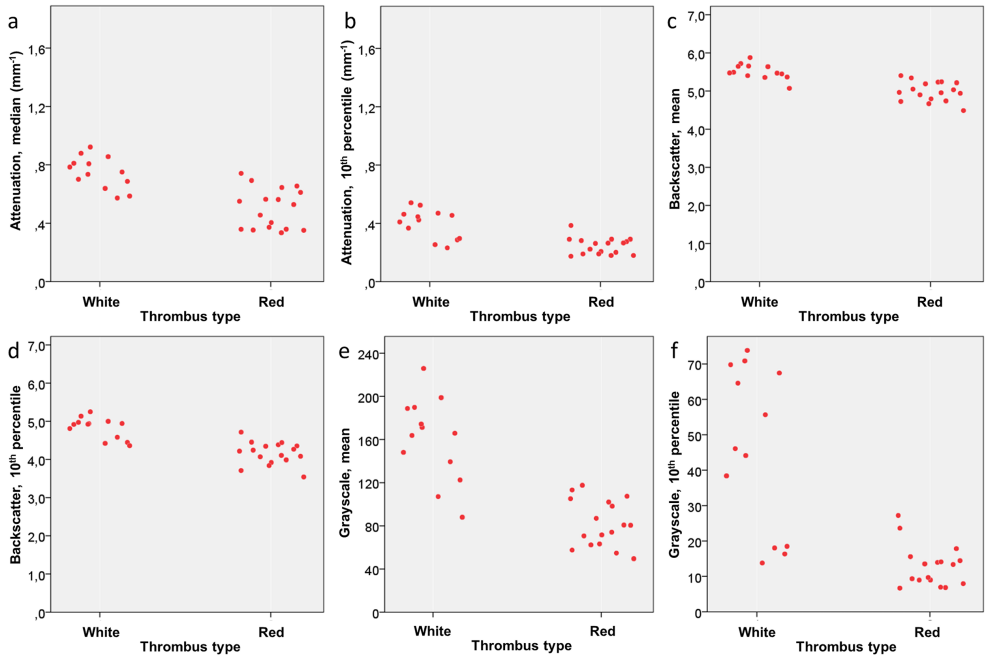

Figure 6.7: Relationship of binary thrombus type and parameters measured by image analysis software in thrombus areas in optical coherence tomography (OCT) images. Scatterplots for **(a)** median attenuation, **(b)** 10^{th} percentile of attenuation, **(c)** mean backscatter, **(d)** 10^{th} percentile of backscatter, **(e)** mean grayscale intensity and **(f)** 10^{th} percentile of grayscale intensity.

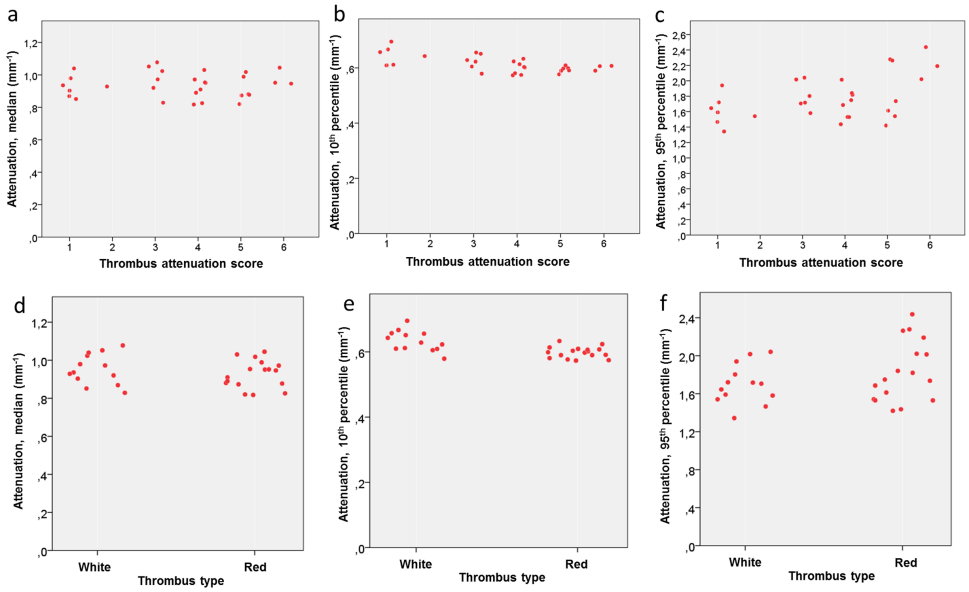

Figure 6.8: Relationship of thrombus type and parameters measured by image analysis software in thrombus areas in optical coherence tomography (OCT) images using a higher (0.5) threshold for minimal attenuation. Scatterplots for **(a)**, **(e)** median attenuation, **(b)**, **(d)** 10^{th} percentile of attenuation, **(c)**, **(e)** 95^{th} percentile of attenuation.

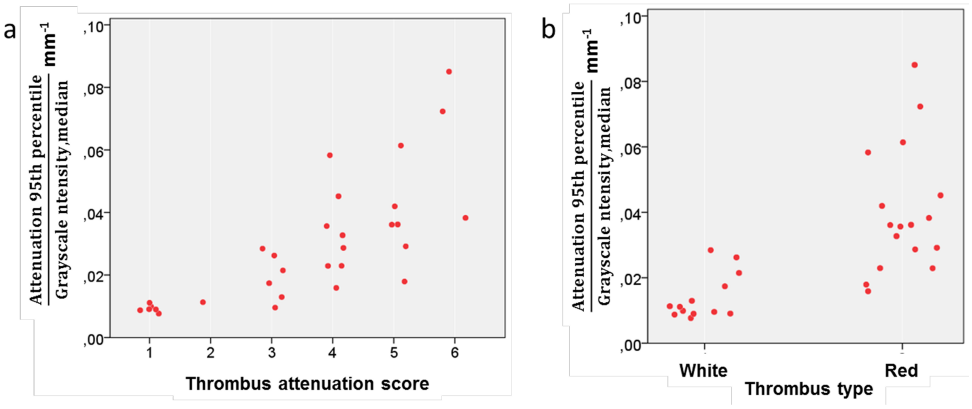

Figure 6.9: Relationship of thrombus type and the ratio of 95th percentile of attenuation and median grayscale intensity. **(a)** thrombus attenuation score and **(b)** binary thrombus type.

Table 6.4: Results of receiver operating characteristic (ROC) curve analysis of values determined by QCU-CMS software in prediction of thrombus type (white vs. red)

	Attenuation (mm^{-1})					Backscatter					Grayscale				
	AUC	95%CI	Sens	Spec	CP	AUC	95%CI	Sens	Spec	CP	AUC	95%CI	Sens	Spec	CP
Med.	0.919	0.83-1.00	100	71	0.568	0.946	0.87-1.00	92	88	5.33	0.941	0.86-1.00	100	77	57.11
Mean	0.896	0.78-1.00	85	82	0.753	0.959	0.89-1.00	92	94	5.35	0.959	0.89-1.00	85	100	120.1
P_5	0.896	0.78-1.00	85	88	0.246	0.946	0.87-1.00	92	82	4.19	0.928	0.84-1.00	92	82	12.03
P_{10}	0.891	0.77-1.00	77	94	0.294	0.955	0.89-1.00	100	77	4.36	0.937	0.85-1.00	92	82	15.95
P_{90}	0.679	0.48-0.87	46	88	1.384	0.801	0.63-0.97	62	100	6.20	0.941	0.84-1.00	92	94	261.6
P_{95}	0.584	0.38-0.79	100	24	1.222	0.710	0.51-0.91	62	88	6.33	0.900	0.78-1.00	92	82	337.6
SD	0.624	0.42-0.83	85	18	0.322	0.837	0.67-1.00	15	77	0.694	0.756	0.58-0.94	69	77	106.7
Skew.	0.186	0.02-0.35	85	12	0.778	0.072	0.00-0.17	62	6	-0.417	0.081	0.00-0.18	8	53	2.72
Kurt.	0.312	0.11-0.52	85	12	0.849	0.882	0.76-1.00	69	100	0.110	0.100	0.00-0.23	8	82	14.86

attenuation/Med. intensity (mm^{-1})	AUC	95%CI	Sens	Spec	CP
P_{95}	0.950	0.88-1.00	88	85	0.022

AUC = area under curve, Sens = sensitivity (%), Spec = specificity (%), SD = standard deviation,
P_i = i^{th} percentile, CP = cut-off point defined by the largest value of J (Youden) index.

6.3.4 ROC analysis

A ROC curve analysis was applied to assess the best parameters to distinguish between different types of thrombus. The AUCs represented the ability of QCU-CMS software parameters to differentiate red and white thrombi (Table 4). The best cutoff values to diagnose red thrombus in each class of variables were <5.35 for mean backscatter (AUC = 0.959, sensitivity 92%, specificity 94%), <120.1 for mean grayscale intensity (AUC = 0.959, sensitivity 85%, specificity 100%), <0.57 mm^{-1} for median attenuation (AUC = 0.919, sensitivity 100%, specificity 71%) and > 0.022 mm^{-1} for 95^{th} percentile of attenuation/median grayscale intensity (AUC = 0.950, sensitivity 88%, specificity 85%) (Fig. 6.10).

AUCs for different statistical variables of attenuation measurements from the second analysis using a higher 0.5 mm^{-1} threshold were low (in range of 0.50-0.60) except for 5^{th} percentile and 10^{th} percentile of attenuation (AUCs 0.878 and 0.851, respectively).

6.4 Discussion

As a first step in order to resolve the clinical significance and predictive potential of OCT-based thrombus analysis in clinical patients, a robust method to translate the traditional visual classification into reproducibly measured variables is needed. Validated methodology to assess different thrombus types by OCT imaging has not been available, and previously published data has relied on subjective analysis methods based on observers' visual perception of the thrombus type [140, 141]. In this methodological study, we measured attenuation, backscatter and grayscale intensity of *in vivo*thrombi using newly developed image analysis software features. For methodological validation, we assessed repeatability of the measurements and the correlation between traditional visual thrombus classification and the computer software-based analysis. We were able to demonstrate for the first time the use of image analysis software to assess *in vivo*thrombi in OCT images. Measurements of attenuation, backscatter and grayscale intensity of the thrombi using the software were highly repeatable and there was good agreement between two observer consensus visual evaluation of thrombus type and several parameters measured using the software on the OCT images.

Visual assessment of thrombus type in OCT images is *per se* highly observer-dependent. There is not much previous data on the repeatability of the operator-based assessment of thrombus type and there is also a lack of standardized definitions and cut-off values differentiating red and white thrombus. We observed that the visual classification, as expected, was only moderately reproducible. Of note, the present analysis was performed off-line by experienced analysts and reproducibility outside the OCT core lab setting is most probably even lower. In the present study, we showed that computer-based image analysis of *in vivo*thrombus can be performed with good repeatability. The OCT-derived mean and 10^{th} percentile backscatter and mean grayscale

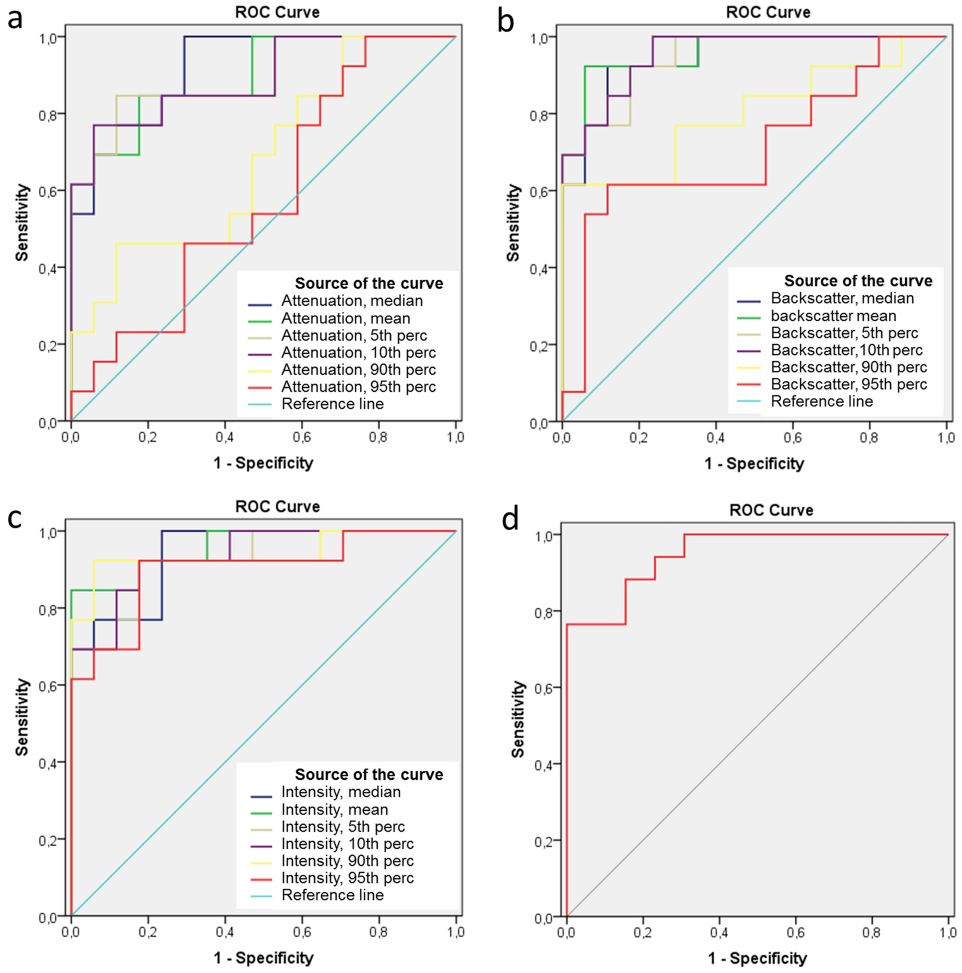

Figure 6.10: Receiver operating characteristic (ROC) curves of parameters determined by QCU-CMS software in prediction of thrombus type (white vs. red). Different statistical parameters of **(a)** attenuation, **(b)** backscatter, **(c)** grayscale intensity and **(d)** the ratio of 95th percentile of attenuation and median grayscale intensity. Perc = percentile.

intensity values and the ratio of 95th percentile of attenuation to median grayscale intensity had excellent performance (AUC $>$ 0.95) in discriminating red from white thrombus. In addition, median values of attenuation, backscatter and grayscale intensity, low percentile values of the same variables and high percentile values of grayscale intensity all had good performance (AUC $>$ 0.90).

Earlier histopathological studies of aspirated coronary thrombi have provided important insight to the composition of the thrombus [142, 143].

Specimens retrieved by aspiration devices, however, do not necessarily represent the whole thrombotic burden in a patient with STEMI. Some of the thrombotic material stays attached to the vessel wall and may differ from the aspirate. Further, the structure of thrombus is easily distorted and the material fragmented during aspiration. A thorough analysis of aspirated thrombus fragments would be highly laborious and as such subject to a variety of sources of error. The three-dimensional structure of the *in vivo*thrombus is lost and the co-localization of thrombus and the culprit lesion is not possible. The ability of intravascular OCT to provide high-resolution images of thrombus *in vivo*during angiography and PCI procedures [144] makes it a robust tool to study thrombus. A further advantage of OCT imaging in comparison to histological analysis of thrombus aspirate is that the images are available for intraoperative decision-making. Considering the frequent occurrence of thrombus in OCT imaging of clinical patients, especially in case of acute coronary syndromes, the data on thrombus image analysis is surprisingly scarce. In a single cadaver series, OCT light attenuation characteristics have been validated against histology to classify thrombi as red or white. When the authors applied a cut-off value defined in that study, OCT had good sensitivity and specificity for differentiating red and white thrombi. [101] In addition to a case report [145] the method has not been used successively.

The goal of analyzing thrombus type *in vivo*and gaining insight to the pathogenesis of acute myocardial infarction is to facilitate the development of novel therapies and to tailor the intervention for each patient. There is some evidence that aspirates consisting mainly of white thrombus might be predictive of lower mortality after the infarction [146]. Presence of older thrombus in even 40% of thrombus aspirates of acute STEMI patients in a large series [147] supports the concept that the acute closure of the culprit artery is preceded by days or weeks of thrombotic process. Interestingly, histological signs of older thrombus have been associated with higher mortality after the myocardial infarction [16]. In addition, red thrombus in the aspirate has been suggested to associate with more frequent angiographically visible distal embolization [148]. Development of reliable image analysis methodology is essential to enable investigation of thrombus types *in vivo*. In the future, development of smaller size imaging catheters may reduce the need for routine thrombus aspiration prior to OCT imaging of highly thrombotic lesions, such as those in STEMI patients.

In a recent *in vitro*study, the correlation between red blood cell concentration and attenuation or backscatter of the OCT signal was shown to have a limit, above which the correlation was not seen [149]. In our series of *in vivo*OCT imaging, we did not observe any saturation threshold level for these variables. A feasible explanation for this might be that the red blood cell concentration achieved in an experimental model is higher than in thrombus *in vivo*, which contains other components as well. Unexpectedly, in the present study we were not able to demonstrate a higher actual attenuation in red than white thrombus using the software algorithm Instead, there was an inverse relationship between attenuation values and red thrombus, including high

percentiles of attenuation. Even after setting a higher threshold for minimum attenuation, which removed all 'dark' areas in the abluminal side of the thrombus when strong signal attenuation was present, a positive correlation was not observed. This seems to be due to high heterogeneity of analyzed thrombus regions. In red thrombi, there are highly attenuating parts, but these are also observed in the white thrombus.

We tested different parameters measured by the software from the thrombus images. Attenuation is a parameter, which describes the relative decrease in the light intensity per distance travelled in the tissue. This is different from backscatter and grayscale intensity, which both describe the absolute values of light properties. In the present series, we observed that grayscale intensity performed as well as attenuation in differentiating thrombus types. There were also no differences in observer variation between attenuation and grayscale intensity parameters. An explanation for this finding may be the high technical quality of the patient subset selected for the analysis. In presence of more blood speckle i.e. residual artefactual blood in the image frames, attenuation is expected to be a more stable parameter. On the other hand, intraluminal thrombus is in most occasions located very proximally to the imaging catheter. This may render thrombus analysis less vulnerable to artefacts, such as small quantities of artefactual blood in the OCT recording.

The tested image analysis methodology relies on automatic measurement of attenuation and backscatter along the A-lines of the OCT image. The analysis is not automatic, and user-dependent interaction is needed, because the software does not integrate global information of the cross-section, considering artefacts and thrombus-like structures. Although it would be possible to use image analysis algorithms to determine most of the borders of thrombus cross-sections, in most cases some manual correction would be needed, especially for the red thrombus where no abluminal border is visible. For that reason and to simplify the testing of observer variation, in this study we decided to use manual tracing of the thrombus cross-sections. In addition, we applied a minimum threshold value for attenuation, which excludes noise pixels and dark regions accidentally included in the regions of interest. By using this threshold, we also aimed at avoiding inclusion of non-informative pixels in the abluminal side of the thrombus, where OCT signal has attenuated to a minimum. For further development of the methodology, it can be possible to aim for a semi-automatic analysis method, starting from delineation of intraluminal space followed by automatic detection of luminal border of the thrombus with necessary manual corrections.

6.4.1 Limitations

The current study has a number of important limitations. First, the thrombus regions were manually delineated. To reduce user-dependence, we applied a minimal threshold value to attenuation, which effectively delineated the endoluminal border of the thrombus. The abluminal border of the thrombus area, especially in the case of red thrombi was, however, partly dependent on

manual tracing.

Second, since this was an in vivo study including clinical patients, no histological golden standard could be applied to the ROC curve analyses. This prevents us from establishing a direct correlation between the software-derived parameters and biological thrombus contents. The basic principle of increased light attenuation by increased red blood cell content of the thrombus has, however, been validated earlier [101].

Third, the current study was not designed to assess the real-world reproducibility, but was limited to a relatively small sample of selected cases. We focused on improving the reproducibility of thrombus type analysis by the use of computer-based methodology. More data is needed in order to evaluate the true absolute reproducibility.

6.5 Conclusions

Subjective thrombus type assessment in OCT images can be complemented by less user-dependent computer-based image analysis methodology. Computer-based measurement of attenuation, backscatter and grayscale intensity of thrombi is repeatable and can be used to differentiate red and white thrombi with high sensitivity and specificity. This study stimulates further studies with larger sample size to confirm the results and their clinical value.

CHAPTER SEVEN

SUMMARY AND DISCUSSION

7.1 Summary

The aim of this thesis was to develop a software pipeline for tissue analysis in IVOCT by systematically addressing different open questions for analysis.The absolute intensities of comparable tissue regions in IVOCT images were speculated to be affected by the position of the catheter due to a difference in light loss caused by two factors, the traveling distance in the flush medium and the incident angle of light entering the arterial wall. This has been inferred mainly based on empirical evidence in combination with specialized tissue optics knowledge [34] and the studies of other catheter based imaging modalities such as IVUS. In Chapter 2, we report on a first attempt to quantify the correlation between the position of the catheter with respect to the luminal wall and the image intensities. Statistical analysis based on a hierarchical linear model showed that both factors affect image intensities within a superficial tissue layer significantly with $p < 0.001$, as either aspect increases, the intensity tends to decrease. A potential compensation was suggested and application experiments shown its potential for enhancing the visualization and BVS struts detection with the signal levels being balanced circumferentially. Visual assessment showed that attenuated structures were enhanced when the catheter was eccentric and the blood was poorly flushed. BVS detection for 6 out of 8 pullbacks was improved by 1 to 6.6 percent in F-score. On the other hand, the generalization of the algorithm was limited due to the fact that it is using an estimated intercept which is pullback-dependent.

Since the attenuation coefficient represents the decreasing trend of signals without involving an intercept term, it is less dependent on the catheter position and other related parameters. In the remaining work, our attention is focused on the estimation of this optical property. Until recently, region-based curve-fitting approaches have been predominantly used for attenuation calculation. As a pixel-based estimation, using the Depth-Resolved (DR) model has the advantage of being less dependent on local homogeneity and preserving original resolution. We implemented the DR-model for IVOCT images in Chapter 3. In addition to the attenuation coefficient, we further extended the model to estimate a backscatter term, and proposed an algorithm to exclude the noisy region at the end of the A-lines. For the first time, it was implemented in IVOCT images with fast and robust calculations. We analyzed the attenuation

coefficient, backscatter term and the image intensity in regions of interest (ROIs), which were delineated referring to corresponding histopathology. The optical values in the ROIs were reported and their distributions were further compared with 2-sample t-test to evaluate the potential for distinguishing six types of tissues. Results show that the IVOCT intensity, DR attenuation coefficient and backscatter term extracted with the reported implementation are complementary to each other in characterizing six tissue types: mixed, calcification, fibrous, lipid-rich, macrophages and necrotic core.

During the implementation of the DR model, we encountered unstandardized intensity ranges which resulted in different estimations even with the same approach. This is because different vendors follow different ways to store the data, which are unknown. Since 16-bit data yields values in comparable range with the published numbers, we applied a looked-up table to convert the 8-bit Terumo data into a 16-bit St. Jude like range for calculation in Chapter 3. This approach has been later improved using an exact histogram specification technique presented in Chapter 4. IVOCT pullbacks were matched according to visual landmarks, and the matching error was analyzed at both histogram and local intensity level. Two schemes, one global one local, for the determination of target histogram were compared. The leave-one-out validation shows that dissimilarities between the two pullbacks matched by the two schemes are comparable across the entire validation data set. Despite the errors caused by empirical matching, catheter position and histogram-based technique, the total matching difference was shown to be relative small. For the first time, this issue has been addressed with purely *in vivo* images rather than experimental data acquired with physical laboratory settings. The proposed matching framework can be further adopted for the intensity standardization across other OCT systems or other multi-slice imaging modalities where the intensity's order is maintained.

For the application of the DR algorithm, the optical parameters were analyzed as features for the maturity of post-stenting neointima in Chapter 5. The three factors DR attenuation, backscatter term and image intensity were determined in the neointima of both superficial and deep layers with fixed thickness. Comparison of the neointima in BVS struts with that in CoCr-EES strut showed a lower attenuation coefficient in both the superficial and the deep layer. The backscatter term and image intensity term in superficial neointima were comparable in the superficial layer but lower in the deep neointima. In general, the maturation was comparable while the change of lipid content in neointima was less prominent in BVS strut stents.

For the differentiation between thrombus types analyzed in Chapter 6, the three values were analyzed within consensus delineated regions of thrombi. Results showed two types of thrombi can be well differentiated using regional statistical values with high area under curve values. The determination is highly reproducible, less objective with minimum user-dependency. This warrants further investigation in larger randomized trials.

7.2 Discussion

The image intensity, the estimated attenuation coefficient and the backscatter term were considered in each study throughout the thesis. We have observed certain complimentary contributions of these three factors when comparing regional statistical analysis in Chapter 3. Meanwhile, we observed that the backscatter term tends to balance the intensity level circumferentially along the lumen, but how it adds to tissue characterization is yet not clear. Although the backscatter term is strongly related to the attenuation term by design, results show that it gives additional information for the differentiation of tissue types. Therefore, all three features are recommended to be calculated in studies such that they can be analyzed in meta-analysis in the future. Among these three parameters, the influence of estimated attenuation is most distinguishable and perceivable. From an image processing viewpoint, the estimation of DR attenuation can also be considered as normalization of intensities at a certain pixel position with the summation of intensities behind it. Structures can be enhanced when shadows occur due to high attenuation or reflection. Therefore, the estimated attenuation coefficient can potentially enhance the detection of structures including superficial dense macrophage infiltrations, TCFAs, red thrombi and metal stents.

Indication of macrophage infiltration: In Chapter 3, the carpet view of attenuation coefficient (Fig. 13) shows groups of regions of high values with dark shadows (Fig. 15). Their histology counterparts at four sites indicate that these regions may be associated with dense macrophage infiltrations and warrant further research. As it has been discussed in the work from Phipps et al. [61], that there are two types of macrophages; M1 macrophages that engulf lipid particles and form the necrotic core while M2 macrophage are more densely constructed with high reflection and serves for anti-inflammatory purposes. They also argued that only those macrophages that engulf lipid particles cause dark shadows. The analyzed superficial macrophages in Chapter 3 present both dark shadows and much higher attenuation coefficient than any other tissue types. That may suggest the presence of both types of macrophages: the carpet view of attenuation coefficients can be a promising auxiliary tool to validate the aforementioned subtype macrophages.

Detection of IVOCT-TCFAs: Acute coronary syndromes (ACSs) have been confirmed to be highly associated with TCFAs, which is defined in histology anatomy as a thin fibrous cap ($<65\mu$m) on top of a large lipid pool. In IVOCT it appears as a signal rich layer followed by a signal poor region separated with a diffused border in between. In the meanwhile, some other structures can be misread as TCFAs [8], such as the tangential signal dropout artifact, dramatic signal loss due to intraluminal thrombus and residual blood, or the aforementioned superficial macrophage infiltration. We refer to all structures looking like TCFA in IVOCT image as IVOCT-TCFAs. The detection of IVOCT-TCFAs should be considered as

a next step. The largest obstacle is the generalization of ground truth. The quality of IVOCT is restricted by its high noise level, and requirement of flushing and operator expertise. TCFA classifiers require large scale of training and validation *in vivo* data. It is highly challenging to acquire corresponding histological confirmation for ground truth. Therefore, the ground-truth generated in IVOCT images can be disturbed by the aforementioned artifacts. A suggestion is to generate a ground truth of IVOCT-TCFAs. The catheter position, attenuation of residuals in the lumen, and the attenuation of the cap can be analyzed as post-processing to refine the detection. The cap thickness should be measured with validated algorithm and reported as an important population property.

Detection of IVOCT thrombus: Encouraged by outcome of the work in Chapter 6, automated thrombus detection may be helpful for both further validation with larger data sets and clinical application in the future. In CAD patients, thrombi are associated with the erosion or rupture of the endothelium. To determine the backside border of a red thrombus, the algorithm proposed in Chapter 3 should be used. A challenge for thrombus detection can be the lumen border detection for embolic white thrombus and red thrombus of moderate size. In the former case, the lumen border can be difficult to distinguish due to the fact that the circumferential thrombus is closely attached to lumen border. In the latter case, the lumen border is invisible due to the high light loss. Both cases can cause an abrupt decrease of lumen radius in the longitudinal view of a pullback. Therefore, the continuity of lumen size in longitudinal view can be used as auxiliary information for lumen border determination. Thrombi detection and classification can also contribute to a detailed evaluation of iatrogenic damage during PCI and a better therapeutic treatment.

From the viewpoint of feature analysis, results indicate that the proposed pipeline can enhance the differentiation of tissue types using traditional machine learning classification. Traditional classifiers meet an upper boundary of performance once the size of training data is above a certain scale, while the prediction accuracy of a deep learning network can approximate to one as the size of training data continues to grow [150]. An interesting question is whether the estimated optical terms can benefit the detection of deep learning classifiers. However, this requires well-labeled training data, which is a well-known bottleneck in introducing deep nets to new imaging modalities such as IVOCT. Using the proposed pipeline as a preprocessing step can reduce the irrelevant variations for tissue recognition. In the meanwhile, the calculation of local DR attenuation involves the regularization of summation intensities behind a specific pixel position, thus the estimated value is location dependent. This type of information usually cannot effectively be learned even by deep networks. Therefore, using the proposed pipeline as preprocessing is expected to speed up the training convergence and increase the prediction accuracy for the same amount of data.

7.3 Future work

This work aimed to look into tissue recognition based on image data. We aimed to develop an analysis pipeline that can be ultimately used directly with data acquired in the catheterization laboratory without additional measurements. We extensively analyzed the variation range of measured values that can be caused by catheter dependent parameters such as focal point and incident angle. However, we did not include solid experimental control groups for concrete accuracy analysis. The validation of estimated attenuation coefficient and backscatter terms with phantom data can be found in the literature [59, 64]. For the intensity standardization framework, validation with data acquired from phantoms or ophthalmology data can be interesting for the future work since it allows for more control of the image alignment. However, it remains challenging to analyze the matching effect caused by the difference in catheter position, the pressure and strain on the vessel wall during cardiac cycle, etc. The effect can be monitored using high-speed OCT and electrocardiography (ECG) gating. Currently developed systems can acquire 100-mm-vessel within one second [151], which allows for imaging a long coronary segment within one cardiac cycle. Acquiring images at the same cardiac phase can minimize the cardiac motion differences. Another interesting attempt can be, if technically possible, building an inter-vendor system to combine catheters from two vendors as one such that images can be acquired at the same time, thus the concern over image alignment can be avoided.

As the algorithms for deep learning are becoming more efficient, it may hold promise for IVOCT image analysis in the future. A general structure can be constructed for stent struts detection to tackle the broad range of designs of stent. Using deep learning for intensity standardization can hopefully contend with the local variation better with higher performance than the proposed histogram-based technique, and it requires no maintained intensity order. A generative adversarial network would allow for the generation of artificial images. This is even more promising when combined with multimodal imaging. IVOCT has the shortcoming of limited imaging depth, thus it cannot offer information of plaque size and vessel remodeling. This information can be augmented by IVUS. Combining IVOCT with IVUS would preserve the advantages of both modalities at the expense of imaging speed. More existing techniques include near-infrared reflection spectroscopy (NIRS), near-infrared fluorescence (NIRF), and fluorescence lifetime imaging (FLIm) [16]. Since these techniques do not provide depth information, these techniques have been combined with IVUS or OCT catheters to offer direct information of tissue compositions per A-line. The intravascular photoacoustic (IVPA) imaging detects similar tissue components as those aforementioned techniques but with structural information at resolution of IVUS. Multimodal imaging allows for perfect inter-modality matching. Since images are acquired simultaneously, it allows for performing data alignment regardless the cardiac cycle. Once they are well validated, it is expected that the acquired images can evolve into *in vivo* alternatives for histological data for generating large random ground-truth

for training tissue classifiers. Given an image from one modality, it is then possible to predict its counterparts from other modalities. This can be further used to perfect the functionality of IVOCT and also possible to speed up the validation work of new techniques in the future.

Samenvatting

Het doel van dit proefschrift was om een software pijplijn te ontwikkelen voor de weefsel analyse in IVOCT beelden door systematisch een aantal open vragen met betrekking tot de analyse te behandelen. Er werd gespeculeerd dat de absolute intensiteiten van vergelijkbare weefselgebieden in IVOCT-beelden worden beïnvloed door de positie van de katheter met als gevolg een verschil in lichtverlies veroorzaakt door twee factoren: de afgelegde afstand in het spoelmedium en de invalshoek van het licht dat de vaatwand binnengaat. Dit is voornamelijk afgeleid uit empirisch bewijs in combinatie met specialistische kennis van de optische eigenschappen van weefsel [34] en de studies van andere op katheter gebaseerde beeldvormende modaliteiten zoals IVUS. In Hoofdstuk 2 rapporteren we over een eerste poging om de correlatie tussen de positie van de katheter ten opzichte van de vaatwand en de beeldintensiteiten te kwantificeren. Statistische analyse gebaseerd op een hiërarchisch lineair model toonde aan dat beide factoren significant de beeldintensiteit in een weefsel laag net onder de oppervlakte beïnvloeden met $p < 0.001$. Naarmate beide aspecten toenemen, heeft de intensiteit de neiging om af te nemen. Een mogelijke compensatie methode werd gesuggereerd en experimenten toonden hun potentie voor het verbeteren van de visualisatie en verbeterde BVS-strut detectie waarbij de signaalniveaus rondom het vat beter in balans waren. Visuele beoordeling liet zien dat uitgedoofde structuren werden versterkt wanneer de katheter excentrisch was en het bloed slecht was weggespoeld. De BVS detectie voor 6 van de 8 pullbacks werd verbeterd met 1 tot 6.6 procent in F-score. Aan de andere kant was de generalisatie van het algoritme beperkt vanwege het feit dat het een geschatte interceptie gebruikt die pullback-afhankelijk is.

Aangezien de uitdovingscoëfficiënt de afnemende trend van signalen representeert zonder een interceptieterm te gebruiken, is deze minder afhankelijk van de katheterpositie en andere gerelateerde parameters. In het resterende werk is daarom onze aandacht gericht op de schatting van deze optische eigenschap. Tot voor kort werden voornamelijk op gebied gebaseerde curve-fitting benaderingen gebruikt voor de uitdovingsberekening. Als een op pixels gebaseerde schatting heeft het gebruik van het Depth-Resolved (DR)-model het voordeel dat het minder afhankelijk is van lokale homogeniteit en de originele resolutie behoudt. We hebben het DR-model voor IVOCT-afbeeldingen in hoofdstuk 3 geïmplementeerd. Naast de

uitdovingscoëfficiënt hebben we het model verder uitgebreid om een terugverstrooiing term te schatten en hebben we een algoritme voorgesteld om het gebied met ruis aan het einde van de A-lijnen uit te sluiten. Het is de eerste keer dat dit algoritme is geïmplementeerd voor IVOCT-afbeeldingen met snelle en robuuste berekeningen. We analyseerden de uitdovingscoëfficiënt, terugverstrooiing term en de beeldintensiteit in gebieden van interesse (ROI's). Deze waren ingetekend op basis van overeenkomstige histopathologie beelden. De optische waarden in de ROI's werden gerapporteerd en hun distributies werden vergeleken met de 2-zijdige t-test om de mogelijkheid te onderzoeken om zes verschillende soorten weefsels te onderscheiden. De resultaten tonen aan dat de IVOCT-intensiteit, de DR-uitdovingscoëfficiënt en de terugverstrooiing term, berekend met de beschreven software, complementair zijn aan elkaar bij het karakteriseren van de zes weefseltypes: gemengd, verkalkt, vezelig, vetrijk, macrofagen en necrotische kern.

Tijdens de implementatie van het DR-model kwamen we niet-gestandaardiseerde intensiteit bereiken tegen die resulteerden in verschillende schattingen, zelfs met dezelfde aanpak. Dit komt omdat verschillende leveranciers van IVOCT apparatuur verschillende manieren gebruiken om de gegevens op te slaan die onbekend zijn. Omdat data in 16-bits, waarden opleveren die vergelijkbaar zijn met de gepubliceerde getallen, hebben we een opzoektabel toegepast om de 8-bits Terumo data om te zetten in een 16-bits St. Jude achtig bereik voor de berekeningen in hoofdstuk 3. Deze aanpak is later verbeterd met behulp van een exacte histogramspecificatietechniek die wordt gepresenteerd in hoofdstuk 4. IVOCT-pullbacks werden vergeleken volgens visuele oriëntatiepunten en de aanpassingsfout werd geanalyseerd op zowel histogram- als lokaal intensiteitsniveau. Twee schema's, één globaal en één lokaal, voor het bepalen van het doelhistogram werden vergeleken. De één-weg-laten validatie toont aan dat de verschillen tussen twee pullbacks die zijn gematched met de twee schema's vergelijkbaar zijn met de gehele validatie set. Ondanks de fouten veroorzaakt worden door de empirische matching, de katheterpositie en de op histogram gebaseerde techniek, bleek het totale matching-verschil relatief klein te zijn. Het is voor de eerste keer is dit probleem wordt geanalyseerd met puur in vivo-afbeeldingen in plaats van met experimentele gegevens die zijn verkregen in laboratorium omstandigheden. Het voorgestelde aanpassingsraamwerk kan verder worden toegepast voor de intensiteitsnormering in andere OCT-systemen of andere beeldvormingsmodaliteiten waarbij de volgorde van de intensiteit wordt gehandhaafd.

Als toepassing van het DR-algoritme werden de optische parameters geanalyseerd als kenmerken voor de ontwikkeling van weefsel in de stent na de plaatsing van een stent in hoofdstuk 5. De drie factoren; DR-uitdovingscoëfficiënt, terugverstrooiing term en beeldintensiteit werden bepaald van het weefsel dat aan de oppervlakte lag, en van diepere lagen met een vaste dikte. De vergelijking van het weefsel in de stent in BVS-stents en die in CoCr-EES-stents vertoonde een lagere uitdovingscoëfficiënt in zowel de

oppervlakkige als de diepe lagen. De terugverstrooiing term en de intensiteit in van het weefsel in de stent waren vergelijkbaar in de oppervlakkige laag maar lager in de diepere lagen. Over het algemeen was de ontwikkeling vergelijkbaar, terwijl de verandering in vetgehalte in het weefsel in de stent minder prominent was in BVS stents.

Voor het onderscheid tussen trombus types in Hoofdstuk 6, werden de drie optische parameters bepaald binnen in met consensus getekende trombus gebieden. De resultaten toonden aan dat twee typen trombi goed kunnen worden onderscheiden met behulp van regio gebaseerde statistische waarden met een groot oppervlak onder curve-waarden. De bepaling was zeer reproduceerbaar, maar minder objectief met minimale gebruikersafhankelijkheid. Dit rechtvaardigt verder onderzoek in grotere gerandomiseerde studies.

7.4 Discussie

De beeldintensiteit, de geschatte uitdovingscoëfficiënt en de terugverstrooiing term werden in elk onderzoek in het proefschrift beschouwd. We hebben complementaire bijdragen van deze drie factoren waargenomen bij het vergelijken van gebieden door middel van statistische analyse in hoofdstuk 3. Inmiddels hebben we waargenomen dat de terugverstrooiing-term de neiging heeft om het intensiteitsniveau langs de omtrek langs het lumen in evenwicht te brengen, maar hoe het bijdraagt aan weefselkarakterisering is nog niet duidelijk. Hoewel de terugverstrooiing term sterk gerelateerd is aan de uitdovingscoëfficiënt, laten de resultaten zien dat deze extra informatie geeft voor het onderscheid tussen de weefseltypen. Daarom wordt het aanbevolen om alle drie de parameters in studies te berekenen zodat in de toekomst in meta-analyse ze kunnen worden geanalyseerd. Van deze drie parameters is de invloed van geschatte uitdoving het best te onderscheiden en waarneembaar. Vanuit het oogpunt van beeldverwerking kan de schatting van de DR-uitdoving ook worden beschouwd als normalisatie van intensiteiten op een bepaalde pixelpositie met de sommatie van de intensiteiten erachter. De zichtbaarheid van structuren kan worden verbeterd wanneer er schaduwen optreden als gevolg van hoge uitdoving of reflectie. Daarom kan de geschatte uitdovingscoëfficiënt mogelijk de detectie van structuren verbeteren, waaronder oppervlakkige dichte macrofaaginfiltraties, TCFA's, rode trombi en metalen stents.

Indicatie van infiltratie van macrofagen: In Hoofdstuk 3 toont het tapijtbeeld van de uitdovingscoëfficiënt (Fig. 13) groepen van hoge waarden met donkere schaduwen (Fig. 15). Hun histologische tegenhangers op de vier locaties geven aan dat deze regio's geassocieerd kunnen worden met hoge infiltraties van macrofagen dat verder onderzoek rechtvaardigen. Zoals beschreven in het werk van Phipps et al. [61], er zijn twee soorten macrofagen; M1-macrofagen die vetdeeltjes bevatten die de necrotische kern vormen, terwijl M2-macrofagen meer compact zijn

geconstrueerd met hoge reflectie en dienen voor ontstekingsremmende doeleinden. Er werd beweerd dat alleen die macrofagen die lipide deeltjes bevatten donkere schaduwen veroorzaken. De geanalyseerde oppervlakkige macrofagen in hoofdstuk 3 tonen zowel donkere schaduwen als een veel hogere uitdovingscoëfficiënt dan alle andere weefseltypes. Dat kan wijzen op de aanwezigheid van beide soorten macrofagen: het tapijtbeeld van de uitdovingscoëfficiënten kan een veelbelovend hulpmiddel zijn om de aanwezigheid van bovengenoemd subtype macrofagen te valideren.

Detectie van IVOCT-TCFA's: Acute coronaire syndromen (ACS's) zijn in hoge mate geassocieerd met TCFA's, wat in de histologie-anatomie wordt gedefinieerd als een dunne vezelachtige kap ($<$65 μm dikte) bovenop een grote vet depot. In IVOCT verschijnt het als een signaalrijke laag gevolgd door een signaalarm gebied gescheiden door een diffuse grens. Echter kunnen sommige andere structuren verkeerd worden aangezien voor TCFA's [8], zoals het tangentiële signaal drop-out artefact, ernstige signaalverlies door trombus en bloed restanten, of door de bovengenoemde oppervlakkige macrofaaginfiltratie. We benoemen alle structuren die lijken op TCFA in IVOCT-afbeelding als IVOCT-TCFA's. De detectie van IVOCT-TCFA's moet als een volgende stap worden beschouwd. Het grootste obstakel is de generalisatie van de referentie standaard. De kwaliteit van IVOCT wordt beperkt door het hoge ruisniveau en de vereiste spoeling van het vat en de deskundigheid van de bediener. TCFA-classificatoren vereisen grootschalige training en validatie van in vivo data. Het is een grote uitdaging om een overeenkomstige histologische bevestiging voor de referentie standaard te verkrijgen. De referentie standaard die wordt gegenereerd in IVOCT-afbeeldingen kan worden verstoord door de bovengenoemde artefacten. Een suggestie is om een referentie standaard van IVOCT-TCFA's te genereren. De katheterpositie, uitdoving door bloed in het lumen en de uitdoving van de kap kunnen worden geanalyseerd als nabewerking om de detectie te verfijnen. De dikte van de kap moet worden gemeten met een gevalideerd algoritme en worden gerapporteerd als een belangrijke populatie-eigenschap.

Detectie van IVOCT-trombus: Aangemoedigd door de uitkomst van het werk in hoofdstuk 6, kan geautomatiseerde trombusdetectie nuttig zijn voor zowel verdere validatie met grotere datasets als voor klinische toepassing in de toekomst. Bij CAD-patiënten zijn de trombi geassocieerd met de erosie of een scheur van het endotheel. Om de achterzijde van een rode trombus te bepalen, moet het in hoofdstuk 3 voorgestelde algoritme worden gebruikt. Een uitdaging voor trombusdetectie kan de detectie van de lumengrens zijn voor embolische witte trombus en rode trombus van gemiddelde grootte. In het eerste geval kan de grens van het lumen moeilijk te onderscheiden zijn vanwege het feit dat de rondom liggende trombus vlak tegen de lumenrand aanzit. In het laatste geval is de

lumenrand onzichtbaar door het hoge lichtverlies. Beide gevallen kunnen een abrupte afname van de lumen diameter veroorzaken in het longitudinale aanzicht van een pullback. Daarom kan de continuïteit van de lumen grootte in het longitudinaal aanzicht worden gebruikt als hulpinformatie voor de bepaling van de lumen contour. Trombus detectie en classificatie kunnen ook bijdragen aan een gedetailleerde evaluatie van behandel schade tijdens een PCI en leiden tot een betere therapeutische behandeling.

Vanuit het oogpunt van parameter analyse, geven de resultaten aan dat de voorgestelde pijplijn het onderscheid tussen weefseltypes kan verbeteren met behulp van traditionele lerende algoritmes. Traditionele classificatoren hebben een bovengrens van prestaties zodra de grootte van training data boven een bepaalde hoeveelheid komt, terwijl de voorspellingsnauwkeurigheid van een diep lerende netwerk ongeveer hetzelfde kan zijn als de omvang van trainingsgegevens blijft groeien [150]. Een interessante vraag is of de geschatte optische termen kunnen bijdragen aan de prestatie van classificatiesystemen op basis van diep lerende netwerken. Dit vereist echter goed gelabelde trainingsgegevens, wat een bekend knelpunt is bij de introductie van diep lerende netwerken in nieuwe beeldvormingsmodaliteiten zoals IVOCT. Het gebruik van de voorgestelde pijplijn als een voorbewerkingsstap kan de irrelevante variaties voor weefselherkenning verminderen. In de tussentijd omvat de berekening van lokale DR-uitdoving de regularisatie van de som van intensiteiten achter een specifieke pixelpositie, waardoor de geschatte waarde locatieafhankelijk is. Dit type informatie kan meestal niet effectief worden geleerd, zelfs niet door diep lerende netwerken. Daarom wordt verwacht dat het gebruik van de voorgestelde pijplijn als voorbewerking de trainingsconvergentie versnelt en de voorspellingsnauwkeurigheid met dezelfde hoeveelheid data verhoogt.

7.5 Toekomstig werk

Dit werk was gericht op het herkennen van weefseltypes op basis van beelddata. We streefden ernaar om een analyse pijplijn te ontwikkelen die uiteindelijk rechtstreeks kan worden gebruikt met de gegevens die zijn verkregen in het katheterisatielaboratorium zonder aanvullende metingen. We hebben uitvoerig de variatie van gemeten waarden geanalyseerd die kunnen worden veroorzaakt door katheterafhankelijke parameters zoals brandpunt en invalshoek. We hebben echter geen solide experimentele controlegroepen voor concrete nauwkeurigheidsanalyse opgenomen. De validatie van de geschatte uitdovingscoëfficiënt en terugverstrooiing term met fantoomgegevens is te vinden in de literatuur [59, 64]. Voor het raamwerk voor intensiteitsnormalisatie kan validatie met gegevens die zijn verkregen uit fantomen of gegevens uit de oogheelkunde interessant zijn voor het toekomstige werk, omdat hierbij meer controle kan worden verkregen over de uitlijning van de afbeeldingen. Het blijft echter een uitdaging om het afstemmingseffect te

analyseren dat wordt veroorzaakt door het verschil in katheterpositie, de druk en spanning op de vaatwand tijdens hartcyclus, enz. Het effect kan worden gecontroleerd met behulp van hoge snelheid OCT en elektrocardiografie (ECG) gestuurde opnames. De momenteel ontwikkelde hoge snelheid systemen kunnen binnen één seconde een vat van 100 mm opnemen [151], wat de opname van een lang coronair segment binnen één hartcyclus mogelijk maakt. Het verkrijgen van beelden in dezelfde hartfase kan de cardiale bewegingsverschillen minimaliseren. Een andere interessante poging kan zijn, als dit technisch mogelijk is, om een meerdere-fabrikanten-systeem te bouwen om katheters van twee leveranciers te combineren, zodanig dat beelden tegelijk kunnen worden verkregen, waardoor de problemen met beelduitlijning kan worden vermeden.

Omdat de algoritmen voor diep lerende netwerken efficiënter worden, kan dit in de toekomst misschien veel belovend zijn voor de beeldanalyse van IVOCT. Een algemene structuur kan worden opgezet voor de stent strut detectie om het brede scala van de ontwerpen van stent aan te pakken. Het gebruik van diep leren voor intensiteitsnormalisatie kan hopelijk de lokale variatie beter compenseren met een betere prestatie dan de voorgestelde op histogram gebaseerde techniek, en het vereist geen opgelegde intensiteitsvolgorde. Een generatief adversariaal netwerk zou het genereren van kunstmatige beelden mogelijk moeten maken. Dit is nog veelbelovender in combinatie met multimodale beeldvorming. IVOCT heeft de tekortkoming van de beperkte doordringingsdiepte, dus kan het geen informatie verschaffen over de grootte van de plaque en de hermodellering van het vat. Deze informatie kan worden verkregen met IVUS. Het combineren van IVOCT met IVUS zou de voordelen van beide modaliteiten kunnen combineren maar gaat ten koste van de opname snelheid. Andere bestaande technieken omvatten NIRS[1], NIRF[2] en FLIm[3] [16]. Omdat deze technieken geen diepte-informatie verschaffen, zijn deze technieken gecombineerd met IVUS- of OCT-katheters om directe informatie van de weefselstructuren per A-lijn te verkrijgen. De intravasculaire fotoakoestische (IVPA) beeldvorming detecteert vergelijkbare weefselstructuren als de voorgenoemde technieken, maar met structurele informatie met de resolutie van IVUS. Multimodale beeldvorming zorgt voor een perfecte intermodaliteits vergelijking. Aangezien afbeeldingen gelijktijdig worden verkregen, kunnen de gegevens worden uitgelijnd, ongeacht de hartcyclus. Zodra ze goed zijn gevalideerd, wordt verwacht dat de verkregen beelden kunnen evolueren naar in vivo alternatieven voor histologische gegevens voor het genereren van grote willekeurige referentie standaarden voor het trainen van weefselclassificators. Gegeven een afbeelding van één modaliteit, is het dan mogelijk om zijn tegenhangers te voorspellen in een andere modaliteit. Dit kan verder worden gebruikt om de functionaliteit van IVOCT te perfectioneren en ook om het validatiewerk van nieuwe technieken in de toekomst te versnellen.

[1] nabij-infraroodreflectiespectroscopie
[2] nabij-infraroodfluorescentie
[3] fluorescentie-levensduurbeeldvorming

Bibliography

[1] Bhatia SK. Coronary Artery Disease. *Biomaterials for Clinical Applications*. New York, NY: Springer, 2010. Chap. 2:23.

[2] GBD 2016 Mortality Collaborators. Global, regional, and national under-5 mortality, adult mortality, age-specific mortality, and life expectancy, 1970-2016: a systematic analysis for the global burden of disease study 2016. *Lancet (London, England)* 2017; 390(10100):1084–1150.

[3] World Health Organization. *World Health Statistics 2017: Monitoring Health for the SDGs, substantial development goals*. Geneva: World Health Organization, 2017.

[4] Tanaka A, Imanishi T, Kitabata H, et al. Morphology of exertion-triggered plaque rupture in patients with acute coronary syndrome: an optical coherence tomography study. *Circulation* 2008; 118(23):2368–2373.

[5] Prati F, Regar E, Mintz GS, et al. Expert review document on methodology, terminology, and clinical applications of optical coherence tomography: physical principles, methodology of image acquisition, and clinical application for assessment of coronary arteries and atherosclerosis. *Eur. Heart J.* 2010; 31(4):401–415.

[6] Xie Y, Jin H, Zeng M, Li D. Coronary artery plaque imaging. *Curr. Atheroscler. Rep.* 2017; 19(9):37.

[7] Mendis S, Puska P, Norrving B. Global atlas on cardiovascular disease prevention and control. *World Heal. Organ.* 2011:2–14.

[8] Tearney GJ, Regar E, Akasaka, et al. Consensus standards for acquisition, measurement, and reporting of intravascular optical coherence tomography studies: a report from the international working group for intravascular optical coherence tomography standardization and validation. *J. Am. Coll. Cardiol.* 2012; 59(12):1058–1072.

[9] Grover-Páez F, Zavalza-Gómez AB. Endothelial dysfunction and cardiovascular risk factors. *Diabetes Res. Clin. Pract.* 2009; 84(1):1–10.

[10] Tabas I. Macrophage apoptosis in atherosclerosis: consequences on plaque progression and the role of endoplasmic reticulum stress. *Antioxid. Redox Signal.* 2009; 11(9):2333–2339.

[11] Naghavi M, Libby P, Falk E, et al. From vulnerable plaque to vulnerable patient: a call for new definitions and risk assessment strategies: part ii. *Circulation* 2003; 108(15):1772–1778.

[12] Brancati M, Burzotta F, Trani C, Leonzi O, Cuccia C, Crea F. Coronary stents and vascular response to implantation: literature review. *Pragmat. Obs. Res.* 2017; Volume 8:137–148.

[13] Lowe HC, Narula J, Fujimoto JG, Jang IK. Intracoronary optical diagnostics: Current status, limitations, and potential. *JACC Cardiovasc. Interv.* 2011; 4(12):1257–1270.

[14] Prati F, Guagliumi G, Mintz GS, Costa M, Regar E, et al. Expert review document part 2: methodology, terminology and clinical applications of optical coherence tomography for the assessment of interventional procedures. *Eur. Heart J.* 2012; 33(20):2513–2520.

[15] Bouma BE, Villiger M, Otsuka K, Oh W-Y. Intravascular optical coherence tomography [invited]. *Biomed. Opt. Express* 2017; 8(5):2660–2686.

[16] van Soest G, Marcu L, Bouma BE, Regar E. Intravascular imaging for characterization of coronary atherosclerosis. *Curr. Opin. Biomed. Eng.* 2017; 3:1–12.

[17] Jang IK, Tearney G, Bouma B. Visualization of tissue prolapse between coronary stent struts by optical coherence tomography: comparison with intravascular ultrasound. *Circulation* 2001; 104(22):2754.

[18] Yabushita H, Bouma BE, Houser SL, et al. Characterization of human atherosclerosis by optical coherence tomography. *Circulation* 2002; 106(13):1640–1645.

[19] Tearney GJ, Yabushita H, Houser SL, et al. Quantification of macrophage content in atherosclerotic plaques by optical coherence tomography. *Circulation* 2003; 107(1):113–119.

[20] Serruys PW, Rutherford JD. The Birth, and Evolution, of Percutaneous Coronary Interventions: A Conversation With Patrick Serruys, MD, PhD. *Circulation* 2016; 134(2):97–100.

[21] Taniwaki M, Stefanini GG, Silber S, et al. 4-year clinical outcomes and predictors of repeat revascularization in patients treated with new-generation drug-eluting stents a report from the resolute all-comers trial (a randomized comparison of a zotarolimus-eluting stent with an everolimus-eluting stent for percutaneous coronary intervention). *J. Am. Coll. Cardiol.* 2014; 63:1617–1625.

[22] Stolker JM, Cohen DJ, Kennedy KF, et al. Repeat revascularization after contemporary percutaneous coronary intervention: an evaluation of staged, target lesion, and other unplanned revascularization procedures during the first year. *Circ. Cardiovasc. Interv.* 2012; 5(6):772–782.

[23] Nakano M, Yahagi K, Otsuka F, et al. Causes of early stent thrombosis in patients presenting with acute coronary syndrome an ex vivo human autopsy study. *J. Am. Coll. Cardiol.* 2014; 63:2510–2520.

[24] Habara M, Terashima M, Suzuki T. Detection of atherosclerotic progression with rupture of degenerated in-stent intima five years after bare-metal stent implantation using optical coherence tomography. *J. Invasive Cardiol.* 2009; 21(10):552–553.

[25] Park S-J, Kang S-J, Virmani R, Nakano M, Ueda Y. In-stent neoatherosclerosis: a final common pathway of late stent failure. *J. Am. Coll. Cardiol.* 2012; 59(23):2051–2057.

[26] Ali ZA, Maehara A, Généreux P, et al. Optical coherence tomography compared with intravascular ultrasound and with angiography to guide coronary stent implantation (ILUMIEN III: OPTIMIZE PCI): a randomised controlled trial. *Lancet* 2016; 388(10060):2618–2628.

[27] Xu C, Schmitt JM, Carlier SG, Virmani R. Characterization of atherosclerosis plaques by measuring both backscattering and attenuation coefficients in optical coherence tomography. *J. Biomed. Opt.* 2008; 13(3):034003.

[28] van Soest G, Koljenović S, Bouma BE, et al. Atherosclerotic tissue characterization in vivo by optical coherence tomography attenuation imaging. *J. Biomed. Opt.* 2010; 15(1):11105.

[29] van der Sijde JN, Karanasos A, Villiger M, Bouma BE, Regar E. First-in-man assessment of plaque rupture by polarization-sensitive optical frequency domain imaging in vivo. *Eur. Heart J.* 2016; 37(24):1932–1932.

[30] Villiger M, Karanasos A, Ren J, et al. Intravascular polarization sensitive optical coherence tomography in human patients. *Conference on Lasers and Electro-Optics*. Optical Society of America, 2016:AW1O.2.

[31] Mozaffarian D, Benjamin EJ, Go AS, et al. Heart disease and stroke statistics—2016 update. *Circulation* 2016.

[32] Prati F, Uemura S, Souteyrand G, et al. Oct-based diagnosis and management of STEMI associated with intact fibrous cap. *JACC Cardiovasc. Imaging* 2013; 6(3):283–287.

[33] Regar E, van Leeuwen A, Serruys PW, eds. *Optical Coherence Tomography in Cardiovascular Research*. 1st ed. CRC Press, Mar. 2007.

[34] van Soest G, Regar E, Goderie TP, et al. Pitfalls in plaque characterization by octimage artifacts in native coronary arteries. *JACC Cardiovasc. Imaging* 2011; 4(7):810–813.

[35] Huang Y-P, Saarakkala S, Toyras J, Wang L-K, Jurvelin JS, Zheng Y-P. Effects of optical beam angle on quantitative optical coherence tomography (OCT) in normal and surface degenerated bovine articular cartilage. *Phys. Med. Biol.* 2011; 56(2):491.

[36] Courtney BK, Robertson AL, Maehara A, et al. Effects of transducer position on backscattered intensity in coronary arteries. *Ultrasound Med. Biol.* 2002; 28(1):81–91.

[37] Picano E, Landini L, Distante A, et al. Angle dependence of ultrasonic backscatter in arterial tissues: a study in vitro. *Circulation* 1985; 72(3):572–576.

[38] de Kroon MGM, van der Wal LF, J. GW, N. B. Angle-dependent backscatter from the arterial wall. *Ultrasound in Medicine & Biology* 1991; 17(2):121–126.

[39] Di Mario C, Madretsma S, Linker D, et al. The angle of incidence of the ultrasonic beam: a critical factor for the image quality in intravascular ultrasonography. *Am. Heart J.* 1993; 125(2, Part 1):442 –448.

[40] Ughi GJ, Adriaenssens T, Sinnaeve P, Desmet W, D'hooge J. Automated tissue characterization of in vivo atherosclerotic plaques by intravascular optical coherence tomography images. *Biomed. Opt. Express* 2013; 4(7):1014–30.

[41] Nam HS, Kim C-S, Lee JJ, Song JW, Kim JW, Yoo H. Automated detection of vessel lumen and stent struts in intravascular optical coherence tomography to evaluate stent apposition and neointimal coverage. *Med. Phys.* 2016; 43(4):1662–1675.

[42] Menguy P-Y, Péry E, Ouchchane L, et al. Preliminary results for the supervised detection of lumen and stent from OCT pullbacks. *IRBM* 2016; 37(5):271–275.

[43] Ughi GJ, Adriaenssens T, Onsea K, et al. Automatic segmentation of in-vivo intra-coronary optical coherence tomography images to assess stent strut apposition and coverage. *Int. J. Cardiovasc. Imaging* 2012; 28(2):229–241.

[44] Wang A, Eggermont J, Dekker N, et al. Automatic stent strut detection in intravascular optical coherence tomographic pullback runs. *Int. J. Cardiovasc. Imaging* 2013; 29(1):29–38.

[45] Wang A, Tang X. Automatic segmentation of vessel lumen in intravascular optical coherence tomography images. *2016 IEEE International Conference on Mechatronics and Automation*. 2016:948–953.

[46] Dubuisson F, Péry E, Ouchchane L, et al. Automated peroperative assessment of stents apposition from OCT pullbacks. *Comput. Biol. Med.* 2015; 59:98–105.

[47] Wang A, Nakatani S, Eggermont J, et al. Automatic detection of bioresorbable vascular scaffold struts in intravascular optical coherence tomography pullback runs. *Biomed. Opt. Express* 2014; 5(10):3589.

[48] Valery T. *Tissue Optics: Light Scattering Methods and Instruments for Medical Diagnosis*. 2nd ed. Vol. 23. Washington: SPIE, 2007:231.

[49] Pedrotti FL, Pedrotti LS. *Introduction to Optics*. 2nd ed. Englewood Cliffs: Prentice-Hall International, 1993:407–411.

[50] Sullivan LM, Dukes Ka, Losina E. Tutorial in biostatistics. an introduction to hierarchical linear modelling. *Statistics in medicine* 1999; 18(7):855–888.

[51] van der Meer FJ. Vascular applications of quantitative optical coherence tomography. Dissertation. Universiteit van Amsterdam, 2005:86.

[52] Precht H, Leth PM, Thygesen J, et al. Optimisation of post mortem cardiac computed tomography compared to optical coherence tomography and histopathology – technical note. *JOFRI* 2014; 2(2):85 –90.

[53] Goutte C, Gaussier E. A probabilistic interpretation of precision, recall and f-score, with implication for evaluation. *Advances in Information Retrieval: 27th European Conference on IR Research, ECIR 2005, Santiago de Compostela, Spain, March 21-23, 2005. Proceedings*. Berlin, Heidelberg: Springer Berlin Heidelberg, 2005:345–359.

[54] Phipps JE, Vela D, Hoyt T, et al. Macrophages and intravascular OCT bright spots: a quantitative study. *JACC Cardiovasc. Imaging* 2015; 8:63–72.

[55] Tuchin V. Optical coherence tomography and heterodyning imaging. *Tissue Optical Light Scattering Methods Instruments Medical Diagnosis*. 2nd ed. Bellingham, WA 98227-0010: SPIE Press, 2007. Chap. 9:565–589.

[56] Tenekecioglu E, Albuquerque FN, Sotomi Y, et al. Intracoronary optical coherence tomography: clinical and research applications and intravascular imaging software overview. *Catheterization and Cardiovascular Interventions*; 89(4):679–689.

[57] Nakatani S, Onuma Y, Ishibashi Y, et al. Temporal evolution of strut light intensity after implantation of bioresorbable polymeric intracoronary scaffolds in the ABSORB cohort B trial. *Circulation* 2014; 78(8):1873–1881.

[58] Nakatani S, Ishibashi Y, Sotomi Y, et al. Bioresorption and vessel wall integration of a fully bioresorbable polymeric everolimus-eluting scaffold: optical coherence tomography, intravascular ultrasound, and histological study in a porcine model with 4-year follow-up. *JACC Cardiovasc. Interv.* 2016; 9(8):838–851.

[59] Vermeer KA, Mo J, Weda JJA, Lemij HG, Boer JF de. Depth-resolved model-based reconstruction of attenuation coefficients in optical coherence tomography. *Biomed. Opt. Express* 2013; 5(1):322–37.

[60] Tearney GJ. Oct imaging of macrophages: a bright spot in the study of inflammation in human atherosclerosis. *JACC Cardiovasc. Imaging* 2015; 8(1):73–75.

[61] Phipps JE, Vela D, Hoyt T, et al. Macrophages and intravascular OCT bright spots: a quantitative study. *JACC Cardiovasc. Imaging* 2015; 8(1):63–72.

[62] Minami Y, Hoyt T, Phipps JE, et al. Lipid-lowering therapy stabilizes the complexity of non-culprit plaques in human coronary artery : a quantitative assessment using OCT bright spot algorithm. *Int. J. Cardiovasc. Imaging* 2017; 33(4):453–461.

[63] Li J, Feroldi F, de Lange J, Daniels JMA, Grünberg K, de Boer JF. Polarization sensitive optical frequency domain imaging system for endobronchial imaging. *Opt. Express* 2015; 23(3):3390–3402.

[64] Schmitt JM, Knuttel A, Bonner RF, Knüttel. Measurement of optical properties of biological tissues by low-coherence reflectometry. *Appl. Opt.* 1993; 32(30):6032–6042.

[65] Schmitt JM, Knüttel a, Yadlowsky M, Eckhaus Ma. Optical-coherence tomography of a dense tissue: statistics of attenuation and backscattering. *Phys. Med. Biol.* 1994; 39(10):1705–1720.

[66] Sergeeva EA, Dolin LS, Kamensky VA, Shakhova NM, Richards-kortum R. Novel algorithm of processing optical coherence tomography images for differentiation of biological tissue pathologies. *J. Biomed. Opt.* 2005; 10(12):1–11.

[67] Almasian M, Bosschaart N, van Leeuwen AGJM, Faber DJ. Validation of quantitative attenuation and backscattering coefficient measurements by optical coherence tomography in the concentration-dependent and multiple scattering regime. *J. Biomed. Opt.* 2015; 20(12):121314.

[68] Faber D, van der Meer F, Aalders M, van Leeuwen AGJM. Quantitative measurement of attenuation coefficients of weakly scattering media using optical coherence tomography. *Opt. Express* 2004; 12(19):4353–4365.

[69] Lee P, Gao W, Zhang X. Performance of single-scattering model versus multiple-scattering model in the determination of optical properties of biological tissue with optical coherence tomography. *Appl. Opt.* 2010; 49(18):3538–3544.

[70] Cauberg EC, de Bruin DM, Faber DJ, et al. Quantitative measurement of attenuation coefficients of bladder biopsies using optical coherence tomography for grading urothelial carcinoma of the bladder. *J. Biomed. Opt.* 2010; 15(6):066013.

[71] Gong P, McLaughlin RA, Liew YM, Munro PRT, Wood FM, Sampson DD. Assessment of human burn scars with optical coherence tomography by imaging the attenuation coefficient of tissue after vascular masking. *J. Biomed. Opt.* 2013; 19(2):21111.

[72] Li J, Tu Z, Shen Z, et al. Quantitative measurement of optical attenuation coefficients of cell lines cne1, cne2, and np69 using optical coherence tomography. *Lasers Med. Sci.* 2013; 28(2):621–625.

[73] Yang Y, Wang T, Biswal NC, et al. Optical scattering coefficient estimated by optical coherence tomography correlates with collagen content in ovarian tissue. *J. Biomed. Opt.* 2011; 16(9):090504.

[74] Mujat M, Ferguson RD, Hammer DX, Gittins C, Iftimia N. Automated algorithm for breast tissue differentiation in optical coherence tomography. *J. Biomed. Opt.* 2009; 14(3):034040.

[75] Gan Y, Tsay D, Amir SB, Marboe CC, Hendon CP. Automated classification of optical coherence tomography images of human atrial tissue. *J. Biomed. Opt.* 2016; 21(10):101407.

[76] Gargesha M, Shalev R, Prabhu D, et al. Parameter estimation of atherosclerotic tissue optical properties from three-dimensional intravascular optical coherence tomography. *J. Med. Imaging* 2015; 2(1):016001.

[77] Yonetsu T, Kim JS, Kato K, et al. Comparison of incidence and time course of neoatherosclerosis between bare metal stents and drug-eluting stents using optical coherence tomography. *Am. J. Cardiol.* 2012; 110(7):933–939.

[78] Nagoshi R, Shinke T, Otake H, et al. Qualitative and quantitative assessment of stent restenosis by optical coherence tomography: comparison between drug-eluting and bare-metal stents. *Circ. J.* 2013; 77(3):652–660.

[79] Gnanadesigan M, Hussain AS, White S, et al. Optical coherence tomography attenuation imaging for lipid core detection: an ex-vivo validation study. *Int. J. Cardiovasc. Imaging* 2017; 33(1):5–11.

[80] Rodriguez CLR, Szu JI, Eberle MM, et al. Decreased light attenuation in cerebral cortex during cerebral edema detected using optical coherence tomography. *Neurophotonics* 2014; 1(2):025004.

[81] Smith GT, Dwork N, O'Connor D, et al. Automated, depth-resolved estimation of the attenuation coefficient from optical coherence tomography data. *IEEE Trans. Med. Imaging* 2015; 34(12):2592–2602.

[82] Girard MJA, Strouthidis NG, Ethier CR, Mari JM. Shadow removal and contrast enhancement in optical coherence tomography images of the human optic nerve head. *Invest. Ophthalmol. Vis. Sci.* 2011; 52(10):7738–7748.

[83] Mari JM, Strouthidis NG, Park SC, Girard MJA. Enhancement of lamina cribrosa visibility in optical coherence tomography images using adaptive compensation. *Invest. Ophthalmol. Vis. Sci.* 2013; 54(3):2238–2247.

[84] Foin N, Mari JM, Davies JE, Di Mario C, Girard MJA. Imaging of coronary artery plaques using contrast-enhanced optical coherence tomography. *Eur. Heart J. Cardiovasc. Imaging* 2013; 14(1):85.

[85] Teo JC, Foin N, Otsuka F, et al. Optimization of coronary optical coherence tomography imaging using the attenuation-compensated technique: a validation study. *Eur. Heart J. Cardiovasc. Imaging* 2016; 2(3):1035–1046.

[86] Lee R, Foin N, Otsuka F, et al. Intravascular assessment of arterial disease using compensated OCT in comparison with histology. *JACC Cardiovasc. Imaging* 2016; 9(3):321–322.

[87] Goldberg BD, Vakoc BJ, Oh W-Y, et al. Performance of reduced bit-depth acquisition for optical frequency domain imaging. *Opt. Express* 2009; 17(19):16957–16968.

[88] Liu S, Eggermont J, Nakatani S, Lelieveldt BPF, Dijkstra J. Light intensity matching between different intravascular optical coherence tomography systems. *Proc. SPIE* 2016; 9689:96893D–96893D–7.

[89] Phipps JE, Hoyt T, Vela D, et al. Diagnosis of thin-capped fibroatheromas in intravascular optical coherence tomography images. *Circ. Cardiovasc. Interv.* 2016; 9(7).

[90] Liu S, Eggermont J, Wolterbeek R, et al. Analysis and compensation for the effect of the catheter position on image intensities in intravascular optical coherence tomography. *J. Biomed. Opt.* 2016; 21(12):126005.

[91] Varkentin A, Otte M, Meinhardt-Wollweber M, et al. Simple model to simulate oct-depth signal in weakly and strongly scattering homogeneous media. *J. Opt.* 2016; 18(12):125302.

[92] Rico-Jimenez JJ, Campos-Delgado DU, Villiger M, Otsuka K, E. BB, Jo JA. Automatic classification of atherosclerotic plaques imaged with intravascular oct. *Biomed. Opt. Express* 2016; 7(10):4069–4085.

[93] Rheude TA, Xhepa E, Byrne RA. Case report markedly different tissue types on optical coherence tomography imaging in a patient with multiple lesion. *Catheter. Cardiovasc. Interv.* 2017; 89(6):E181–E184.

[94] Jia H, Dai J, Hou J, et al. Effective anti-thrombotic therapy without stenting: intravascular optical coherence tomography-based management in plaque erosion (the EROSION study). *Eur. Heart J.* 2017; 38(11):792–800.

[95] MacNeill BD, Jang IK, Bouma BE, et al. Focal and multi-focal plaque macrophage distributions in patients with acute and stable presentations of coronary artery disease. *J. Am. Coll. Cardiol.* 2004; 44(5):972–979.

[96] Ino Y, Kubo T, Tanaka A, et al. Difference of culprit lesion morphologies between ST-segment elevation myocardial infarction and non-ST-segment elevation acute coronary syndrome. *JACC Cardiovasc. Interv.* 2011; 4(1):76–82.

[97] Tian J, Hou J, Xing L, et al. Significance of intraplaque neovascularization for vulnerability: optical coherence tomography study. *J. Am. Coll. Cardiol.* 2012; 59(13 Supplement):E1439.

[98] Tanimoto T, Imanishi T, Tanaka A, et al. Various types of plaque disruption in culprit coronary artery visualized by optical coherence tomography in a patient with unstable angina. *Circulation Journal* 2009; 73(1):187–189.

[99] Uemura S, Ishigami KI, Soeda T, et al. Thin-cap fibroatheroma and microchannel findings in optical coherence tomography correlate with subsequent progression of coronary atheromatous plaques. *Eur. Heart J.* 2012; 33(1):78–85.

[100] Taruya A, Tanaka A, Nishiguchi T, et al. Vasa vasorum restructuring in human atherosclerotic plaque vulnerability: a clinical optical coherence tomography study. *J Am Coll Cardiol* 2015; 65(23):2469–2477.

[101] Kume T, Akasaka T, Kawamoto T, et al. Assessment of coronary arterial thrombus by optical coherence tomography. *Am. J. Cardiol.* 2006; 97(12):1713–7.

[102] Karanasos A, Tu S, van Ditzhuijzen NS, et al. A novel method to assess coronary artery bifurcations by oct: cut-plane analysis for side-branch ostial assessment froma main-vessel pullback. *Eur. Heart J. Cardiovasc. Imaging* 2015; 16(2):177–189.

[103] Cao Y, Jin Q, Chen Y, et al. Automatic identification of side branch and main vascular measurements in intravascular optical coherence tomography images. *2017 IEEE 14th International Symposium on Biomedical Imaging (ISBI 2017)*. Melbourne,VIC, 2017:608–611.

[104] Wang Z, Jenkins MW, Linderman GC, et al. 3-d stent detection in intravascular OCT using a bayesian network and graph search. *IEEE Trans. Med. Imaging* 2015; 34(7):1549–1561.

[105] Adriaenssens T, Ughi GJ, Dubois C, et al. Automated detection and quantification of clusters of malapposed and uncovered intracoronary stent struts assessed with optical coherence tomography. *Int. J. Cardiovasc. Imaging* 2014; 30(5):839–848.

[106] Sotomi Y, Tateishi H, Suwannasom P, et al. Quantitative assessment of the stent/scaffold strut embedment analysis by optical coherence tomography. *Int. J. Cardiovasc. Imaging* 2016; 32(6):871–883.

[107] Chen C-L, Ishikawa H, Wollstein G, et al. Individual A-scan signal normalization between two spectral domain optical coherence tomography devices. *Invest. Ophthalmol. Vis. Sci.* 2013; 54(5):3463–71.

[108] Chen C-L, Ishikawa H, Wollstein G, Bilonick RA, Kagemann L, Schuman JS. Virtual averaging making nonframe-averaged optical coherence tomography images comparable to frame-averaged images. *Transl. Vis. Sci. Technol.* 2016; 5(1):1.

[109] Chen C-L, Ishikawa H, Ling Y, et al. Signal normalization reduces systematic measurement differences between spectral-domain optical coherence tomography devices. *Invest. Ophthalmol. Vis. Sci.* 2013; 54(12):7317–22.

[110] Chen C-L, Ishikawa H, Wollstein G, Bilonick RA, Kagemann L, Schuman JS. Signal normalization reduces image appearance disparity among multiple optical coherence tomography devices. *Transl. Vis. Sci. Technol.* 2017; 6(1):13.

[111] Hummel RA. Histogram modification techniques. *Computer Graphics and Image Processing* 1975; 4(3):209–224.

[112] Nikolova M, Wen Y-W, Chan R. Exact histogram specification for digital images using a variational approach. *J. Math. Imaging Vis.* 2013; 46(3):309–325.

[113] Coltuc D, Bolon P, Chassery JM. Exact histogram specification. *IEEE Trans. Image Process.* 2006; 15(5):1143–1152.

[114] Wan Y, Shi D. Joint exact histogram specification and image enhancement through the wavelet transform. *IEEE Transactions on Image Processing* 2007; 16(9):2245–2250.

[115] Chen C-L, Ishikawa H, Wollstein G, et al. Histogram matching extends acceptable signal strength range on optical coherence tomography images. *Invest. Ophthalmol. Vis. Sci.* 2015; 56(6):3810–9.

[116] Stanciu SG, Stanciu GA, Coltuc D. Automated compensation of light attenuation in confocal microscopy by exact histogram specification. *Microsc. Res. Tech.* 2010; 73(3):165–175.

[117] Euser AM, Dekker FW, le Cessie S. A practical approach to Bland-Altman plots and variation coefficients for log transformed variables. *J. Clin. Epidemiol.* 2008; 61(10):978–982.

[118] Liu S, Sotomi Y, Eggermont J, et al. Tissue characterization with depth-resolved attenuation coefficient and backscatter term in intravascular optical coherence tomography images. *J. Biomed. Opt.* 2017; 22(9):1–16.

[119] Onuma Y, Sotomi Y, Shiomi H, et al. Two-year clinical, angiographic, and serial optical coherence tomographic follow-up after implantation of an everolimuseluting bioresorbable scaffold and an everolimus-eluting metallic stent: Insights from the randomised ABSORB Japan trial. *EuroIntervention* 2016; 12(9):1090–1101.

[120] Serruys PW, Chevalier B, Sotomi Y, et al. Comparison of an everolimus-eluting bioresorbable scaffold with an everolimus-eluting metallic stent for the treatment of coronary artery stenosis (ABSORB II): a 3 year, randomised, controlled, single-blind, multicentre clinical trial. *Lancet* 2016; 388(10059):2479–2491.

[121] Sotomi Y, Suwannasom P, Serruys PW, Onuma Y. Possible mechanical causes of scaffold thrombosis: insights from case reports with intracoronary imaging. 2017; 12(14):1747–1756.

[122] Otake H, Shite J, Ikeno F, et al. Evaluation of the peri-strut low intensity area following sirolimus-and paclitaxel-eluting stents implantation: Insights from an optical coherence tomography study in humans. 2012; 157:38–42.

[123] Imanaka T, Fujii K, Hao H, et al. Ex vivo assessment of neointimal characteristics after drug-eluting stent implantation: Optical coherence tomography and histopathology validation study. *Int. J. Cardiol.* 2016; 221:1043–1047.

[124] Nakano M, Vorpahl M, Otsuka F, et al. Ex vivo assessment of vascular response to coronary stents by optical frequency domain imaging. *JACC Cardiovasc. Imaging* 2012; 5(1):71–82.

[125] Malle C, Tada T, Steigerwald K, et al. Tissue characterization after drug-eluting stent implantation using optical coherence tomography. *Arterioscler. Thromb. Vasc. Biol.* 2013; 33(6):1376–1383.

[126] Sabaté M, Windecker S, Iñiguez A, et al. Everolimus-eluting bioresorbable stent vs. durable polymer everolimus-eluting metallic stent in patients with ST-segment elevation myocardial infarction: results of the randomized ABSORB ST-segment elevation myocardial infarction-TROFI II trial. *Eur. Heart J.* 2016; 37(3):229–240.

[127] Authors/Task Force members, Windecker S, Kolh P, et al. 2014 ESC/EACTS guidelines on myocardial revascularization: the task force on myocardial revascularization of the European Society of Cardiology (ESC) and the European Association for Cardio-Thoracic Surgery (EACTS) developed with the special contribution of the European Association of Percutaneous Cardiovascular Interventions (EAPCI). *Eur. Heart J.* 2014; 35(37):2541–2619.

[128] Räber L, Onuma Y, Brugaletta S, et al. Arterial healing following primary PCI using the Absorb everolimus-eluting bioresorbable vascular scaffold (Absorb BVS) versus the durable polymer everolimus-eluting metallic stent (XIENCE) in patients with acute ST-elevation myocardial infarction: Ration. *EuroIntervention* 2016; 12(4):482–489.

[129] Nakatani S, Sotomi Y, Ishibashi Y, et al. Comparative analysis method of permanent metallic stents (XIENCE) and bioresorbable poly-L-lactic (PLLA) scaffolds (Absorb) on optical coherence tomography at baseline and follow-up. *EuroIntervention* 2016; 12(12):1498–1509.

[130] Gomez-Lara J, Brugaletta S, Farooq V, et al. Head-to-head comparison of the neointimal response between metallic and bioresorbable everolimus-eluting scaffolds using optical coherence tomography. *JACC Cardiovasc. Interv.* 2011; 4(12):1271–1280.

[131] Tellez A, Afari ME, Buszman PP, et al. Peri-strut low-intensity areas in optical coherence tomography correlate with peri-strut inflammation and neointimal proliferation: An in-vivo correlation study in the familial hypercholesterolemic coronary swine model of in-stent restenosis. *Coron. Artery Dis.* 2014; 25(7):595–601.

[132] Otsuka F, Pacheco E, Perkins LEL, et al. Long-term safety of an everolimus-eluting bioresorbable vascular scaffold and the cobalt-chromium XIENCE v stent in a porcine coronary artery model. *Circ. Cardiovasc. Interv.* 2014; 7(3):330–342.

[133] Sotomi Y, Suwannasom P, Tenekecioglu E, et al. Differential aspects between cobalt-chromium everolimus drug-eluting stent and Absorb everolimus bioresorbable vascular scaffold: from bench to clinical use. *Expert Rev. Cardiovasc. Ther.* 2015; 13(10):1127–1145.

[134] Windecker S. Comparison of the ABSORB Everolimus Eluting Bioresorbable Vascular Scaffold System With a Drug- Eluting Metal

Stent (Xience) in Acute ST-Elevation Myocardial Infarction: 2-year results of TROFI II Study. presented at TCT, 2016.

[135] Taniguchi Y, Otake H, Shinke T, et al. Two-year vessel healing after everolimus-eluting stent implantation: Serial assessment by optical coherence tomography. *J. Cardiol.* 2015; 65(4):298–304.

[136] Jolly SS, Cairns J, Yusuf S, et al. Design and rationale of the TOTAL trial: a randomized trial of routine aspiration ThrOmbecTomy with percutaneous coronary intervention (PCI) versus PCI ALone in patients with ST-elevation myocardial infarction undergoing primary PCI. *Am. Heart J.* 2014; 167(3):315–321.e1.

[137] Jolly SS, Cairns JA, Yusuf S, et al. Randomized trial of primary PCI with or without routine manual thrombectomy. *N. Engl. J. Med.* 2015; 372(15):1389–1398.

[138] Bhindi R, Kajander OA, Jolly SS, et al. Culprit lesion thrombus burden after manual thrombectomy or percutaneous coronary intervention-alone in ST-segment elevation myocardial infarction: The optical coherence tomography sub-study of the TOTAL (ThrOmbecTomy versus PCI ALone) trial. *Eur. Heart J.* 2015; 36(29):1892–1900.

[139] Bland JM, Altman DG. Statistical methods for assessing agreement between two methods of clinical measurement. *The Lancet* 1986; 327(8476):307 –310.

[140] Saia F, Komukai K, Capodanno D, et al. Eroded versus ruptured plaques at the culprit site of STEMI: in vivo pathophysiological features and response to primary PCI. *JACC Cardiovasc. Imaging* 2015; 8(5):566–575.

[141] Wang L, Parodi G, Maehara A, et al. Variable underlying morphology of culprit plaques associated with ST-elevation myocardial infarction: an optical coherence tomography analysis from the SMART trial. *Eur. Hear. J. - Cardiovasc. Imaging* 2015; 16(12):1381–1389.

[142] Rittersma SZH, van der Wal AC, Koch KT, et al. Plaque instability frequently occurs days or weeks before occlusive coronary thrombosis: A pathological thrombectomy study in primary percutaneous coronary intervention. *Circulation* 2005; 111(9):1160–1165.

[143] Yunoki K, Naruko T, Sugioka K, et al. Thrombus aspiration therapy and coronary thrombus components in patients with acute ST-elevation myocardial infarction. *J. Atheroscler. Thromb.* 2013; 20(6):524–537.

[144] Bezerra HG, Costa MA, Guagliumi G, Rollins AM, Simon DI. Intracoronary optical coherence tomography: a comprehensive review. *JACC Cardiovasc. Interv.* 2009; 2(11):1035–1046.

[145] Itoh T, Fusazaki T, Kimura T, et al. ”intracoronary whirling current phenomenon” and thrombus formation after sirolimus-eluting stent implantation visualized by optical coherence tomography. *Circ. Cardiovasc. Interv.* 2009; 2(3):264–267.

[146] Quadros AS, Cambruzzi E, Sebben J, et al. Red versus white thrombi in patients with ST-elevation myocardial infarction undergoing primary

percutaneous coronary intervention: Clinical and angiographic outcomes. *Am. Heart J.* 2012; 164(4):553–560.

[147] Kramer MC, van der Wal AC, Koch KT, et al. Presence of older thrombus is an independent predictor of long-term mortality in patients with ST-elevation myocardial infarction treated with thrombus aspiration during primary percutaneous coronary intervention. *Circulation* 2008; 118(18):1810–1816.

[148] Yunoki K, Naruko T, Inoue T, et al. Relationship of thrombus characteristics to the incidence of angiographically visible distal embolization in patients with ST-segment elevation myocardial infarction treated with thrombus aspiration. *JACC Cardiovasc. Interv.* 2013; 6(4):377–385.

[149] Yang G, Zhang X, Meng Q, et al. Evaluation of the characterization of thrombi in vitro by optical coherence tomography. *Int. J. Cardiol.* 2016; 220:116–121.

[150] Goodfellow I, Bengio Y, Courville A. *Deep Learning*. MIT Press, 2016.

[151] Katagiri Y, Tenekecioglu E, Serruys P, et al. What does the future hold for novel intravascular imaging devices: a focus on morphological and physiological assessment of plaque. *Expert Rev. Med. Devices* 2017; 14(12):985–999.

Publications

Publications in Peer-review Journals:

- **S. Liu**, Y. Sotomi, J. Eggermont, G. Nakazawa, S. Torii, T. Ijichi, Y. Onuma, P. W. Serruys, B. P. F. Lelieveldt, and J. Dijkstra, **Tissue Characterization with Depth-Resolved Attenuation Coefficient and Backscatter Term in Intravascular Optical Coherence Tomography Images**, *J. Biomed. Opt.*, vol. 22, no. 9, p. 1, 2017.

- **S. Liu**, J. Eggermont, R. Wolterbeek, A. Broersen, C. A. G. R. Busk, H. Precht, B. P. F. Lelieveldt, and J. Dijkstra, **Analysis and Compensation for the Effect of the Catheter Position on Image Intensities in Intravascular Optical Coherence Tomography**, *J. Biomed. Opt.*, vol. 21, no. 12, p. 126005, Dec. 2016.

- Y. Sotomi, Y. Onuma, **S. Liu**, T. Asano, J. Eggermont, Y. Katagiri, R. Cavalcante, R. J. de Winter, J. J. Wykrzykowska, S. Brugaletta, L. Räber, M. Sabaté, S. Windecker, J. Dijkstra, P. W Serruys, **Quality Difference of Neointima Following the Implantation of Everolimus Eluting Bioresorbable Scaffold and Metallic Stent in Patients with ST Elevation Myocardial Infarction: Quantitative Assessments by Light Intensity, Light Attenuation, and Backscatter on Optical Coherence Tomography in TROFI II Trial**, *EuroIntervension*, 2018 Feb 27. pii: EIJ-D-17-00884. doi: 10.4244/EIJ-D-17-00884. [Epub ahead of print] PubMed PMID: 29488886.

- Y. Sotomi, Y. Onuma, J. Dijkstra, J. Eggermont, **S. Liu**, E. Tenekecioglu, Y. Zeng, T. Asano, R. J. de Winter, J. J. Popma, K. Kozuma, K. Tanabe, P. W. Serruys, and T. Kimura, **Impact of Implantation Technique and Plaque Morphology on Strut Embedment and Scaffold Expansion of Polylactide Bioresorbable Scaffold - Insights From ABSORB Japan Trial**, *Circ. J.*, vol. 80, no. 11, pp. 2317–2326, Oct. 2016.

- Y. Sotomi, H. Tateishi, P. Suwannasom, J. Dijkstra, J. Eggermont, **S. Liu**, E. Tenekecioglu, Y. Zheng, M. Abdelghani, R. Cavalcante, R. J. de Winter, J. J. Wykrzykowska, Y. Onuma, P. W. Serruys, and T. Kimura, **Quantitative Assessment of the Stent/Scaffold Strut Embedment**

Analysis by Optical Coherence Tomography, *Int. J. Cardiovasc. Imaging*, vol. 32, no. 6, pp. 871–883, Jun. 2016.

- S. Nakatani, Y. Onuma, Y. Ishibashi, J. Eggermont, Y.-J. Zhang, C. M. Campos, Y. K. Cho, **S. Liu**, J. Dijkstra, J. H. C. Reiber, *et al*, **Temporal Evolution of Strut Light Intensity After Implantation of Bioresorbable Polymeric Intracoronary Scaffolds in the ABSORB Cohort B Trial**, *Circ. J.*, vol. 78, no. 8, pp. 1873–1881, 2014.
- R. Stettler, J. Dijkstra, L. Räber, R. Torii, Y.-J. Zhang, A. Karanasos, **S. Liu**, T. Crake, S. Hamshere, H. M. Garcia-Garcia, E. Tenekecioglu, M. Ozkor, S. Windecker, P. W. Serruys, E. Regar, A. Mathur, and C. V Bourantas, **Neointima and Neoatherosclerotic Characteristics in Bare Metal and First and Second Generation Drug Eluting Stents in Patients Admitted with Cardiovascular Events Attributed to Stent Failure: an Optical Coherence Tomography Study**, *EuroIntervention*, Jun. 2017.
- W. Sun, C. Wang, D. Bu, **S. Liu**, B. Wu, and M.Ouyang, **A Fuzzy Cerebellar Model Articulation Controller Based Visual Servo System for Robot**, *Int. J. Control. Autom. Syst.*, vol. 10, no. 2, pp. 430–436, Apr. 2012.

Manuscripts Under Review in Peer-review Journals:

- **S. Liu**, O. Dzyubachyk, J. Eggermont, S. Nakatani, B. P. F. Lelieveldt, and J. Dijkstra, **Histogram-Based Standardization of Intravascular Optical Coherence Tomography Images Acquired from Different Imaging Systems**, *Med. Phys.*, Accepted.
- T. P. Kaivosoja, **S. Liu**, J. Dijkstra, H. Huhtala, T. Sheth and O.A. Kajander, **Comparison of Visual Assessment and Computer Image Analysis of Intracoronary Thrombus Type by Optical Coherence Tomography in Clinical Patients**, *Interventional Cardiology*, Under Review.

Publication and Presentation in International Conference Proceedings:

- **S. Liu**, J. Eggermont, R. Wolterbeek, B. P. F. Lelieveldt, J. Dijkstra, **Influence of Distance and Incident Angle on Light Intensities in Intravascular Optical Coherence Tomography Pullback Runs (Conference Presentation and Publication)**, in *Photonic Therapeutics and Diagnostics XII*, Hyun Wook Kang; Guillermo J. Tearney; Kenton W. Gregory; Laura Marcu; Melissa C. Skala; Paul J. Campagnola; Bernard Choi; Haishan Zeng; Nikiforos Kollias; Andreas Mandelis; Michael D.

Morris; Brian J. F. Wong; Justus F. Ilgner, Editors, *Proceedings of SPIE*, vol. 9689 (SPIE, Bellingham, WA 2016), 96893B.

- **S. Liu**, J. Eggermont, S. Nakatani, B. P. F. Lelieveldt, J. Dijkstra, **Light Intensity Matching Between Different Intravascular Optical Coherence Tomography Systems (Conference Presentation and Publication)**, in *Photonic Therapeutics and Diagnostics XII*, Hyun Wook Kang; Guillermo J. Tearney; Kenton W. Gregory; Laura Marcu; Melissa C. Skala; Paul J. Campagnola; Bernard Choi; Haishan Zeng; Nikiforos Kollias; Andreas Mandelis; Michael D. Morris; Brian J. F. Wong; Justus F. Ilgner, Editors, *Proceedings of SPIE* Vol. 9689 (SPIE, Bellingham, WA 2016), 96893D.

Abstract and Poster Presentation:

- **S. Liu**, J. Eggermont, Y. Sotomi, J. Dijkstra, **Attenuation and backscattering based tissue characterization in intravascular optical coherence tomography pullback-runs (Abstract)**, *Proc. SPIE*, 10042, *Diagnostic and Therapeutic Applications of Light in Cardiology*, 100420H (19 April 2017); doi: 10.1117/12.2251771;

- **S. Liu**, J. Eggermont, R. Wolterbeek, J. Dijkstra, **Factors which affect image intensities in IVOCT pullback runs (Abstract and Poster Presentation)**", in *Optics in Cardiology*, Rotterdam, 2015.

- **S. Liu**, J. Eggermont, R. Wolterbeek, A. Broersen, C.A.G.R. Busk, H. Precht, B. P. F. Lelieveldt, J. Dijkstra, **Improved Bioresorbable Vascular scaffold detection by Compensating for the Effect of the Catheter position on image intensities (Abstract and Poster Presentation)**, in *Optics in Cardiology*, Rotterdam, 2017.

- **S. Liu**, B. P. F. Lelieveldt, J. Dijkstra, **The detection of guide-wire with 3D volume of depth-resolved attenuation and backscattering coefficients in the intravascular optical coherence tomography (Abstract and Poster Presentation)**, in *Optics in Cardiology*, Rotterdam, 2017.

Acknowledgment

Motivated by my curiosity about being a scientist, I started to look for a PhD position abroad. Thanks to Dr. Changyan Xiao and Marius, I got to know LKEB. Thanks to Boudewijn and Jouke for offering me the opportunity to enter LKEB, I got to conduct my research with OCT images, to which I have dedicated myself for the rest of my research years.

LKEB is a wonderful place for a student to transform softly to a professional. Thank everyone here for accepting my (I hope) occasionally bungling and naiveté. I shall start with Professor Reiber, a respectable scholar. Thank you for founding LKEB and providing us later scholars with an internationally competitive environment to conduct research. Dear Boudewijn, I appreciate you creating such a vivid and creative ambiance for research. In hindsight, I enjoyed all the moments working here. Meanwhile, I would like to thank you for the methodical management and guidance of my thesis project. Thanks to your thoughtfulness and decisiveness, the project proceeded and ends well-organized. Dear Jouke, thank you for helping me overcome so many difficulties throughout the project. The progressing of the project benefited from your long-time accumulated good connections and your dedicated guidance. No matter how tangled the question was from the reviewer, you always backed me up with your broad clinical and technical knowledge on OCT to reach a decent answer.In particular, I would like to thank you for your great support for helping me with the Dutch translation and valuable suggestions on the thesis.

Dear Oleh, thank you for devoting tremendous effort and time to help me with the Histogram manuscript. Your rigorous drafting standard costs me a great amount of energy, but it all paid off with the pleasure and the confidence of having a highly qualified manuscript. Dear Berend, many thanks for walking me through those low points, and also for spending time on helping me with the statistical analysis and paper writing. Dear Patrick and Jeroen, thank you for all the kind and timely support for my work and life. Our file commits on Fridays and the WOT trainings are highly enlightening for me to finish the book. Dear Niels, thank you for being always friendly, carrying, sweet and C++. Bedankt dat jullie drieën me geholpen hebben met mijn Nederlands en mijn levensvrienden geworden zijn. Dear Floris, thank you for those inspiring discussions. Dear Jos, your experience of driving a tank and marathon running is as amazing as your passion and understanding of MRI imaging. Dear Alex, Baldur, Els, Jasper, Leo, Michèle, Pieter, Qian, Rahil, Rob, Ronald and Shengxian, thank you for all the

kind help and good memories and I shall remember all the best ones.

Also thank all those aspiring fellows on the way pursuing their degrees. Ancong, Ahmed, Antonis, Chenhong, Evgeni, Hessam, Labrinus, Ling, Mohammed, Mohamed×2, Pauline, Qing, Shan, Sahar, Shufang, Walid, Yingguang, Yuanbo, Yuchuan, Zhiwei and Zhuo. You embellished my journey and let me know that I am not alone.

Dear all LKEBers, your meticulous attitude, genial personality, unselfish spirit of sharing and cooperating, and passion for work and life will stay with me. These commendable qualities will remind me to do as good as you.

Dear Professor Serruys, thank you very much for facilitating the cooperation of LKEB and excellent doctors from Cardialysis. For me, you are a inspirational leader in the field who always motivates me to work hard. Dear Yoshi, Shimpei, Yohei and Olli, thank you for your tremendous support. It was truly enjoyable to work with you.

I want to specially thank my computer which never failed me during my PhD time with its top configuration.

Yang Liu and Eva, my dear friends, I was lucky to meet you here. Thank you for all your accompanying, listening, empathy and encouragement. I was also lucky to meet many optimistic, joyful and positively upward friends, Illia, Maria, Katia, Tomas, Changgong, Chaoping, Hua, Yaoyao, Yuanyuan. I cherished and enjoyed every gathering with you guys. Wish you all the best.

Last but not least I would like to thank my parents and my families. 我很感谢亲爱的爸爸妈妈和姐姐对我所有的决定义无反顾地支持理解与包容. 我也很庆幸成长在一个大家庭里，感谢每个成员姑母姑父，姨母姨父，表哥表嫂表姐表姐夫，尤其感激三姨，三姨父对我学业和事业的大力支持，我会永远铭记. Dear Den, meeting you is the biggest surprise I got in the Netherlands. You are my dearest friend, companion, supporter and my ”den”.

Curriculum Vitae

Shengnan Liu was born in Jilin Dunhua, China, on July 29, 1986. She received her bachelor degree in Mathematics and Applied Mathematics in 2009 at Hunan University. In the same year she entered the postgraduate program majored in Control Science and Engineering with a exemption (for top 15%) from Entrance Examination. In 2012, she got her M.Sc. degree and started her Ph.D studies in Division of Imaging Processing (LKEB) in Leiden University Medical Center. Working in the Vascular and Molecular Imaging Group, her interest of research includes Tissue Analysis on Intravascular Optical Coherence Tomography images. The project has been carried out in broad collaborations with Cardialysis BV, Osaka University and Tokai University. The outcomes are collected to construct this thesis.

It is an end of a journey,

yet a start of a brand new voyage...